Atmospheric Influences
on Space-Based Observations
of Extremely High-Energy Cosmic Rays

Zur Erlangung des akademischen Grades eines

Doktors der Naturwissenschaften

von der Fakultät für Physik des
Karlsruher Instituts für Technologie (KIT)

genehmigte

Dissertation

von

Dipl. Phys. Stefanie Elfriede Falk

aus Gengenbach (Baden)

The fluorescence light of the UHECR showers
cascading through the Earth atmosphere
is shining outwards, we know it, towards space:
It shall not shine in vain!

<div style="text-align: right">

ETIENNE PARIZOT

</div>

Atmospheric Influences on Space-Based Observations of Extremely High-Energy Cosmic Rays

The Extreme Universe Space Observatory on board the Japanese Experiment Module (JEM-EUSO) shall observe the night side of the Earth from space to detect the faint UV light emitted by air showers. For the detection of air showers, it is mandatory to know the state of the Earth's atmosphere, since it has an influence on the shower development, as well as on the emission and transmission of the UV light. In this work, this atmospheric influence on extensive air shower detection from space has been studied in detail.

For this purpose, an important contribution has been made to the adaption of $\overline{\text{Off}}\underline{\text{line}}$, the analysis and simulation software framework of the Pierre Auger Observatory, to the needs of JEM-EUSO. A reduced version of $\overline{\text{Off}}\underline{\text{line}}$ has been developed together with colleagues of the JEM-EUSO collaboration. The existing atmospheric simulation has been revised within this work. Improvements by means of computation time for the atmospheric profiles and depth in case of very inclined shower geometries have been made. The new algorithm has been proven to give reliable results and is up to eight times faster compared to the old algorithm. The UV absorption by ozone has been included in the simulation. The concept of an Earth surface described by albedo and outgoing phase function has been introduced. The light reflection on ground is calculated by a new module in the simulation chain. All algorithms have been validated and extensively tested.

The Global Data Assimilation System (GDAS) has been chosen as a global atmospheric model to provide atmospheric profiles. Ten example locations have been selected. Monthly mean atmospheric profiles have been compiled for each location and used for simulation to compare to the U.S. Standard Atmosphere 1976 by means of atmospheric depth and light emission. Deviations in the vertical atmospheric depth up to $30\,\text{g}\,\text{cm}^{-2}$ have been found. A shower at $E = 10^{20}$ eV and $\theta = 60°$ has been simulated for studying the effects on the reconstruction procedures. The largest deviation of the position of the shower maximum was about $1\,300$ m. The amount of emitted fluorescence photons changes by $\pm(5-6)\%$. From the comparison of different locations within a wide field of view, the atmospheric profile closest to the nadir position on ground will be sufficient, except for showers close to the edge of the field of view.

The transmission properties for a clear atmosphere have been evaluated for a distance of 40 km at ground level and at the orbit of the International Space Station (ISS) as possible location for a telescope. In both cases, the attenuation by Rayleigh scattering dominates compared to Mie scattering. At the main fluorescence line (337 nm), the attenuation in the ground-based scenario is almost 98% compared to 50% in the space-borne case. The absorption of UV light by ozone has been studied thoroughly. Mean monthly profiles of ozone have been calculated from ozone sounding data and processed with the simulation chain of $\overline{\text{Off}}\underline{\text{line}}$. Ozone reduces the amount of transmitted light in average by 8.5% for a space-borne experiment with a seasonal variation of about $\pm1\%$. The least ozone is found close to the equator resulting in about 3% less attenuation compared to a continental ozone profile at higher latitude. The overall impact of the atmosphere has been studied on a set of simulated air shower events in different conditions. The assumed ground properties strongly affect the amount of light transmitted.

The total amount of light varies by about 10% at high geographical latitudes (51°) and close to the equator. The monthly mean profiles have been compared to single date profiles. For locations in the tropics, no significant change of the amount of light has been found, the opposite for locations in subarctic regions or the cold temperated zone.

Near event-time atmospheric data have to be implemented into the reconstruction of air shower events. Altitude-dependent atmospheric profiles can be provided by a database filled with GDAS data corresponding to the air shower event time and ISS position. Parametrized ozone profiles are given for several regions. Earth albedo for several typical surfaces is provided in parametrized form.

Atmosphärische Einflüsse auf die Messung von extrem hochenergetischer kosmischer Strahlung vom Weltraum aus

Das Extreme Universe Space Observatory on board the Japanese Experiment Module (JEM-EUSO) soll vom Weltraum aus die Nachtseite der Erde beobachten, um das schwache UV-Licht, welches von Luftschauern erzeugt wird, zu detektieren. Die Messung der kosmischen Strahlung mittels Luftschauer benötigt eine genaue Kenntnis der Atmosphäre, da sich ihr Zustand auf die Entwicklung sowohl des Luftschauers als auch der Emission und Transmission des UV-Lichts auswirkt. Zusätzlich zu den Systemen zur Atmosphärenüberwachung, die mit JEM-EUSO zur ISS gebracht werden, sollen globale Atmosphärenmodelle verwendet werden. Anhand von Daten eines solchen Modells wird die Signifikanz der vielfältigen atmosphärischen Einflüsse auf die Messung von Luftschauern vom Weltraum aus exemplarisch anhand von JEM-EUSO innerhalb dieser Arbeit behandelt.

Zu diesem Zweck wurde maßgeblich an der Adaption des Analyse- und Simulationsframeworks des Pierre-Auger-Observatoriums, $\overline{\text{Off}}\underline{\text{line}}$, für die Belange von JEM-EUSO gearbeitet. In enger Zusammenarbeit mit Kollegen aus der JEM-EUSO-Kollaboration wurde eine reduzierte Version der $\overline{\text{Off}}\underline{\text{line}}$-Software erarbeitet und an JEM-EUSO angepasst. Meine Arbeit resultierte unter Anderem in der Überprüfung und Verbesserung der bestehenden Atmosphärensimulation. Ein Geschwindigkeitsgewinn bei der Berechnung von atmosphärischen Profilen und Tiefenprofilen für stark geneigte Luftschauer konnte erzielt werden. Der neue Algorithmus ist verlässlich und bis zu acht mal schneller als der alte. Es war notwendig neue Klassen und Funktionen speziell zur Berechnung der Reflexion von Licht an der Erdoberfläche einzuführen. Mit JEM-EUSO ist es im Gegensatz zu den üblichen, erdgebundenen Fluoreszenzteleskopen möglich, die am Erdboden reflektierten Komponenten des vom Luftschauer emittierten Lichts zu beobachten. Abhängig von der Beschaffenheit des Erdbodens stellt dieses reflektierte Licht einen signifikanten Anteil des detektierten Lichts dar. Ferner wurde auch die Absorption von UV-Licht durch Ozon in die Simulation integriert, welche im erdgebundenen Fall vernachlässigt werden kann.

Das Global Data Assimilation System (GDAS) wurde als globales Atmosphärenmodell ausgewählt. Es stellt unter anderem Temperatur-, Druck- und Feuchteprofile auf einem globalen $1° \times 1°$-Netz zur Verfügung. Zehn Beispielorte wurden anhand ihrer ausgezeichneten Lage ausgewählt. Sie befinden sich in den subarktischen, gemäßigten, bis hin zu den subtropischen und tropischen Breiten und liegen sowohl inmitten der Ozeane, als auch auf den Kontinenten. Um diese Orte mit der zurzeit für JEM-EUSO-Simulationen verwendeten U.S. Standard Atmosphere 1976 (US-StdA 76) zu vergleichen, wurden Monatsmittel gebildet. Die berechneten atmosphärischen Tiefen weichen um bis zu 30 g cm^{-2} von jener der US-StdA 76 ab. Dies würde, wenn nicht bei der Rekonstruktion von späteren Daten berücksichtigt, zu einer Bevorzugung größerer Tiefen für das Schauermaximum in der Nähe des Äquators führen. Das Umgekehrte gilt für Orte in den hohen Breiten. Die Luftschauersimulation für einen Schauer der Energie 10^{20} eV und einem Einfallswinkel von 60° ergibt hierbei eine maximale Verschiebung des Schauermaximums von etwa 1 300 m, was bei einer angestrebten optischen Auflösung von JEM-EUSO von etwa 500 m möglicherweise aufgelöst werden kann. Die Menge an emittiertem Fluoreszenzlicht schwankt um $\pm(5-6)\%$, welches zwar nicht unsignifikant

ist, aber bei der derzeit besten Rekonstruktionsgenauigkeit von etwa 20% in der Energie, wohl nicht aufzulösen sein dürfte. Für eine schnelle Analyse des Schauermaximums ist die US-StdA 76 ausreichend, sollte allerdings für genauere Analysen zumindest durch ein Atmosphärenprofil am Ort des Fußpunkts des Teleskops am Erdboden ersetzt werden.

Zur Illustration der Signifikanz der Abschwächung des Lichts durch Streuung in der Atmosphäre wurde zunächst die Transmission für klare atmosphärische Bedingungen, wie von der Pierre-Auger-Kollaboration für Malargüe gemessen, auf eine Entfernung von 40 km berechnet. Die gleichen atmosphärischen Bedingungen wurden verwendet, um die Transmission zu einem Teleskop in 400 km Höhe zu berechnen. Während im ersteren, klassischen Fall die Abschwächung des Lichts bei einer Wellenlänge von 337 nm 98% beträgt, liegt sie in letzterem Fall bei nur 50%. In einer solch klaren Atmosphäre dominiert in beiden Fällen die Rayleighstreuung. Anhand von drei Beispielen wurde die Signifikanz der Ozonabsorption studiert. Aus Ozonsondendaten der amerikanischen National Oceanic and Atmospheric Administration (NOAA) wurden mittlere Monatsprofile der Ozonverteilung in der Atmosphäre erstellt. Auch wenn die Ozonabsorption keine Rolle für bodengebundene Observatorien spielt, bewirkt sie eine Reduktion der Transmission im Falle von JEM-EUSO um $7 - 10\%$. Über das Jahr betrachtet variiert die Ozonkonzentration und somit die Abschwächung um $\pm 1\%$. Ein passendes Ozonprofil sollte deshalb bei der Analyse der echten Daten berücksichtigt werden. Schlussendlich wurden sowohl Emission als auch Transmission mittels Simulationen getestet. Die Verhältnisse des direkten Fluoreszenz- bzw. gestreuten/reflektierten Cherenkovlichts zur gesamten Lichtmenge, welche das Teleskop erreicht, ist stark abhängig von der angenommenen Albedo und Phasenfunktion des Erdbodens. Die maximale Abweichung des gesamten, transmittierten Lichts zum Mittelwert von neun Standorten beträgt 10%. Es ergibt sich auch hier, dass Orte in den Tropen geringere Abweichungen aufweisen, als Orte in subarktischen Gebieten. Gleiches ergibt sich beim Vergleich einzelner Tagespofile zu den monatlichen Mitteln. Außerhalb der Tropen wäre es daher sinnvoll, zeitnah zum Luftschauerereignis passende Profile anstelle der gemittelten Profile zu verwenden, da die atmosphärischen Schwankungen und somit die Emission und Transmission erheblich sind.

Hinsichtlich des JEM-EUSO Experiments ist es unerlässlich, höhenabhänige atmosphärische Daten zeit- und ortsnah zum Luftschauerereignis in die Prozeduren zur Rekonstruktion von Luftschauern einzuarbeiten. Welche atmosphärischen Daten in welcher Genauigkeit später in einem Experiment Anwendung finden, kann natürlich noch variieren und von denen, in dieser Arbeit vorgestellten, abweichen. Dennoch soll betont werden, dass beispielsweise die GDAS Daten eine ausreichende räumliche und zeitliche Auflösung für übliche Luftschauer-Experimente aufweisen, und ihre unkomplizierte und zuverlässige Anwendbarkeit bei Analysen und Rekonstruktionen von Luftschauerereignissen bewiesen haben.

Contents

Introduction

More than 100 years ago, the hunt for the highly penetrative, non-terrestrial radiation began. Ever since these pioneering days and the achievements of Victor Hess in consolidating their existence, cosmic rays have fascinated generations of physicists around the globe. Early on, cosmic rays have been proven a valuable tool for investigating the physics of particles and antiparticles – long before accelerators were built which could reach adequate energies. For example, the positron was found in cosmic rays by Anderson in 1933. The measurement of particle cascades in the atmosphere induced by primary cosmic rays, as consulted by Werner Kolhörster and Pierre Auger in 1939, had opened the door to even higher energy ranges. Decades of intensive work have shed light into the vast darkness of the astroparticle space. Yet, the mysteries of their origin and nature have not been solved completely. About ten years ago, the Pierre Auger Observatory set off to thoroughly investigate the upper end in the ultra-high energy cosmic rays spectrum, excavating more puzzling details about cosmic rays.

The decade to come might see a cosmic rays observatory orbiting the Earth, as already proposed by John Linsley in the early 1980s. The Extreme Universe Space Observatory on board the Japanese Experiment Module (JEM-EUSO) shall be a UV light detector performing astrophysics through the particle channel by looking towards Earth from above. The main goal of JEM-EUSO is to explore the cosmic ray spectrum at about 10^{20} eV and beyond. On board the International Space Station, this detector will monitor almost the whole Earth and cover the celestial sphere almost homogeneously. Since the cosmic rays are measured calorimetrically in the Earth's atmosphere, this poses a further challenge in monitoring its state. The state of the atmosphere affects the development of the particle cascades known as extensive air shower, as well as the emission and transmission of the induced UV light.

Complementary to the on-board Atmospheric Monitoring System of JEM-EUSO, the usage of a global atmospheric model, e.g., the Global Data Assimilation System (GDAS), has been proposed. Based on GDAS data, the significance of the atmospheric influence on the measurement of cosmic rays by an Earth orbiting telescope shall be investigated within this work. This includes studies dedicated to the shower development, as well as light emission and transmission in atmospheric conditions from the subarctics to the tropics. The absorption by ozone has been studied explicitly. This general investigation will be completed by conclusions with respect to the JEM-EUSO mission. In this context, the development of a simulation and analysis software framework for JEM-EUSO based on the $\overline{\text{Off}}\underline{\text{line}}$ framework of the Pierre Auger Observatory has been initiated.

In Chapter 1, a brief introduction to cosmic rays and extensive air showers, covering the most important basics related to this work, will be given. In Chapter 2, the JEM-EUSO detector and detection principle will be presented in more detail. Chapter 3 will cover the necessary basics of atmospheric science including radiative transfer, scattering by molecules, absorption by ozone, and reflection of light on the Earth's surface. In Chapter 4, the O̅ff̲l̲i̲n̲e̲ framework for JEM-EUSO will be presented together with the developed enhancements to the atmospheric simulation. The global atmospheric model used will be briefly introduced in Chapter 5. Based on these data, the influence of the varying atmospheric conditions on atmospheric depth and light emission of an extensive air shower will be studied. The radiative transfer in the context of a space-borne experiment will be studied in Chapter 6. This includes the attenuation by molecular scattering, the absorption by ozone, and a final comparison between different example locations and conditions. A summary of the results and conclusions will be given in Chapter 7.

Cosmic Rays and Extensive Air Showers

For more than one century, cosmic rays (CR) have fascinated physicists around the globe. Back in the pioneering days of nuclear physics in the early 20th century, the existence of an ionizing radiation, other than natural ores and minerals, was found. Balloon ascents by Albert Gockel indicated a strong penetrative radiation in the atmosphere [37]. Theodor Wulf conducted precise electroscopic measurements ascending the Eiffel tower in Paris (France). He also found an increase of ionization towards the top [89]. However, cosmic rays only became established after subsequent balloon ascents by Victor Hess and Werner Kolhörster in 1911 and 1912. They measured the rate of ionization with high accuracy, and consolidated first the expected decrease followed by a strong increase with altitude [46].

Although the cosmic ray spectrum has been measured in a very wide energy range by various experiments during the past decades, some of the remaining questions read the same as a century ago: Where do they come from? Which mechanisms accelerate them? Is there a limit to the spectrum? If yes, what causes this limit?

In this chapter, some important features of the cosmic ray spectrum are described in more detail. With regard to the objective of this work, CR detection techniques based on extensive air showers, and light emission during the shower development will be briefly presented.

1.1 Cosmic Rays

CR consist mainly of fully ionized atomic nuclei with a high abundance of hydrogen. The CR flux is steeply falling with energy over many orders of magnitude. It can be well described by a power law

$$\frac{\mathrm{d}N}{\mathrm{d}E} \propto E^{-\gamma},\qquad(1.1)$$

with the energy E of a nucleus, the number of particles N, and $\gamma \approx 2.7$. Towards higher energies at about 1 PeV, the change in the spectral index ($\gamma \approx 3.1$) marks a feature called *knee*. At about 80 PeV a further steepening of the spectrum, the *second knee*, is observed [7]. The spectrum flattens again at about 4 EeV which is called *ankle*. A flux suppression occurs beyond 50 EeV[1]. These features become clearly visible in a CR spectrum scaled by a factor of $E^{2.5}$ (Fig. 1.1).

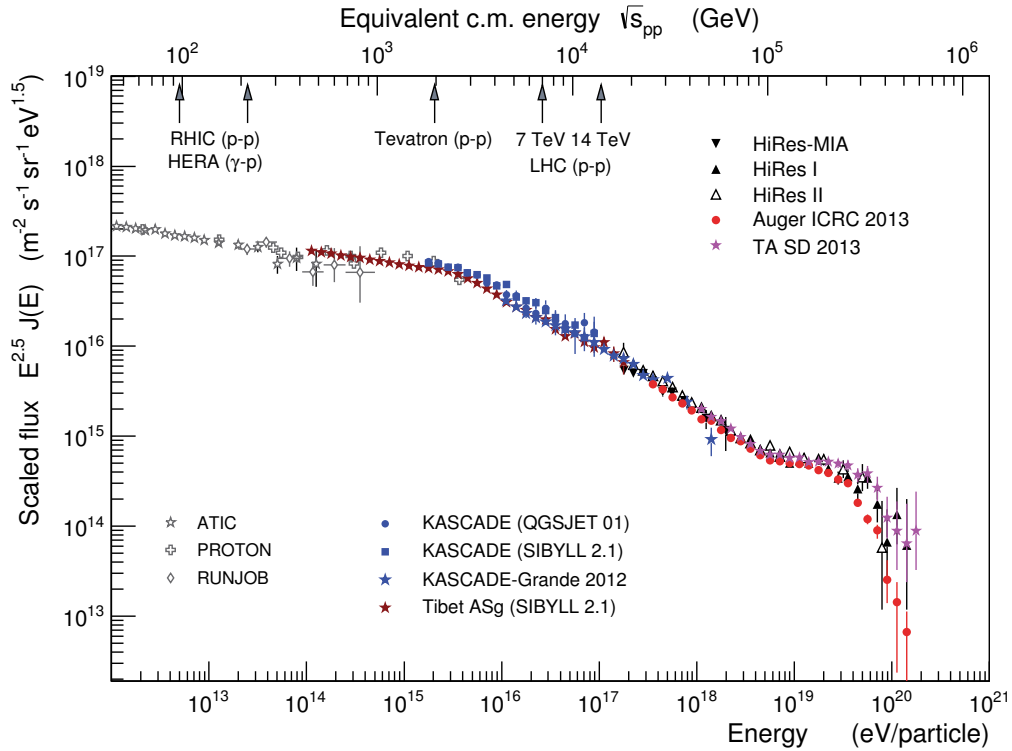[1] PeV refers to 10^{15} eV and EeV to 10^{18} eV.

Figure 1.1: Double logarithmic all-particle spectrum of the CR flux scaled by $E^{2.5}$([29] updated by Ralph Engel). A steepening of the spectrum (knee) becomes visible at about 1 PeV. Flattening appears at about 3 EeV (ankle). Above 50 EeV, the flux is highly suppressed. PeV refers to 10^{15} eV and EeV to 10^{18} eV.

The abundance of individual chemical elements has been measured with balloon or satellite experiments for primary energies below 1 PeV. At low energies (TeV − PeV), the composition mimics the known solar system element abundance, except for some light elements (e.g., lithium, beryllium, and boron), and elements below iron and lead are more abundant in CR due to spallation processes during propagation [19]. Thus, CR are accelerated ordinary matter of galactic origin in this energy regime. Due to the low flux, those direct measurement methods become insufficient at higher energies.

For better discrimination, the term high energy cosmic rays (HECR) is used from the knee onwards to about the ankle. The knee, as well as the second knee can be explained for HECR of galactic origin by a *leaky box* model [35]. The acceleration of charged particles is bound to the galactic magnetic field B, and therefore proportional to the atomic mass A and charge Z of the CR. The Larmor radius of a charged particle with a velocity $v_\perp$ perpendicular to the magnetic field

$$r_L = \frac{A \cdot v_\perp}{Z \cdot B} \tag{1.2}$$

exceeds the dimension of the galactic magnetic field at a critical momentum, and particles can escape the galactic disk. The escape of particles can be observed at Earth as a flux suppression of this element in the spectrum. The maximum acceleration power of the sources is unknown at this point. The first change of the
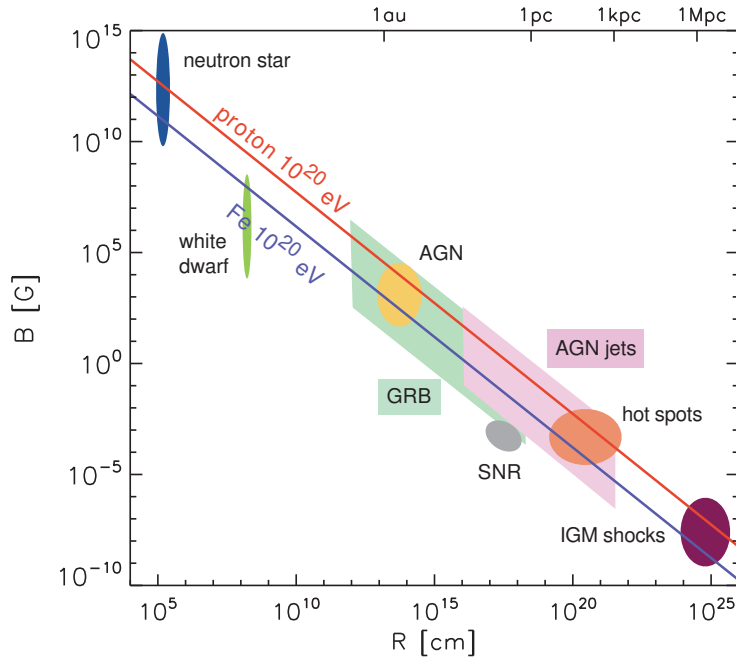
Figure 1.2: Hillas plot. The spatial dimension R is given in cm, the magnetic field strength in G. The red/blue line indicates confinement of protons/iron nuclei up to an energy of 10^{20} eV. Different sources are displayed regarding the typical range of parameters, with $\beta = 1$ [48,52].

spectral index is due to the suppression of the proton flux, while a second knee corresponding to a suppression of the flux of heavy elements at about 80 PeV is reported by the KASCADE-Grande collaboration [8]. The recovery of the flux at the ankle is most likely caused by high energy particles which are of extragalactic origin (ultra-high energy cosmic rays (UHECR)), though there are different models concerning the origin of the feature (rev. [17]). Composition studies in the ankle region can provide further information on the astrophysical sources, since all models predict a slightly different composition.

Astrophysical requirements on the dimension L of source candidates have been put into a simple form based on Eq. (1.2) by Hillas [48]

$$B \cdot L > \frac{2 \cdot E}{Z \cdot \beta},$$

(1.3)

with L in pc, B the normal component of the galactic magnetic field in terms of particle velocity and in units of μG, the particle energy E in units of PeV, and $\beta = v/c$ with c the speed of light. In Fig. 1.2, the resulting constraints on acceleration of protons (red line) and iron nuclei (blue line) are shown together with source candidates (e.g., neutron stars, Active Galactic Nuclei (AGN), Gamma Ray Bursts (GRB), Supernova Remnants (SNR)) according to size R and magnetic field strength. In the search of the sources of UHECR, deflection of charged particles in the galactic and inter-galactic magnetic fields constrains the possible messengers to high energy protons, and neutral particles such as neutrinos.

After the discovery of the cosmic microwave background (CMB) by Penzias and

Wilson in 1965, it became clear that the 2.7 K radiation of the CMB sets an upper limit to the observable flux of CR. The Greisen-Zatsepin-Kuz'min (GZK) effect describes the energy loss of UHECR through the interaction with CMB photons [40, 90]. In case of protons, this happens due to continuous photo-pion production

$$p + \gamma \rightarrow \Delta^+ \rightarrow p + \pi^0 \tag{1.4}$$
$$\rightarrow n + \pi^+.$$

Heavy elements undergo photo-disintegration because of giant dipole resonances at roughly the same energy. This leads to the assumption of a GZK horizon with a radius of about 100 Mpc. UHECR of energies exceeding 60 EeV have to originate from sources within the GZK horizon [41]. It is still not clear, whether the observed flux suppression is a manifest of this or rather an energy limit of the accelerating sources. Particles, close to the limit set by the GZK effect or probably exceeding it, shall be referred to as extreme energy cosmic rays (EECR).

Towards the very end of the known spectrum ($\sim 10^{20}$ eV), the kinetic energy of particles is of macroscopic order, though the probability of encountering them at Earth is as low as once per century and square kilometer. Therefore, current experiments like the Pierre Auger Observatory in Argentina or Telescope Array (TA) in the US use detectors of ~ 1000 km^2-size to observe the secondary particle cascade induced by primary CR that is called extensive air shower (EAS). In case of the Pierre Auger Observatory, an area of 3000 km^2 is monitored by a surface detector array that consists of ~ 1600 water Cherenkov detectors and 27 fluorescence telescopes measuring the fluorescence light emission from ionized nitrogen molecules. A similar technique is used by TA, except for the surface detector consists of about 500 scintillator detectors on an area of 777 km^2. Regarding the composition of UHECR, data of the Pierre Auger Observatory suggest a trend from light to heavy elements above 10^{19} eV [1]. A trend that has not been confirmed by TA and other experiments on the northern hemisphere. The current data of these experiments are consistent with a constant light composition [12].

1.2   Extensive Air Showers

Primary CR interact with nuclei of molecules in the Earth's atmosphere, inducing a cascade of secondary particles which is called extensive air shower. EAS allow for the indirect detection of UHECR by the measurement of secondary particles on ground, induced light emission, or radio emission. An EAS consists of three components (see the schematic development depicted in Fig. 1.3a).

The *hadronic component* originates from the interaction of the primary particle with air molecules. Through inelastic scattering and hadronic interactions, new hadronic particles are created. About $2/3$ end up as charged particles (mainly $\pi^\pm$), the remaining $1/3$ as neutral particles (π^0). Those neutral pions induce the *electromagnetic component* of the shower ($\pi^0 \rightarrow \gamma + \gamma$). The charged pions decay into muons and neutrinos which form the *muonic component* of the air shower. Using the *superposition model*, heavy primary particles can be regarded as composites of A individual nucleons with $1/A$-th fraction of the total energy E_0. The number of hadronic interactions scales with A, and also the number of muons increases. The smaller shower-to-shower fluctuations for showers induced by nuclei compared
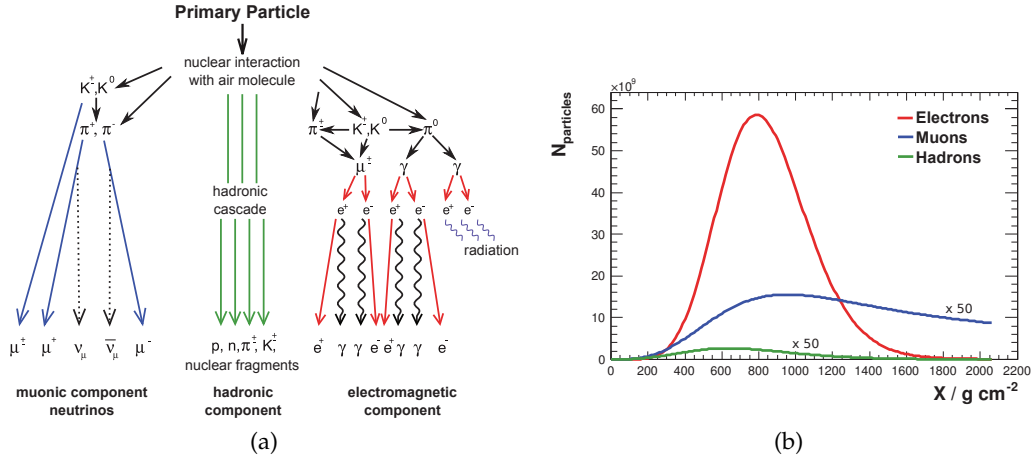
Figure 1.3: Components of an EAS. (a) Schematic development. The primary particle inter-acts with an air molecule and produces a hadronic shower through subsequent inelastic scattering. Through decay, charged and neutral pions are created. The former decay further to muons and neutrinos, the latter initiate the electromagnetic cascade emitting radiation at various wavelengths (after [42]). (b) Conex [73] simulated abundance of the shower components versus atmospheric depth X ($E = 10^{20}$ eV, $\theta = 60°$). Muonic and hadronic components are scaled by a factor of 50 (note the scale factor above).

to proton-induced showers can be explained by the superposition of A individual showers in the former case. The abundance for each component is exemplarily given for a Conex [73] simulated proton-induced shower with a primary energy $E = 10^{20}$ eV and a zenith angle $\theta = 60°$ in Fig. 1.3b. The muonic and hadronic component herein are scaled by a factor of 50. Photons, electrons, and positrons are the most abundant secondary particles in an EAS, but get quickly absorbed in the atmosphere. On the contrary, muons are far more penetrative, dominating the shower composition at sea level.

The development of the electromagnetic component can be understood by means of the *Heitler model* [44,56]. A cascade initiated by an electron or photon is driven by two radiative processes, *bremsstrahlung* of $e^{\pm}$ and *pair production* of $e^{\pm}$ by photons, and energy loss due to ionization. At the critical energy ($E_c \approx 86$ MeV in air), ionization losses equal particle production. The interaction length λ_{em} within which particles undergo interaction is given in units of depth (g cm^{-2}), and amounts to ~ 37 g cm^{-2} in air. The depth X is defined as the integral over the path length in a given density profile $\rho(z)$ from infinity (in this case space) to local height z_0

$$X(z) = \int_{\infty}^{z_0} \rho(z) \cdot \mathrm{d}z. \tag{1.5}$$

After each interaction, the particle number doubles, leading to 2^n particles after n interactions. The maximum number of particles is $N_{\max} = E_0/E_c$. In this simple model, the longitudinal development can be written as $N(X) = 2^{X/\lambda_{em}}$, with the shower maximum

$$X_{\max} = \lambda_{em} \cdot \log_2 \left(\frac{E_0}{E_c} \right). \tag{1.6}$$

After reaching its maximum, the number of particles decreases again through

absorption processes. The longitudinal profile of an EAS is well described by an analytical function

$$N(X) = N_{\max} \cdot \left(\frac{X - X_0}{X_{\max} - X_0} \right)^{\frac{X_{\max} - X_0}{\xi}} \cdot e^{\frac{X_{\max} - X}{\xi}}, \tag{1.7}$$

with ξ a polynomial function of X. Eq. (1.7) has first been proposed by Gaisser and Hillas and further developed in accordance to simulation results [43]. In average, the lighter a primary particle is, the deeper it penetrates through the atmosphere. Therefore, the shower maximum $X_{\max}$ is an important observable for composition studies [86].

Detection Techniques

There are several measurement techniques for EAS that can be divided into two categories, namely particle detectors and detectors for radiative emission caused by charged secondary particles in air. The former use ground arrays equipped with particle detectors to measure the lateral particle distribution on ground level. Detectors for radiative emission include optical measurements in the near-ultraviolet (UV) [22, 47], as well as most recently, the detection of signals at radio frequencies (several MHz) [30], or microwave frequencies in the GHz regime [78].

The important processes involved in the emission of UV light from EAS are *fluorescence* and *Cherenkov radiation*. Fluorescence light is emitted isotropically by nitrogen molecules that were excited by the *energy deposit* of mainly $e^{\pm}$. The spectrum reaches from about 280 nm to about 420 nm with the most intense line at 337 nm (Fig. 1.4).

Air fluorescence detectors image the longitudinal development of an EAS, allowing for a direct observation of the shower maximum and calorimetric measurement of the energy of the primary particle. The latter can be analyzed independently of high-energy interaction models and Monte Carlo (MC) methods. Fluorescence telescopes can only be operated during night, on fair-weather conditions, and when the background light level is not too high, e.g., the night sky in central Europe is too bright to effectively operate fluorescence telescopes. A duty cycle of about $10 - 15\%$ is quoted for ground-based fluorescence detectors [88].

For the calorimetric measurement, it is important to know the *fluorescence photon yield* as best as possible. The fluorescence photon yield is also sensitive to varying atmospheric conditions, since the radiative de-excitation of nitrogen competes with non-radiative processes, namely collisional quenching with other molecules in air. The fluorescence yield in dry air (pressure p, temperature T) can be written with respect to the main spectral line at $\lambda = 337$ nm

$$Y_{\text{air}}(\lambda, p, T) = Y_{\text{air}}(337 \text{ nm}, p_0, T_0) \cdot \frac{I_\lambda}{I_{337}(p_0, T_0)} \cdot \frac{1 + \frac{p_0}{p'_{\text{air}}(\lambda, T_0)}}{1 + \frac{p}{p'_{\text{air}}(\lambda, T_0) \cdot \sqrt{\frac{T}{T_0}} \cdot \frac{H_\lambda(T_0)}{H_\lambda(T)}}}, \tag{1.8}$$

where p'_{air} refers to the characteristic pressure of dry air. In Eq. (1.8), the intensity ratio $I_\lambda / I_{337}(p_0, T_0)$ and the absolute fluorescence yield $Y_{\text{air}}(337 \text{ nm})$, measured at fixed pressure p_0 and temperature T_0, is used. The temperature dependence in the
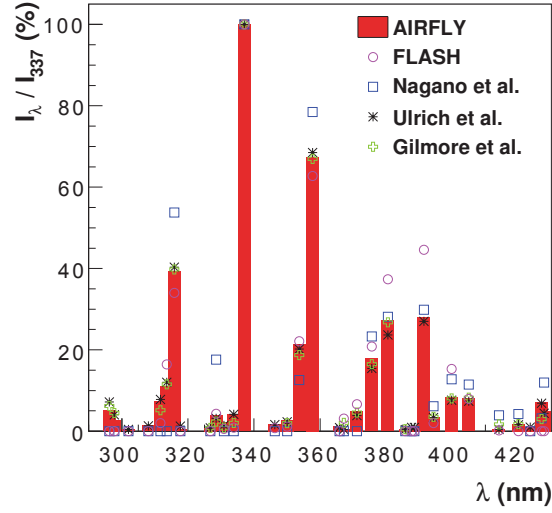
Figure 1.4: Relative fluorescence intensities normalized to I_{337} (100%) between about 290 and 430 nm. Measured by different experiments [51].

collisional cross section is described by

$$\frac{H_\lambda(T_0)}{H_\lambda(T)} = \left(\frac{T}{T_0}\right)^{\alpha_\lambda}, \tag{1.9}$$

with the exponent of the power law for each wavelength α_λ [51] In humid air, the atmospheric pressure p'_{air} has to be expanded with the characteristic pressure for collisional quenching p'_{H_2O} and the partial pressure of water vapor e

$$\frac{1}{p'_{air}} \rightarrow \frac{1}{p'_{air}}\left(1 - \frac{e}{p}\right) + \frac{1}{p'_{H_2O}} \cdot \frac{e}{p}. \tag{1.10}$$

The most recent measurement result on the absolute fluorescence yield $Y_{air}(337)$ reported is 5.61 photons/MeV at 1013 hPa, and 293 K [11].

Charged particles in matter exceeding the speed of light in the corresponding medium ($v > c/n$) cause non-canceling radiation due to asymmetric polarization. Other than the isotropically emitted fluorescence light, this Cherenkov radiation is highly peaked forward. The characteristic Cherenkov angle θ_c with respect to the particle direction is

$$\cos(\theta_c) = \frac{1}{\beta \cdot n(\lambda)}, \tag{1.11}$$

with the wavelength dependent refractive index $n(\lambda)$, and $\beta = v/c$. In air, θ_c varies between $\approx 1.4°$ at sea level and $\approx 0.2°$ at 35 km height. The photon yield for one particle is given by the *Frank-Tamm* formula [34]

$$Y_c = \frac{2\pi\alpha}{\rho_{air}(z)} \int_{\lambda_1}^{\lambda_2} \left(1 - \frac{1}{n^2(\lambda)\beta^2}\right) \cdot \frac{d\lambda}{\lambda^2}, \tag{1.12}$$

with the fine structure constant α. The number of emitted Cherenkov photons is continuous with respect to the photon wavelength and decreasing with increasing λ. The amount of emitted fluorescence and Cherenkov light in the UV is of about the same order of magnitude ($E \geq 10^{19}$ eV).

Extreme Universe Space Observatory on board the Japanese Experiment Module

In the early 1980s, Benson and Linsley came forward with a first proposal for a satellite-borne telescope looking towards the Earth at night time, called Maximum-energy Auger (Air)-Shower Satellite (MASS) [14]. Two later offspring of this original proposal were the competing Orbiting Wide-angle Light-collectors (OWL) (US National Aeronautics and Space Administration (NASA)) and the Extreme Universe Space Observatory (EUSO) (European Space Agency (ESA)). OWL was supposed to be a stereo vision, satellite-borne fluorescence detector with a high resolution in X_{max} and energy, as well as a wide field of view (FOV). The OWL mission intended orbits between $500 - 1\,000$ km [80]. EUSO was meant to be hosted by the Columbus module of the International Space Station (ISS), also aiming for a wide FOV and large exposure [39]. As part of the ISS, EUSO would have orbited the Earth at an altitude of roughly 400 km and with a ground speed of about $7\ \mathrm{km\ s}^{-1}$. Compared to the Schmidt optic design of OWL, EUSO had been designed as a lens telescope. Both projects were discontinued by the space agencies in the early 2000s mainly because of financial constraints. The Extreme Universe Space Observatory on board the Japanese Experiment Module (JEM-EUSO) is the direct successor of the original EUSO mission supported by the Japan Aerospace Exploration Agency (JAXA).

In accordance to the official mission status in the end of 2013 [83], details about the scientific goals of JEM-EUSO, the detector description, calibration systems, and atmospheric monitoring will be presented in this chapter. The final section is dedicated to the small scale prototypes built by the JEM-EUSO collaboration as performance test of hardware and software.

2.1 Scientific Goals

The main objective of JEM-EUSO as a space-based fluorescence telescope, is the increase of exposure to CR at energies exceeding 50 EeV (GZK threshold) by one order of magnitude compared to the largest current UHECR experiments.

The observed CR spectrum, composition, and lack of strong anisotropies constrain the possible candidates of sources of UHECR to a few known astrophysical objects. Furthermore, the GZK effect constrains the propagation distance of UHECR. EECR can originate only from a few potential sources within the GZK horizon. So

far, no source has been identified. EECR above 80 EeV could directly point back to their origin if they were protons. Therefore, the main goals of JEM-EUSO are

- the detection and high statistics measurement of trans-GZK CR,
- the study of the anisotropy of their arrival directions,
- the identification of sources, and
- the measurement of the sources' energy spectra.

The statistics needed to reach these goals are at least 10^3 of EECR events [70]. Although over the past decades the exposure of UHECR experiments has been increasing continuously (see Fig. 2.1a), a further increase, above 3000 km^2 in size, of ground-based arrays is not likely. JEM-EUSO could reach an order of magnitude larger exposure in less then 5 years compared to the current experiments. Regarding the study of anisotropy in the arrival directions of EECR, an Earth-orbiting telescope has the advantage that it could uniformly cover the celestial sphere. In Fig. 2.1b, the expected relative deviation from a uniform exposure as function of declination^2 is shown. A near full sky coverage will be reached if showers at all zenith angles can be reconstructed.

Apart from these, JEM-EUSO has the potential to perform studies on

- multi-messengers (ultra-high energy (UHE) neutrinos, gamma rays),
- galactic/extra galactic magnetic fields,
- relativity and quantum gravity, and
- atmospheric phenomena.

The study of multi-messengers is listed as exploratory goal, since it relates to the proclaimed goal of JEM-EUSO doing astronomy and astrophysics through the particle channel. Different propagation and source scenarios can be discriminated by measuring the UHE ν and γ-ray flux. The GZK effect (Eq. (1.4)) does not only place a limit on the propagation of charges nuclei, but continuously produces UHE ν and γ-rays through pion decay. UHE ν produced inside source regions can point back to their origin, and some exotic dark matter theories predict a high γ-ray flux. With the high statistics measurements by JEM-EUSO, UHE ν could be discriminated via the position of the first interaction and shower maximum, while UHE γ-rays can be identified by the sensitivity of the shower maximum to the geomagnetic field and the early interaction in the atmosphere.

Data from the monitoring of the UV background can be used for studying a variety of atmospheric phenomena. Atmospheric phenomena in the UV include, e.g., lightning, transient luminous events (TLE) (see Fig. 2.2), air glow, or light tracks left by meteors and meteoroids. Especially the correlations between CR, lightning, and clouds can be studied, since they are simultaneously observed.

---

^{2}*Declination δ* and *right ascension* are astronomic coordinates locating a point on the celestial sphere in the equatorial coordinate system. The declination is measured with respect to the celestial equator. Positive declination values point north, and negative values south [28].
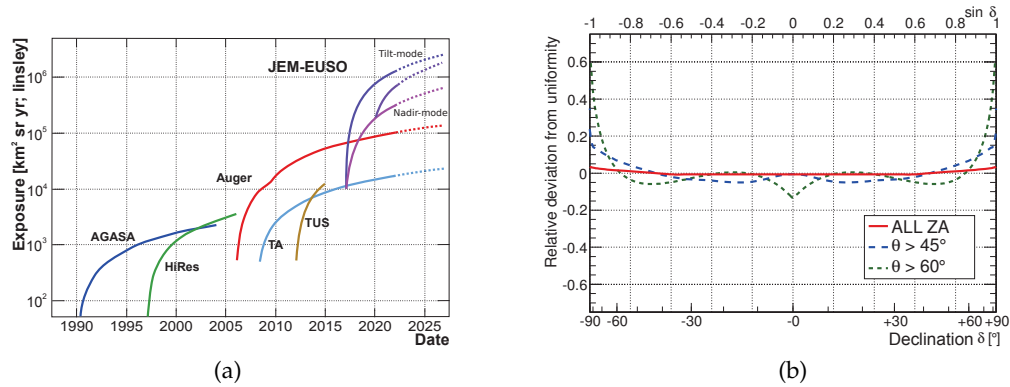
Figure 2.1: JEM-EUSO exposure. (a) Exposures of UHECR observatories from 1990 to 2025. Estimates of the future exposures of the Pierre Auger Observatory, Telescope Array (TA) and JEM-EUSO (adapted from [82]); (b) Expected distribution of observed exposure for JEM-EUSO as function of declination for different zenith angle sets of EAS. The zero-line implies full sky coverage [3].
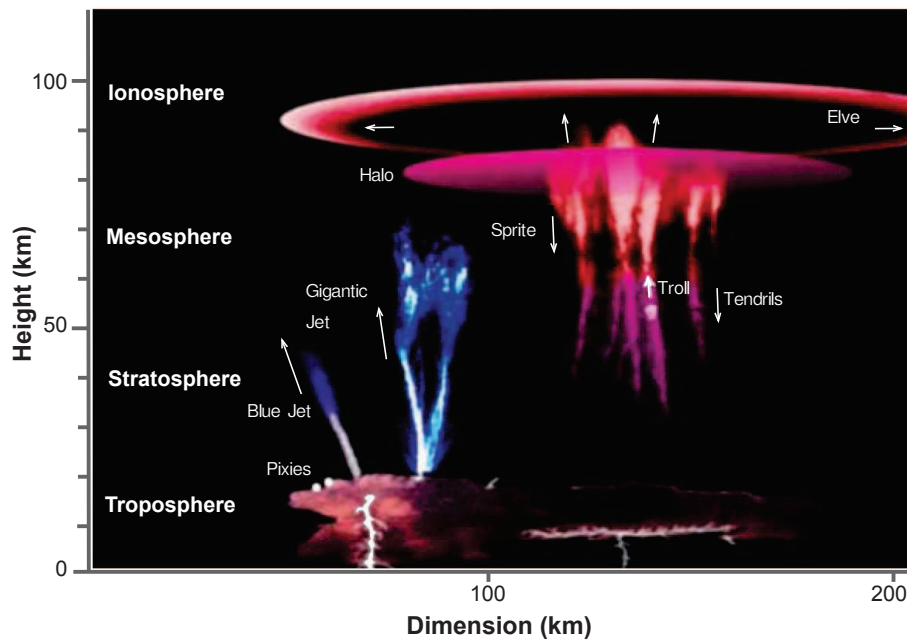

Figure 2.2: Artistic collection of various transient luminous events (TLE) by D. D. Sentmann (Univ. of Alaska in Fairbanks). Common tropospheric lightning is not highlighted.

2.2   Detector Design

JEM-EUSO shall orbit the Earth on board the ISS with a mean altitude of 400 km and an orbit inclination of 51.2° with respect to the equatorial plane of the Earth. The ISS is occasionally lowered for docking maneuvers of transport vehicles by about 70 km or raised to reduce air friction. The ISS orbit covers several climate zones from the subarctics to the tropics. The duration of one orbit is about 90 min with $\approx$ 36 min on the night side of the Earth. The detection principle of JEM-EUSO is depicted in Fig. 2.3. The instantaneous observation area for JEM-EUSO at 400 km altitude would be $1.4 \cdot 10^5$ km^2 in nadir mode (see Fig. 2.3a). It will also be possible to operate the telescope in *tilt* mode, tilted by several degree and increasing the observable area. An EAS developing within the FOV of JEM-EUSO produces fluorescence and Cherenkov light. In Fig. 2.3b, the characteristic light profile is depicted as function of the arrival time at the telescope aperture. The direct fluorescence component is well separated from the characteristic peak of the ground reflected Cherenkov light for a shower with a zenith angle of 60°.

The optics will consist of three non-circular Fresnel lenses of 2.65 m diameter each, made of Polymethyl-Metacrylate (PMMA). The diffractive system allows for a wide FOV of about 60° and an angular resolution of 0.075° ($\sim$ 550 m projected on ground from ISS orbit). The circular design of the original EUSO detector had to be trimmed to fit into the Japanese transport vehicle (H-II transfer Vehicle (HTV)). A circular shape redesign is probable to fit into the SpaceX Dragon vehicle [79].

The number of pixel on the focal surface is about $0.3 \cdot 10^6$ organized in 137 photo-detector modules (PDMs). The smallest detector unit is a multi-anode photomultiplier tube (MAPMT) with 64-pixel. A Schott BG3 filter is attached to each MAPMT. 2×2 MAPMTs build an elementary cell (EC), and 3×3 ECs form a PDM. About 8 PDMs will be managed by a Cluster Control Board (CCB). This detector hierarchy is displayed in Fig. 2.4. The integration time (Gate Time Unit (GTU)) of the electronics is 2.5 µs.

The operational bandwidth is $290 - 430$ nm due to the filters, the lens material, and the quantum and collection efficiencies of the MAPMTs (Fig. 2.5). The performance of these parts has been studied in detail using simulations. In Fig. 2.6, the number of photons and photoelectrons is shown as a function of the off-axis angle[3]. 100 showers had been simulated with an energy of 10^{20} eV and $\theta = 60°$. The azimuthal dependence of the optics has been tested for three different directions ($\psi = 0°$, $45°$, and $90°$). ψ is the deviation from the major axis of the optics. The impact of the atmosphere, as well as the different stages within the detector on the amount of light in the outer part of the FOV is clearly visible [3]. Reconstruction accuracies on

- arrival direction $\leq 2.5°$,
- energy $\leq 30\%$,
- $X_{\max} \leq 120$ g cm^{-2}, and
- energy threshold $\leq 5.5 \cdot 10^{19}$ eV

are required for reaching the physics goals (reference EAS at 10^{20} eV and a zenith angle of 60°).

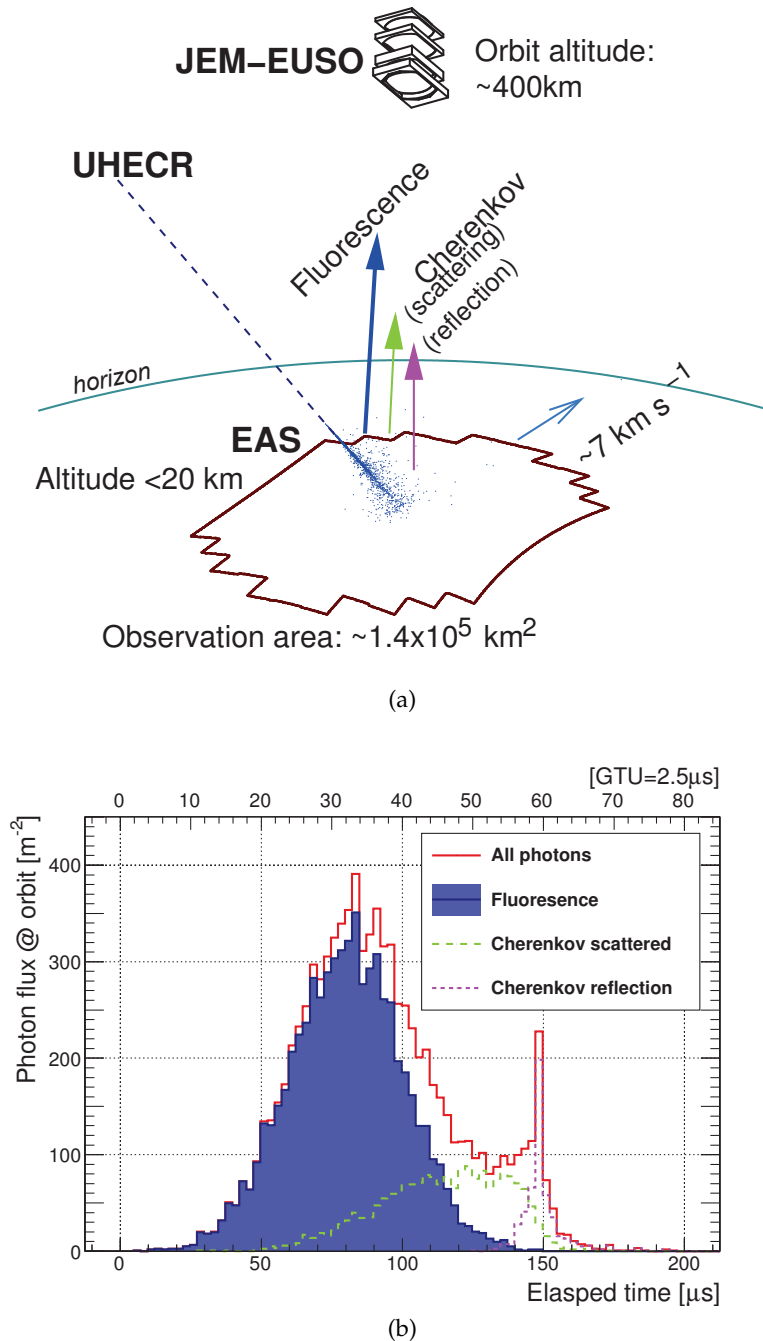[3]Angle between the location of the core and the telescope axis in nadir mode.

(a)

(b)

Figure 2.3: Illustration of the observation principle of JEM-EUSO for a nominal orbit of 400 km [3]. (a) The main signals are fluorescence photons emitted isotropically along the track and scattered Cherenkov light; (b) Light components at the aperture of JEM-EUSO as function of time for a simulated EAS of zenith angle 60° and energy 10^{20} eV. The peak from ground or cloud reflected Cherenkov light is visible well.
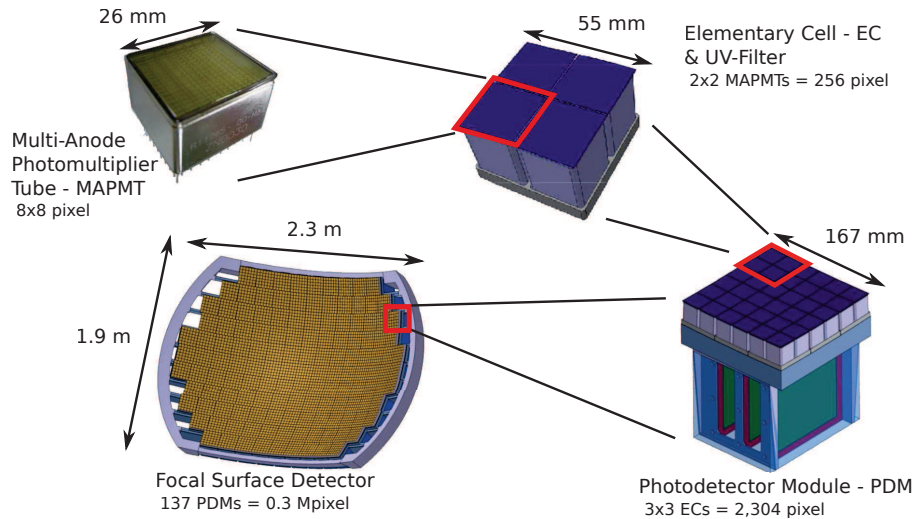
Figure 2.4: Hierarchical detector scheme of the JEM-EUSO focal surface. The smallest unit is a 8×8 pixel MAPMT. 2×2 MAPMTs form an EC, 3×3 ECs a PDM. The focal surface will consist of 137 PDMs [83].
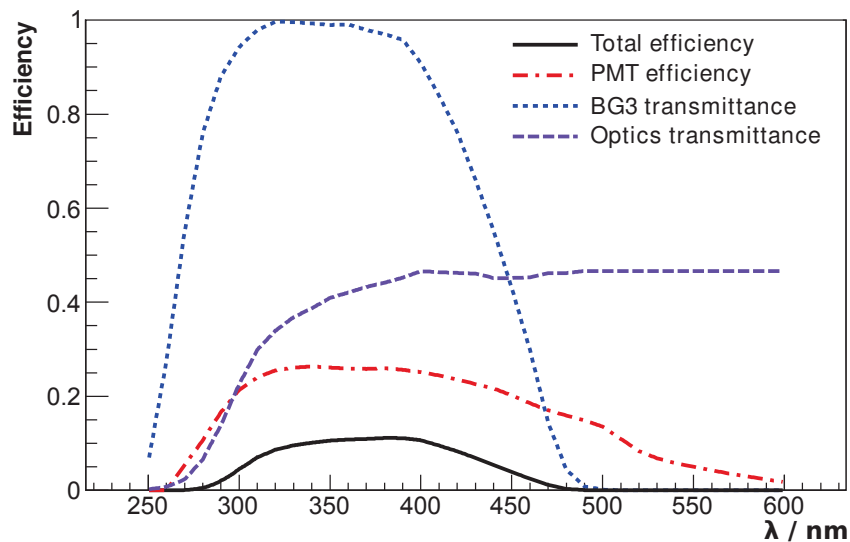
Figure 2.5: Optical properties and efficiencies of JEM-EUSO components: Filter (Schott BG3), transmittance of the 3 lenses (material PMMA), and MAPMT efficiency (Hamamatsu R11265). The optics efficiency has been calculated for light parallel to the optical axis [83].
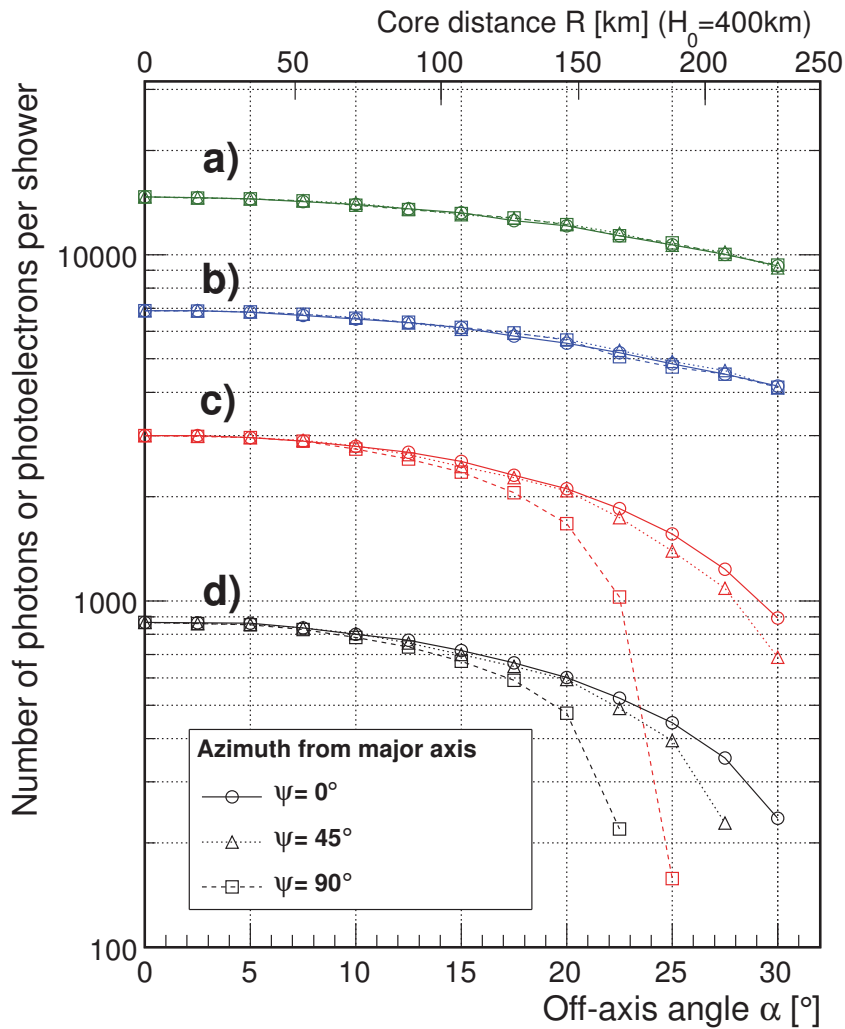
Figure 2.6: Number of photons and photoelectrons as function of off-axis angle α of the core location from nadir, obtained by simulating 100 EAS with 10^{20} eV and $\theta = 60°$. The off-axis angle is the angle between the core location and the nadir axis. To demonstrate the azimuthal dependence of the optics, three different directions are shown in circles ($\psi = 0°$), triangles ($\psi = 45°$) and squares ($\psi = 90°$) where ψ is the angle from the major axis of the optics. The scale on top is the radial distance from the center of FOV on the Earth's surface. In the figure, the different stages are compared: (a) photons from the shower axis directed toward the JEM-EUSO entrance aperture; (b) photons reaching JEM-EUSO entrance aperture; (c) photons reaching the focal surface and (d) detected signal (photoelectrons) (cited from [3]). The conservative assumption of background light is about 500 photons $m^{-2}sr^{-1}yr^{-1}$.

2.3 Calibration and Monitoring

There will be several subsystems for calibration. The absolute pixel-by-pixel calibration of the MAPMTs will be done on ground. A prototype light source consisting of an UV-LED array, an integrating sphere, and a collimator array has been built and tested [83]. The calibration of the MAPMTs, as well as the optics' efficiency will be monitored by an in-flight calibration system which will consist of several small diffuse light sources [83]. This relative calibration will be complemented by absolute calibration measurements using moonlight, and ground-based laser and calibrated xenon flash lamps as part of a Global Light System (GLS) [83]. Possible locations for this GLS are displayed in Fig. 2.7. The GLS can be used for trigger efficiency studies, energy calibration of the whole detector, as well as test of the accuracy of reconstructed directional pointing. In fact, UV laser light, shot through the FOV of JEM-EUSO, is an emulation of an EAS with known direction and energy. This calibration technique has already been in use for several years by ground-based experiments [32, 81].

An Atmospheric Monitoring System (AMS) consisting of an infrared (IR) camera and a Light Detection and Ranging (LIDAR) will be installed together with the main telescope on the ISS. These systems are to survey the cloud scenery and aerosol distribution within the FOV of JEM-EUSO. Additional information about the atmospheric state will be drawn from global atmospheric models (GAMs), see Fig. 2.8. The atmospheric information is important to reconstruct the energy and maximum of the shower properly. The GAMs and the influence of the atmospheric state on the measurement of JEM-EUSO will be described in more detail as part of this thesis.

The total band width of the IR camera ($10 - 12.5$ µm) is limited by narrow band filters of width $\delta\lambda = 1$ µm to two channels which are centered at 10.8 µm and 12 µm. The IR camera will have the same FOV as JEM-EUSO. An altitude resolution of the cloud top with an accuracy better than 500 m shall be achieved. Two algorithms have been tested to retrieve the cloud top temperature. The *stereo vision* requires two different images of the same scenery, using the movement of the ISS, e.g., at time t_1 and t_2. The distance between detector and cloud is computed by intersecting the two images and results in a measurement relative to the altitude of the ISS. The radiometric approach relates the measured *brightness temperature*[4] in both channels with the actual temperature of the cloud. The analysis will use a *split window algorithm* that has been developed for meteorological satellites [66].

The LIDAR uses a transmission system consisting of a Nd:YAG laser at 355 nm, an energy of 20 mJ/pulse, and a pointing mechanism for steering the laser ($\pm 30°$ from nadir) to examine the atmospheric depth near by an observed EAS event. The JEM-EUSO main telescope will act as detector for the backscattered laser. The LIDAR measurement can also be used to detect thin clouds at high altitudes (*cirrus*) and aerosols. The energy will be corrected in the shower reconstruction for the measured optical depth.

Prototypes of the GLS, IR camera, and LIDAR have been built for testing together with the small-scale JEM-EUSO prototypes.

---

[4]The brightness temperature is defined as the corresponding temperature of a blackbody of the same emissivity in the observed wavelength as the object.
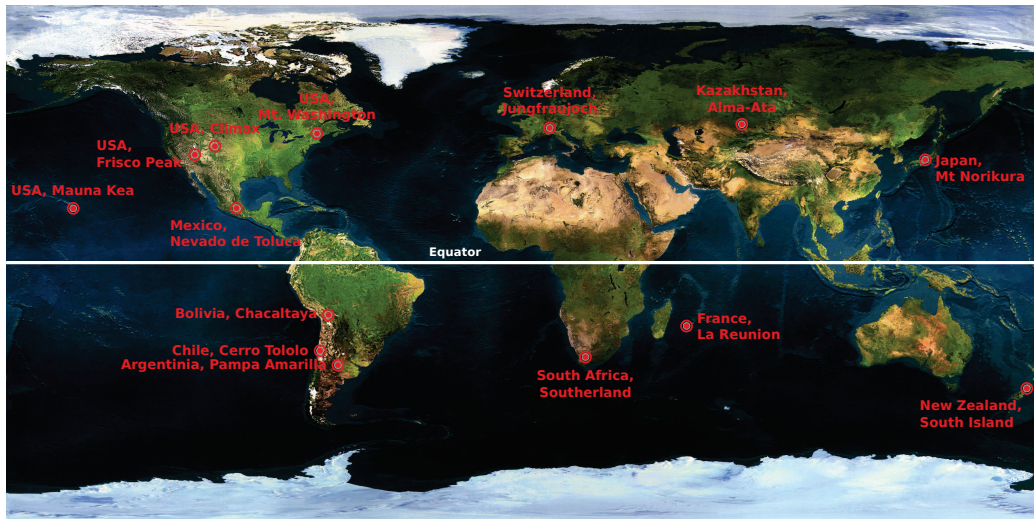
Figure 2.7: Map of the proposed future GLS station locations. Ground-based laser and calibrated xenon flash lamps will be used for the calibration of JEM-EUSO during the mission.
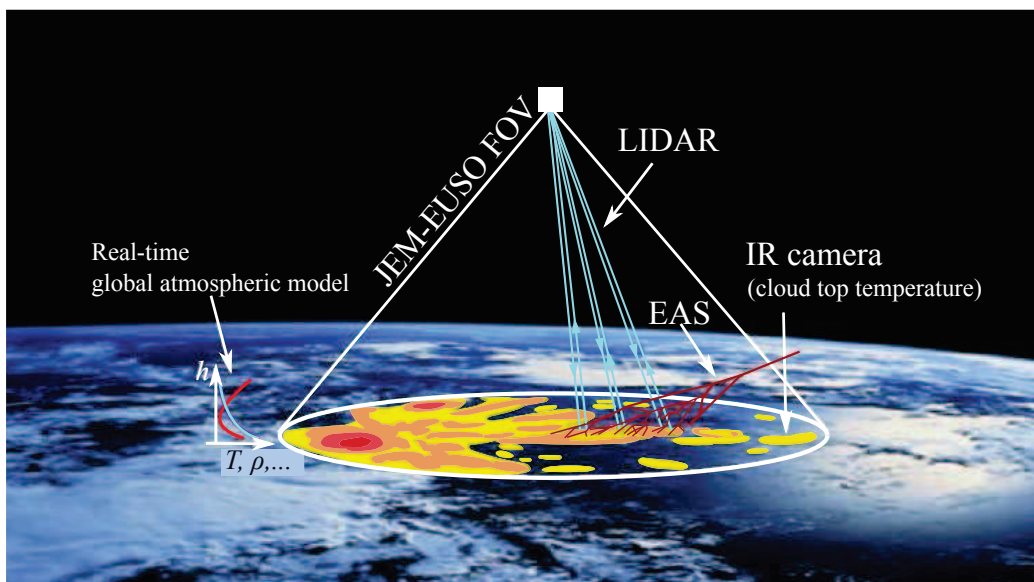

Figure 2.8: Conceptional sketch of Atmospheric Monitoring System (AMS) of JEM-EUSO. With IR camera, LIDAR, and real-time GAM data.

2.4   Prototypes

Two prototypes have been developed as test for the hardware and software performance, as well as for background measurements. A third proposal is currently investigated in cooperation with the Russian Federal Space Agency (ROSCOSMOS). The details about the prototypes and their current status will be given in the following.

The Extreme Universe Space Observatory prototype at the Telescope Array site (EUSO-TA) has been installed in Utah (USA) close to the fluorescence telescope at Black Rock Mesa (Fig. 2.9). EUSO-TA observes artificial UV light produced by the Central Laser Facility (CLF) and the Electron Light Source (ELS) of TA. The ELS is a compact linear accelerator with a output of 10^9 electrons per pulse at 40 MeV. The electron beam is dumped vertically into the air about 100 m in front of the fluorescence telescope at Black Rock Mesa, stimulating nitrogen fluorescence [77]. EUSO-TA consists of two square Fresnel lenses and a single PDM, with a FOV of $\pm 4°$. An external trigger is provided by the TA fluorescence telescopes [23]. The first data was expected by the end of July 2014 but data taking had to be postponed due to technical problems [74].

The Extreme Universe Space Observatory prototype on board a balloon (EUSO-Balloon) (see Fig. 2.10) was sent to a balloon flight campaign in Timmins (Ontario, Canada) by the French Space Agency (CNES) in the mid of August 2014. The purpose of the EUSO-Balloon is to test the performance of critical JEM-EUSO systems such as high voltage supply, hardware trigger, and IR camera in a space-like environment [72]. It is used to measure the UV background of stars and artificial UV sources (GLS prototypes) at a flight altitude of about 40 km. The EUSO-Balloon consists of two square Fresnel lenses, and a single PDM. A FOV of about $\pm 6°$ can be reached. The first flight was on August, 25 th 2014. All instruments worked well and could be recovered from landing in a small lake. The about five hours of recorded data has been shipped in the course of August to Paris.

The latest prototype, Mini-EUSO, shall be installed in the Russian Zvezda module inside the ISS facing a UV transparent window pointed towards Earth. Mini-EUSO will consist of one PDM, two 20 cm in diameter Fresnel lenses, and a data acquisition system. The goals are to

- increase the technical readiness of JEM-EUSO components
- perform a test of in-flight calibration systems
- measure UV background and albedo at ISS altitude, and
- study atmospheric phenomena.
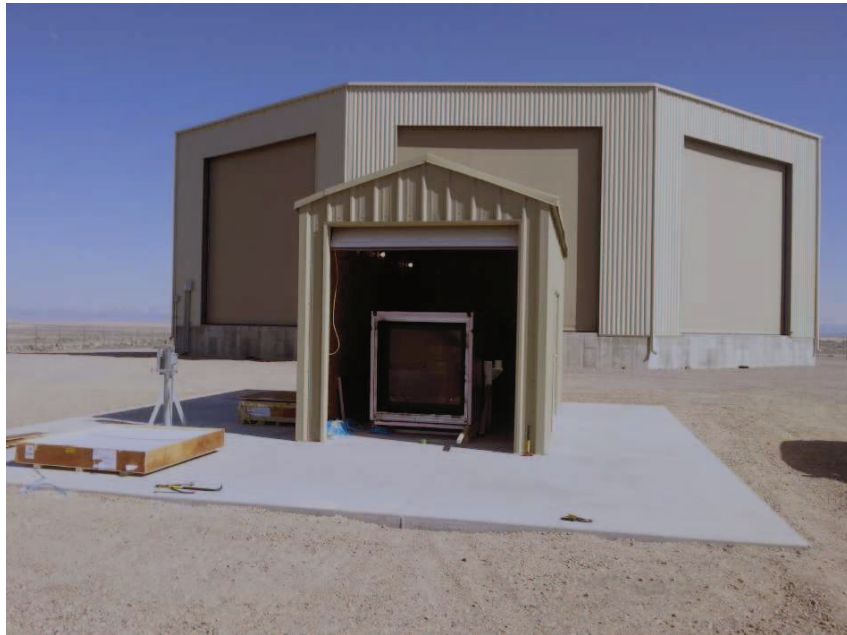
Figure 2.9: EUSO-TA in its housing located close to Black Rock Mesa at the TA in Utah (USA) [23].

Figure 2.10: EUSO-Balloon gondola for balloon flight prepared for launch in Timmins, Ontario (Canada) [26].

Physics of the Atmosphere

In astroparticle physics, the atmosphere plays an important part as a large calorimeter for detecting UHECR. For precise UHECR measurements, it is mandatory to monitor the state of this detector part as best as possible. The transmission of UV light is influenced by scattering and absorption, while the photon yield of both, nitrogen fluorescence and Cherenkov radiation is directly related to the state of the atmosphere which can be defined by, e.g., state variables (pressure, temperature, etc.), molecular composition, aerosol distribution, and ozone content. A brief introduction to atmospheric science, the most important atmospheric parameters, as well as basic transmission properties including the albedo of the Earth, will be given in this chapter.

3.1   Atmospheric Parameters

In atmospheric science, there are two frameworks describing the state of the atmosphere. The *Lagrangian description* pictures the atmosphere as consistent of many small air parcels interacting with their surroundings, undergoing transformations as they move. The *Eulerian description* is favored for numerical solutions, which describes the instantaneous state of the atmosphere by a set of thermodynamical state variables, e.g., temperature T, air pressure p, relative humidity u, and a set of dynamic variables such as the velocity components of wind, or the balance of incoming and outgoing radiation. The latter description shall be used in this work.

General aspects of the atmosphere are already given by Earth itself. Its gaseous and solid components are bound by the Earth's gravitational potential forming characteristic, horizontal layers. Large scale circulation is induced by Earth's rotation giving rise to transport of constituents. Atmospheric state variables are given in either geopotential height H (gpm, geopotential meter), or levels of equipotential pressure, while the Global Positioning System (GPS) uses the geometrical height z above the reference ellipsoid. The definitions shall be given in the following.

According to Federal Meteorological Handbook [69], the geopotential height is defined by rescaling the geopotential Φ_{geo} to mean sea level at a given geographical latitude Θ, and height n

$$H_n = \frac{1}{g_0}\Phi_{\mathrm{geo}} = \frac{1}{g_0}\int_0^n g(\Theta, z) \cdot \mathrm{d}z, \tag{3.1}$$
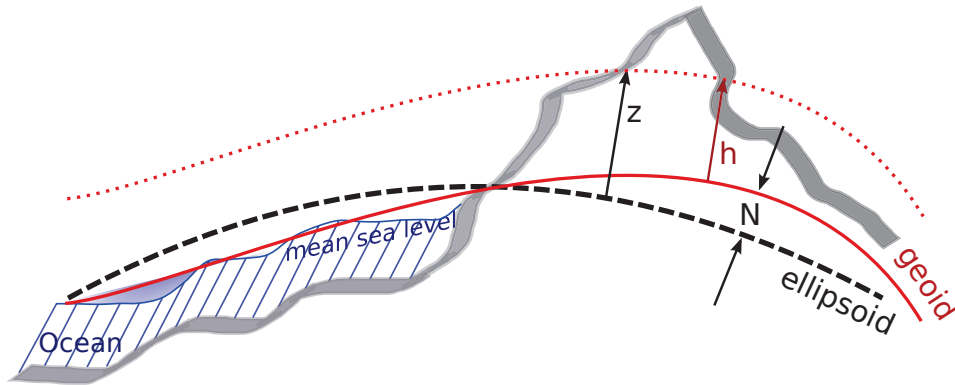
Figure 3.1: Various definitions of height. The geometrical height z is defined above the ellipsoidal surface. The orthometrical height h above the geoid. The local difference between both is the undulation factor N.

with the gravity at latitude Θ

$$g_\Theta = g_0 \cdot (1 - 0.002637 \cdot \cos(2\Theta) + 0.0000059 \cdot \cos^2(2\Theta)), \qquad (3.2)$$

and $g_0 = 9.80616\ \mathrm{m\,s}^{-2}$. This converts to the orthometrical height

$$h = \frac{H \cdot R_\mathrm{E}}{\Gamma_\mathrm{r} - H}, \qquad (3.3)$$

with the radius of Earth's major axis R_E[5], and the gravity ratio

$$\Gamma_\mathrm{r} = \frac{g_\Theta}{g_0} \cdot R_E. \qquad (3.4)$$

The geometrical height z above the reference ellipsoid can be derived by adding an undulation factor N that accounts for the local offset between geoid model, typically Earth Gravitational Model 2008 (EGM 08), and the reference ellipsoid, standardized by the US National Imagery and Mapping Agency (NIMA) and called World Geodetic System 1984 (WGS 84) [63]

$$z = h + N. \qquad (3.5)$$

The geoid is a model of the equipotential surface of the Earth. It becomes evident in the mean sea level (Fig. 3.1). Due to density variations, e.g., gravity anomalies, and land mass distribution, the undulation can reach ± 100 m locally and varies about ± 30 m over a range of $1\,000$ km. An interface for EGM 08-WGS 84 conversion, and retrieving local undulation factors in C++ is provided by `GeographicLib` [49].

The general behavior of atmospheric pressure can be approximated from the concept of *hydrostatic balance*

$$\frac{\mathrm{d}p}{\mathrm{d}z} = -\rho \cdot g(\Theta, z). \qquad (3.6)$$

---

[5]$R_\mathrm{E} = 6\,378\,137$ m [63]

This differential equation is solved by the exponential function

$$p(z) = p_0 \cdot \exp\left(-\int_0^{z_{\max}} \frac{dz}{H(z)}\right), \qquad (3.7)$$

with *scale height*

$$H(z) = \frac{R \cdot T(z)}{g(\Theta, z)}. \qquad (3.8)$$

The slope of the exponential pressure function varies slightly with temperature.

A common description of dry air by means of temperature, pressure and density profiles is given by the U.S. Standard Atmosphere 1976 (US-StdA 76) [62]. It is a model of the atmosphere developed by the United States NASA, released in 1976, comprising measurements of a full solar cycle and a theory for the upper atmosphere ($100 - 1000$ km), though temperature is thermally defined only for the region below 100 km. The temperature profile can be divided into five layers (Fig. 3.2) assuming a broken linear function of geopotential height H. In Eq. (3.8), the latitude is at $45°$ and $z = 0$ (mean sea level). The corresponding standard temperature at sea level is supposed to be $15°$C.

The lowest layer of the atmosphere is named *troposphere*. All typical weather phenomena, and the air shower development occur there. Its thermal behavior is dominated by surface heating and heat radiation. At about 15 km, the *tropopause* marks the end of the troposphere, with almost constant temperature over several kilometers in altitude. Increasing temperature determines the *stratosphere*. Cause to this heating are mainly chemical processes in response to incoming radiation and ozone. Its upper boundary lies around 50 km, and is accordingly called *stratopause*. Temperature declines again within the *mesosphere*, since ozone heating weakens. The mesosphere is concluded by the *mesopause* at around 86 km. Above, air molecules are typically ionized due to solar radiation. Recombination and sinking of air to lower layers during night hours leads to a phenomenon named *air glow*.

3.1.1 Molecular Composition

Air is composed of nitrogen, oxygen, and argon, as well as several trace gases[6] [76]. Such a general description of air that neglects water vapor, is called *dry*. Because the distribution of water vapor in the troposphere is highly variable in time and space, it will be treated separately. These main constituents are homogeneously distributed throughout the region below 100 km, named *homosphere*. Within this region, the mean molar mass of air is constant[7]. Above the *homopause* where convective mixing ceases, the mean molar mass is monotone decreasing (Fig. 3.3). This region is called *heterosphere*.

The density ρ of the atmosphere plays an important role regarding EAS detection with the air fluorescence method. In thermodynamic equilibrium, all constituents i of air will follow the *ideal gas law*

$$p_i \cdot V_i = n_i \cdot R \cdot T, \qquad (3.9)$$

---

[6]Composition of molecular mass of dry air: 78% N_2; 20.5% O_2; 0.93% Ar; 0.04% CO_2

[7]$M_{air}^{dry} = 28.06 \, \mathrm{g \, mol^{-1}}$
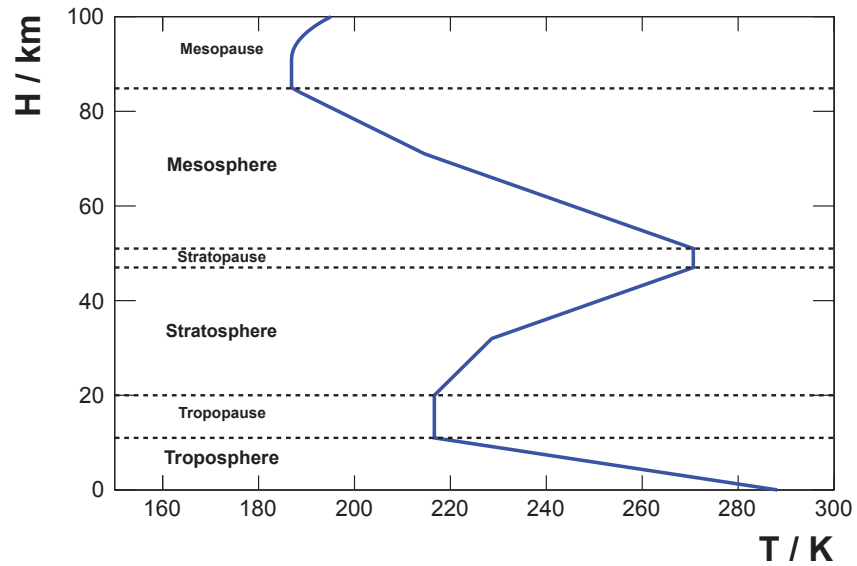
Figure 3.2: Temperature profile as parametrized based on US-StdA 76. The different thermal spheres and pauses in the homosphere below 100 km can be distinguished well.
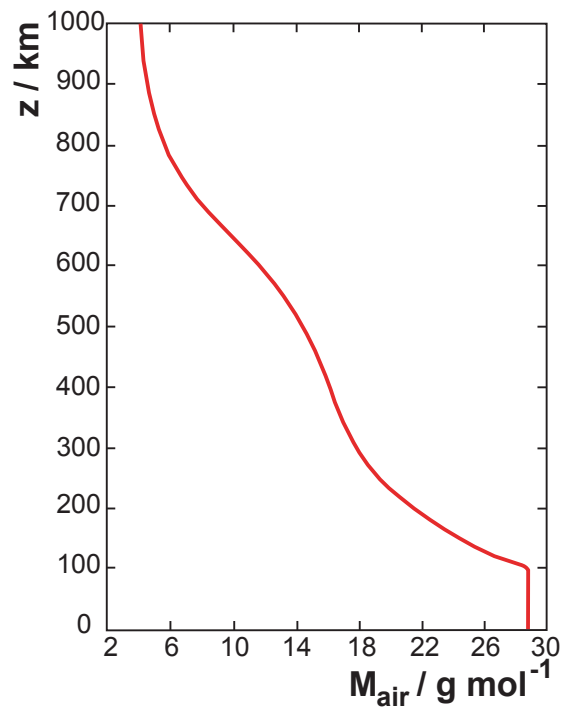
Figure 3.3: Mean molecular weight as a function of geometric altitude, published in US-StdA 76 [62].

with number of particles n_i, universal gas constant R and volume V_i. By introducing the molar mass $M_i = \rho_i \cdot V_i / n_i$, Eq. (3.9) can be rewritten

$$\rho_i = \frac{p_i \cdot M_i}{R \cdot T}.$$
(3.10)

As ideal gases serve *Dalton's law*, the molecular density of dry air reads

$$\rho_m^{\text{dry}} = \frac{p \cdot M_{\text{air}}^{\text{dry}}}{R \cdot T},$$
(3.11)

with the relative abundance ϕ_i of constituent M_i

$$M_{\text{air}}^{\text{dry}} = \sum_i \phi_i \cdot M_i$$
(3.12)
$$= 2 \cdot \phi_N \cdot M_N + 2 \cdot \phi_O \cdot M_O$$
$$+ \phi_{\text{Ar}} \cdot M_{\text{Ar}} + \phi_{\text{CO}_2} \cdot M_{\text{CO}_2}.$$

For calculating the density of moist air

$$\rho_m^{\text{moist}} = \frac{p \cdot M_{\text{air}}^{\text{moist}}}{R \cdot T},$$
(3.13)

it is necessary to estimate the proportion of water vapor in air

$$\phi_{\text{H}_2\text{O}} = \frac{e(\vartheta, u)}{p},$$
(3.14)

where e is the vapor pressure of water approximated with the empirical Magnus formula:

$$e(\vartheta, u) = \begin{cases} \frac{u}{100\% \cdot 6.1070 \cdot \exp\left(\frac{17.15 \cdot \vartheta}{234.9°C + \vartheta}\right)} & \vartheta \geq 0°C \\ \\ \frac{u}{100\% \cdot 6.1064 \cdot \exp\left(\frac{21.88 \cdot \vartheta}{265.5°C + \vartheta}\right)} & -30°C \leq \vartheta < 0°C \end{cases}.$$
(3.15)

All temperatures ϑ herein are in °C. The *relative humidity u* represents the degree of saturation of air with respect to the saturation vapor pressure. For consistency, $1 = \phi_{\text{dry}} + \phi_{\text{H}_2\text{O}}$ needs to be satisfied:

$$M_{\text{air}}^{\text{moist}} = (1 - \phi_{\text{H}_2\text{O}}) \cdot M_{\text{air}}^{\text{dry}} + \phi_{\text{H}_2\text{O}} \cdot M_{\text{H}_2\text{O}}.$$
(3.16)

3.1.2 Aerosol

A suspension of liquid or solid particles in air is referred to as *aerosol*. Aerosols are colloquially known as haze, smoke, fog, or smog, as they influence the optical transmittance of the atmosphere (for the corresponding scattering see Section 3.2.1). Many different species are gathered under this name (e.g., desert sand, sea salt, volcanic debris, fumes). Therefore the shape, occurrence, and size of aerosol particles varies over a wide range (1 nm to 100 μm in diameter) [54]. Their influence is not limited to the opacity of the atmosphere only, but also involves

thermal and chemical properties, e.g., aerosol particles act as condensation nuclei for ice and water droplets, later forming clouds.

Aerosols are divided into two main classes, *continental* and *marine*. In continental regions, sources of aerosols are combustion in industrial countries (mainly on the northern hemisphere), and biomass burning on the southern hemisphere. Marine aerosols consist mainly of sea salt, and their concentration is overall lower. The number density decreases with altitude. The amount of water vapor is a limiting factor to the concentration and persistence of aerosols in the troposphere. After volcanic eruptions, a high number density can be found throughout the stratosphere where aerosols can stay for long terms (e.g., several years).

3.1.3 Ozone

Ozone absorbs light in a wide range of wavelengths but is most efficient in the mid- and far UV-range. Since the most harmful UV radiation is absorbed by ozone in the upper atmosphere, it is one of the most important trace gases for (human) life on Earth. However, the dynamical processes in its formation-destruction cycle are still not fully understood. The former can be described by a two-step process,

$$O + O_2 \rightleftharpoons O_3^*,$$

$$O_3^* + M \rightarrow O_3 + M,$$
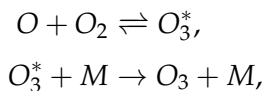
wherein the first process leaves O_3 in an excited state which becomes de-excited and hence stabilized in the following step. Beside a bunch of chemical destruction processes, the absorption of light quanta in the UV-range is one of the key factors. This photo-dissociation process reads as follows:

$$O_3 + \hbar\omega \rightarrow O + O_2.$$
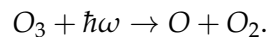
This ozone cycle was first proposed by Chapman in 1930 [25] and has been modified ever since accounting for known effects of ozone interaction with trace gases such as Chlorofluorocarbons (CFCs).

Ozone Distribution and Variance

Two different types of ozone can be distinguished. The *tropospheric ozone* and the *stratospheric ozone*. Mainly of anthropogenic origin, the former is known to cause respiratory and circulation disorders, and is therefore regarded as harmful. Stratospheric ozone gets quickly dissolved after sinking to the troposphere. A typical profile is displayed in Fig. 3.4a. The integrated amount of ozone

$$\Sigma_{O_3} = \int_0^\infty \rho_{O_3} dz, \tag{3.17}$$

referred to as *total column* or *column abundance*, is often given in Dobson units, paying homage to Gordon Dobson who invented the spectroscopic measurement technique for ozone in the 1920s. It refers to the thickness of a layer of gas at 0°C at normal pressure in units of 10^{-5} m. The mean global total column of ozone is 300 DU or a layer thickness of 3 mm.
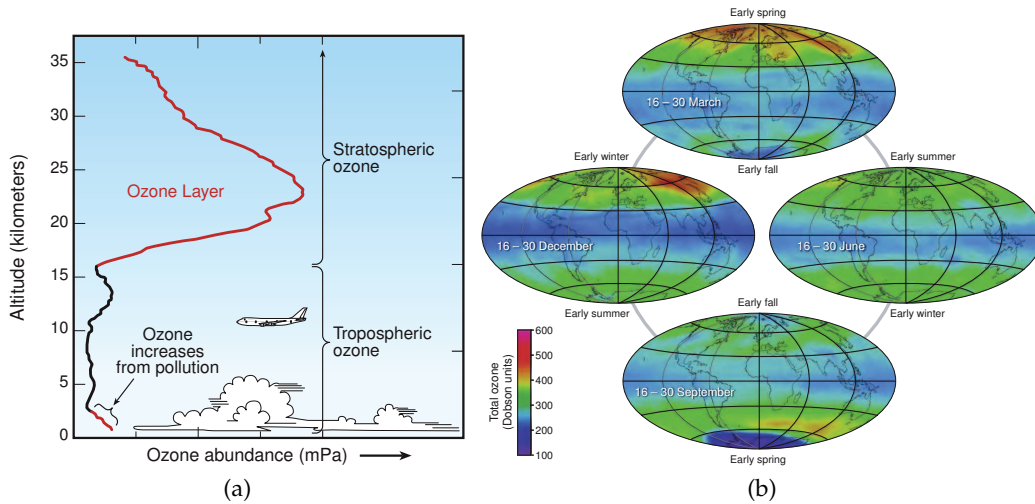
Figure 3.4: Ozone distribution. (a) The vertical ozone distribution profile in the atmosphere; (b) Global Satellite Maps of Total Ozone in 2009 in Dobson units (DU). Both taken from [36].

This amount of ozone in the atmosphere varies with season, latitude and longitude. In Fig. 3.4b, the mean total column ozone $\overline{\Sigma}_{O_3}$ from satellite measurements is shown for the whole globe. The seasonal maximum of ozone ($\approx$ 400 DU) is reached in early spring in the northern hemisphere, whereas the minimum there is in late summer. Although produced mainly in the tropics due to the high solar irradiance, most ozone is found at higher latitudes. $\overline{\Sigma}_{O_3}$ is about 250 DU close to the equator. This is in agreement with convective transport from its source region, making ozone distribution highly dynamic. Various anomalies have been observed, of which the ozone hole is infamous. The term describes the abnormal depletion of ozone above Antarctica, found for the first time in the 1980s. It is most pronounced during the Antarctic spring. Values of total ozone can drop by 2/3 of the global mean value. Probably less known are temporal increases, exceeding 500 DU [76], which can be seen in early winter above northeast Asia (Fig. 3.4b).

3.2 Transmission Properties

The atmosphere affects the transmission of light in various ways. Air molecules and aerosol particles interact with light in form of scattering. Multiple scattering on water droplets or ice crystals defines the optical appearance of clouds. Ozone acts most absorbent in the UV. By back-scattering (reflection), surfaces (natural or anthropogenic) can re-emit radiation towards space. The main concepts will be covered in the following section.

3.2.1 Scattering

Rayleigh Scattering

The basic treatment of scattering by molecules much smaller than the incident wavelength, is called *Rayleigh scattering*. It is assumed that molecules act as dipoles

$$\Phi_{\text{Rayleigh}}(\zeta) \; \text{—}$$

$$\Phi_{\text{Mie}}(\zeta) \; \text{—}$$

forward   forward

(a) Rayleigh   (b) Mie
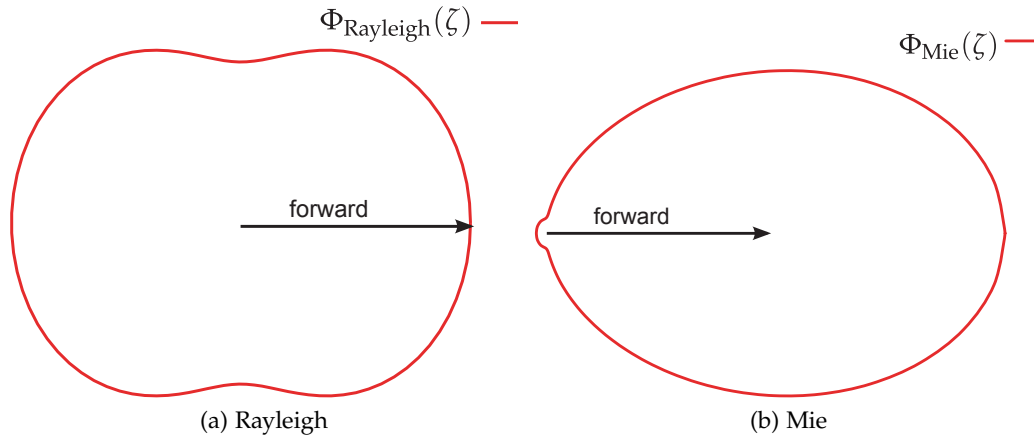
Figure 3.5: Polar plot of scattering phase functions. Forward scattering is indicated by an arrow.

towards incoming radiation. In the above limit of small particle size, it can be shown that the total scattering cross-section $\sigma(\lambda)$ is proportional to the wavelength λ^{-4} (e.g., Salby [76]). This implies that Rayleigh scattering is most effective for short wavelengths. The known Rayleigh phase function $\Phi_{\text{Rayleigh}}(\zeta)$ with respect to the scattering angle ζ

$$\Phi_{\text{Rayleigh}}(\zeta) = \frac{3}{4}(1 + \cos^2(\zeta)), \tag{3.18}$$

yields a strong back-/forward component, which is depicted in Fig. 3.5a. Incoming energy is spread equally to both, backward and forward spaces. However in Eq. (3.18), the polarizability of the scatterer ρ_n is neglected. Taking this into account the phase function takes following form

$$\Phi_{\text{Rayleigh}}(\zeta) = \frac{3}{4} \cdot \frac{1}{1 + 2\rho_n^\star(\lambda)} \cdot \left[(1 + 3\rho_n^\star(\lambda)) + (1 - \rho_n^\star(\lambda)) \cdot \cos^2(\zeta) \right], \tag{3.19}$$

with the wavelength dependent factor $\rho_n^\star(\lambda) = \frac{\rho_n(\lambda)}{2 - \rho_n(\lambda)}$ [21]. The dispersion of the polarization factor is displayed in Fig. 3.6. It rises steeply towards smaller wavelengths. For $\rho_n(\lambda) = 0$, Eq. (3.19) transforms to Eq. (3.18). Another aspect that needs to be taken into account, is the varying abundance of water vapor in the atmosphere. A parametrization for $\rho_n = \rho_n(\lambda, \chi_{\text{H}_2\text{O}})$, the wavelength and water vapor dependent polarization factor, is given by Tomasi et al. [85]. The optical depth $\delta(\lambda)$ of the atmosphere is described by an integral of the volume scattering coefficient $\beta(\lambda, z)$ over the total vertical column

$$\delta(\lambda) = \int_{z_0}^{z_\infty} \beta(\lambda, z) \cdot \mathrm{d}z, \tag{3.20}$$

with

$$\beta(\lambda, z) = N(z) \cdot \sigma_{\text{tot}}(\lambda, z), \tag{3.21}$$

where $N(z)$ is the number density, and $\sigma(\lambda, z)$ the total Rayleigh scattering cross section. The volume scattering coefficient follows an exponential trend (see Fig. 3.7).
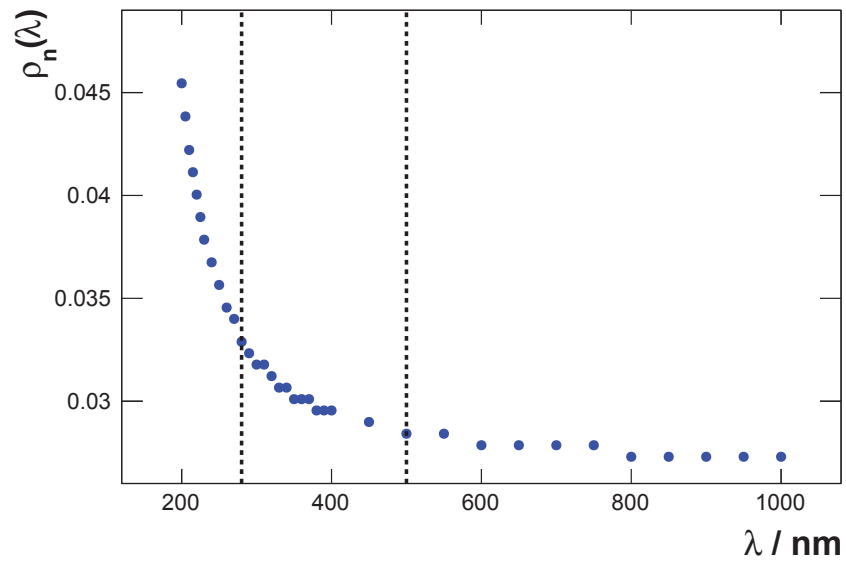
Figure 3.6: Dispersion of polarization factor with respect to wavelength [21]. The vertical lines mark the range of wavelengths of interest.
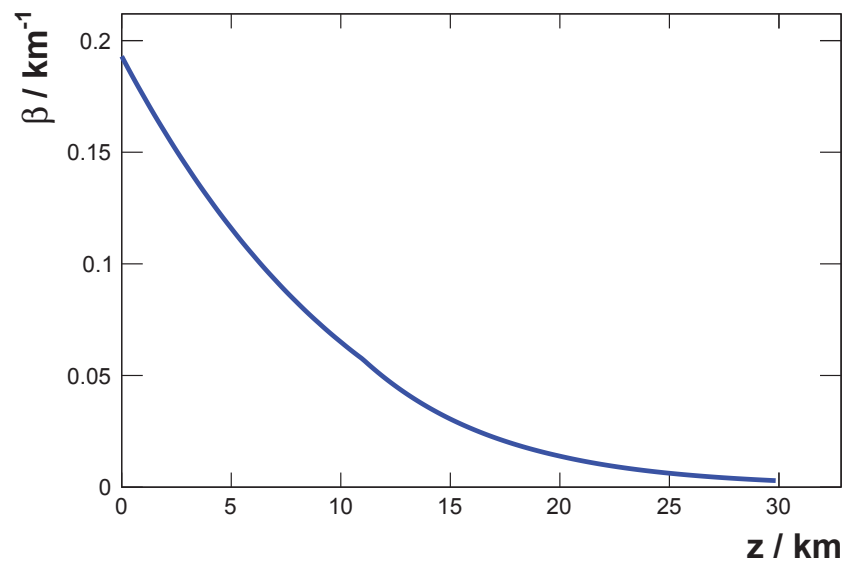
Figure 3.7: Volume scattering coefficient as function of altitude computed for US-StdA 76.

Mie Scattering

Aerosol particles differ in size and shape. A full analytical description is impossible, unless aerosols are approximated by homogeneous spheres. For particles larger than the wavelength of the scattering light, the approximation that led to Rayleigh scattering does not longer hold. A first full derivation for spherical, dielectric particles based on Maxwell's equations dates back to Gustav Mie in 1908 [58]. For large radii, Mie theory yields wavelength independent scattering, which causes clouds white appearance. A popular form for Mie type scattering was introduced by Henyey and Greenstein in 1941 [45]

$$\Phi(\zeta) = \frac{\gamma \cdot (1 - g^2)}{4\pi} \cdot \frac{1}{(1 + g^2 - 2g \cdot \cos(\zeta))^{\frac{3}{2}}}. \tag{3.22}$$

The parameter g describes the asymmetry in forward ($g = 1$) and backward ($g = -1$) direction, and γ the albedo of the homogeneous sphere. As proposed by Henyey and Greenstein, a linear combination of forward and backward scattering phase function is encouraged by measurements at the Pierre Auger Observatory [15]

$$\Phi(\zeta) = \frac{\gamma \cdot (1 - g^2)}{4\pi} \cdot \left[\frac{1}{(1 + g^2 - 2g \cdot \cos(\zeta))^{\frac{3}{2}}} + \frac{f \cdot (3\cos^2(\zeta) - 1)}{2 \cdot (1 + g^2)^{\frac{3}{2}}} \right], \tag{3.23}$$

with $\gamma = 1$. The phase function is depicted in Fig. 3.5b for $g = 0.6$ and $f = 0.4$. Since Mie scattering is in general strongly peaked in forward direction, it is not as important for an Earth orbiting telescope as for Earth bound detectors.

3.2.2   Absorption in the near UV

Absorption cross-sections of ozone have been measured by several groups over the past decades within the $200 - 1100$ nm regime [13, 20, 55, 60]. Four absorption bands can be distinguished in decreasing order of intensity [71]:

- Hartley band ($200 - 320$ nm),
- Huggins bands ($300 - 390$ nm),
- Chappuis band ($380 - 800$ nm),
- and Wulf bands (> 800 nm).

The definition of the corresponding intervals vary slightly in the literature. The absorption cross-section, as measured for differing temperatures, is displayed in Fig. 3.8. The absorption cross-section varies over seven orders of magnitude in the wavelength range $230 - 1070$ nm. A first maximum lies in the Hartley band at about 300 nm, followed by a rapid drop until a minimum is reached at about 380 nm, a second maximum is found at 600 nm, after which the cross-section decreases again towards higher wavelengths. The absorption cross-section in the wavelength range between 300 nm and 450 nm is most important for fluorescence light transmission. A decrease of the cross-section with temperature can be seen in Fig. 3.8b.
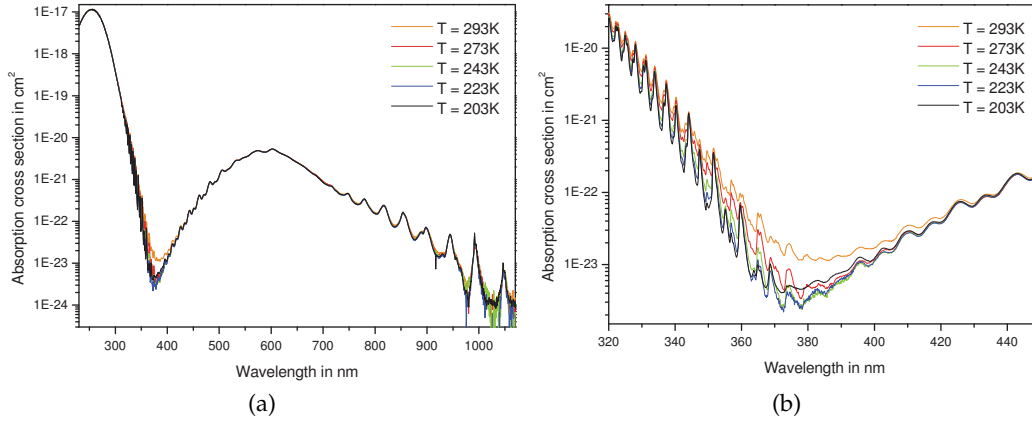
Figure 3.8: Absorption cross-section of ozone (logarithmic scale) for different temperatures [20]. (a) $230 - 1070$ nm range; (b) Main nitrogen fluorescence regime ($320 - 450$ nm).

A quadratic polynomial parametrization of the temperature dependence

$$\sigma(\lambda, \vartheta) = c_0(\lambda) + c_1(\lambda) \cdot \vartheta + c_2(\lambda) \cdot \vartheta^2, \tag{3.24}$$

was suggested by Bass and Paur in 1984 [13]. It reproduces the data to an accuracy better than 1% [71]. The temperature ϑ is given in $^\circ$C. Eq. (3.24) can be generalized inserting $\vartheta = T - T_0$:

$$\sigma(\lambda, T - T_0) = c_0(\lambda) + c_1(\lambda) \cdot (T - T_0) + c_2(\lambda) \cdot (T - T_0)^2, \tag{3.25}$$

with $T_0 = 230$ K. Values of the three parameters $c_{i=1,2,3}$ are displayed in Tab. 3.1 [60].

The ozone optical depth δ_{O_3} in the atmosphere is defined as

$$\delta_{O_3} = \int \sigma_{O_3} \cdot \chi_{O_3} \cdot \rho_m^{\text{moist}} \cdot ds, \tag{3.26}$$

with the pressure ratio of ozone $\chi_{O_3} = p_{O_3}/p$. Up to 60° in zenith angle, a *slant optical depth* can by defined geometrically by dividing by the cosine of the zenith angle

$$\delta_{O_3}^{\text{slant}} = \frac{\delta_{O_3}}{\cos(\theta)}. \tag{3.27}$$

The transmission coefficient is defined as

$$\tau_{O_3} = 1 - e^{-\delta_{O_3}}, \tag{3.28}$$

whilst the transmittance is

$$T_{O_3} = e^{-\tau_{O_3}}. \tag{3.29}$$

The wavelength-dependent effect of ozone on light transmission is shown in Fig. 3.9. A vertical incident direction and an arbitrary ozone profile of $\Sigma_{O_3} \approx 315$ DU have been assumed. At about 300 nm, less than 50% of light is transmitted. Above 320 nm, less than 10% of the light is absorbed by ozone.

Table 3.1: Ozone cross-section parametrization (Eq. (3.25)) in near UV $(300 - 400 \text{ nm})$ [60]. σ_{O_3} is given in units of 10^{-20} cm^{-2}.

λ (nm)	c_1	c_2	c_3
277.778 - 281.690	$4.0293 \cdot 10^2$	$4.3818 \cdot 10^{-2}$	0.0000
281.690 - 285.714	$2.7776 \cdot 10^2$	$6.3125 \cdot 10^{-2}$	0.0000
285.714 - 289.855	$1.8417 \cdot 10^2$	$-9.6665 \cdot 10^{-2}$	$2.1026 \cdot 10^{-4}$
289.855 - 294.118	$1.1300 \cdot 10^1$	$-1.0700 \cdot 10^{-1}$	$3.2697 \cdot 10^{-4}$
294.118 - 298.507	$6.5087 \cdot 10^1$	$-8.0018 \cdot 10^{-2}$	$2.2679 \cdot 10^{-4}$
298.507 - 303.03	$3.6161 \cdot 10^1$	$-6.7156 \cdot 10^{-2}$	$3.3314 \cdot 10^{-4}$
303.03 - 307.692	$1.9615 \cdot 10^1$	$-4.4193 \cdot 10^{-2}$	$2.0338 \cdot 10^{-4}$
307.692 - 312.5	$1.0459 \cdot 10^1$	$-2.8831 \cdot 10^{-2}$	$1.3909 \cdot 10^{-4}$
312.5 - 317.5	5.4715	$-2.0092 \cdot 10^{-2}$	$9.8870 \cdot 10^{-5}$
317.5 - 322.5	2.7569	$-1.0067 \cdot 10^{-2}$	$2.9515 \cdot 10^{-5}$
322.5 - 327.5	1.3527	$-5.7513 \cdot 10^{-3}$	$1.1038 \cdot 10^{-5}$
327.5 - 332.5	$6.9373 \cdot 10^{-1}$	$-2.9792 \cdot 10^{-3}$	$3.1038 \cdot 10^{-6}$
332.5 - 337.5	$3.2091 \cdot 10^{-1}$	$-1.9502 \cdot 10^{-3}$	$5.6456 \cdot 10^{-6}$
337.5 - 342.5	$1.4484 \cdot 10^{-1}$	$-1.1025 \cdot 10^{-3}$	$2.8818 \cdot 10^{-6}$
342.5 - 347.5	$7.5780 \cdot 10^{-2}$	$-5.7359 \cdot 10^{-4}$	$1.6055 \cdot 10^{-6}$
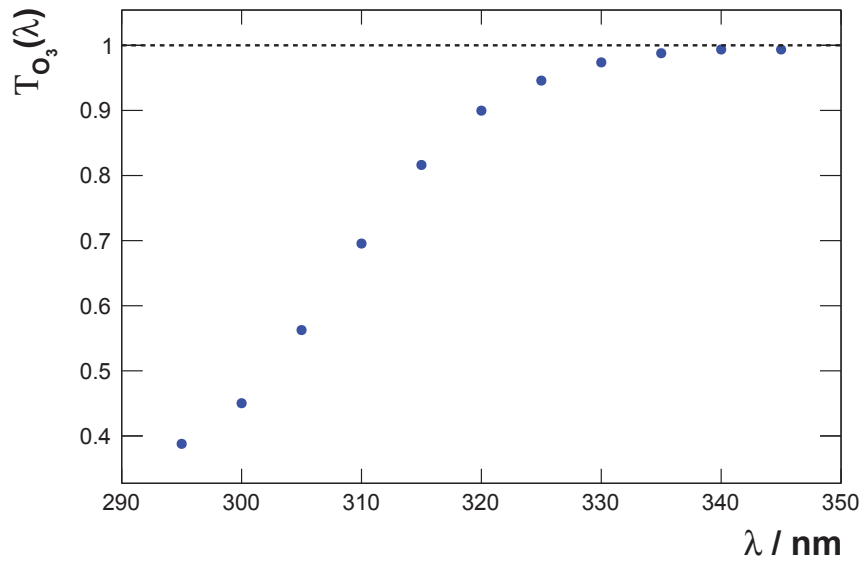
Figure 3.9: Wavelength dependent transmission of ozone based on the parametrization given in Tab. 3.1, assuming light propagation vertically from ground to an altitude of 400 km.

3.2.3 Albedo

In atmospheric science, the ratio between integrated incoming radiation and outgoing radiation, diffusely reflected from the Earth's surface, is called *albedo*. It is dimensionless, typically given as percentage, ranging from 0 (no reflection) to 1 (full reflection). Most surfaces have a high absorption in the UV band, and reflect neither strictly specular nor diffuse. A more thorough description of reflection is provided by bidirectional reflectance distribution functions (BRDFs) [68].

Mean albedo values in the UV regime for different natural and anthropogenic surfaces including cloud are listed in Tab. 3.2. The average cloud albedo measured by satellite instruments of about 60% [27] is only rivaled by snow with an albedo between 62% − 94% measured at ground level [24].

Table 3.2: Mean albedo of natural and anthropogenic surfaces in the UV-regime. Standard deviations as given by the corresponding authors.

Surface	UV-A (320 − 390 nm)	UV-B (280 − 320 nm)
Desert*	0.13±0.03	0.09±0.02
Savannah*	0.02±0.01	0.02±0.01
Forest*	0.09	0.05
Fresh snow*	0.94	0.88
Old snow*	0.66	0.62
Urban*	0.09	0.06
Water*	0.07±0.02	0.05±0.01
Total cloud[†]	0.56 ± 0.20	
Low cloud[†]	0.52 ± 0.16	
Mid cloud[†]	0.57 ± 0.16	
High cloud[†]	0.76 ± 0.14	

* [24], [†] 370 nm [27]

Simulation Software Tools for JEM-EUSO

The ESAF Simulation and Analysis Framework (ESAF) dates back to 2002. It had been originally developed for the ESA EUSO project, discontinued in 2004. It is written in C++ but mainly based on ROOT [16,84]. Difficulties adapting to the ground based prototype of JEM-EUSO (EUSO-TA) were encountered lately. This motivated the development of a simulation framework based on the Auger $\overline{\text{Off}}\underline{\text{line}}$. A simulation chain for JEM-EUSO, as well as both prototypes (EUSO-TA, EUSO-Balloon) is currently under development. The software and its basic concepts will be summarized in this chapter. Enhancements to algorithms for computing atmospheric profiles for air showers with zenith angles above 70°, and extensions to the radiative transfer through the atmosphere, like the absorption of UV light by ozone, and reflection of light on ground, will be covered in more detail as important developments have been part of this thesis.

4.1 $\overline{\text{Off}}\underline{\text{line}}$ Framework

The $\overline{\text{Off}}\underline{\text{line}}$ framework has been originally developed for simulation, shower reconstruction, and analysis of fluorescence and surface detector data of the Pierre Auger Observatory [5,10,38]. It has been shown that the framework can be easily adopted to simulation of a space based observatory such as JEM-EUSO [18]. Except for the shower reconstruction algorithms, access to the framework has been granted to the JEM-EUSO collaboration by the Pierre Auger collaboration. The development of an adaption to the needs of JEM-EUSO simulation and reconstruction tasks has begun in March 2013.

The $\overline{\text{Off}}\underline{\text{line}}$ framework is written in C++. It makes use of the fast computing capabilities of C++, and benefits from object oriented software design. Any user can easily run or modify simulation and reconstruction applications. Four components make up the core of the framework:

- **Central configuration.** It manages all steering files used for a run.
- **Physics Modules.** They host the different algorithms for simulation and reconstruction.
- **Detector description.** It includes information about all detector components at the time of the run, e.g., atmosphere, pixel status, and several more.
- **Event data structure.** All results computed are shared between different modules using this structure.

The steering files used by $\overline{\text{Off}\underline{\text{line}}}$ are written in XML format, and managed by the `CentralConfig` singleton[8]. A set of recommended configuration files is available, e.g., `standardFdSimModuleConfig`, `standardFdIdealDetConfig`. The `CentralConfig` also allows for generating a single XML file with all configurations used for the simulation.

The physics and analysis related code is provided in a modular way. Many such modules are interchangeable, given the correct order. A sequence of modules is written in XML format. Each module is called by name enframed by XML tags, and accompanied by a short designation of the working group[9]. An example of the simulation chain for JEM-EUSO:

```
<module> EventFileReaderOG </module>

<module> EventGeneratorOG </module>

<module> FdSimEventCheckerOG </module>

<module> ShowerLightSimulatorKG </module>

<module> LightAtDiaphragmSimulatorKG </module>

<module> ShowerPhotonGeneratorOG </module>

<module> GroundReflectionSimulatorJG </module>

<module> TelescopeSimulatorJG </module>
```

The `EventFileReader` handles the reading of a variety of input file types, e.g., simulated showers from Conex [73] or CORSIKA [43]. The `EventGenerator` adjusts time, place, and shower geometry of the simulation run. A simple consistency check is done by the `FdSimEventChecker`. The `FdSimEventChecker` algorithms determine whether the generated event satisfies the constrains of the detector, e.g., the time stamp of the simulated event shall be within the range of the effective detector run-time. In case of the simulation of JEM-EUSO, it is necessary to compare the detector position to the simulated shower position, e.g., a shower simulated at the location of the Pierre Auger Observatory cannot be seen by a JEM-EUSO detector located above the Telescope Array in Utah. Finally, the Data Acquisition (DAQ) is created. The simulated DAQ contains in principle all telescopes that satisfy above the conditions. Given yield[10] and atmospheric condition, the `ShowerLightSimulator` computes the fluorescence/Cherenkov light produced by the EAS. The `LightAtDiaphragmSimulator` computes the radiative transfer of light from the shower to the diaphragm of the telescope, and generates 1D light traces for fluorescence light, Cherenkov light, scattered Cherenkov light, and if applicable laser light within the FOV of the telescope. The proper geometric check whether a shower is contained inside the FOV is done here. The `ShowerPhotonGenerator` generates photons from probability functions built from the light traces. The `GroundReflectionSimulator` will be described in detail in Section 4.3. It handles the reflection of light on ground. The `TelescopeSimulator` uses GEANT4 to track the photons through the telescope's optics and computes a simple detector response (Fig. 4.1).

---

[8]Software design pattern restricting the instantiation of a class to one object.

[9]`OG` - Offline Group, `KG` - Karlsruhe Group, `JG` - JEM-EUSO Group

[10]e.g., AirFly [9,11], Nagano et al. [61]
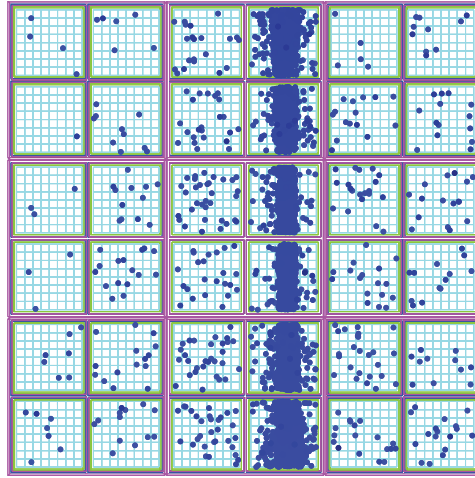
Figure 4.1: `TelescopeSimulator`. GEANT4 simulated hits on a PDM installed at EUSO-TA. A vertical Central Laser Facility (CLF) event has been simulated.

The detector description represents the physical entities of the real detector, including latest information about the atmospheric conditions, and the observed scenery, e.g., cloud fraction and ground properties. The actual detector varies according to the flavor of EUSO (JEM-EUSO, EUSO-TA, EUSO-Balloon, and Mini-EUSO). It follows in principle the physical hierarchy of the detector presented in Section 2.2. An interface to the IR-camera data is also provided. In the future, an interface for the LIDAR data will probably be included. The atmospheric data (details in Section 5.1) are either available from databases or can be read in tabular form from an XML steering file. The scenery information is divided into ground properties (albedo and scattering phase function) and cloud (optical thickness and dimension). The former is currently a simple parametrization, described in more detail in the following sections. The latter retrieves information from the Geostationary Operational Environmental Satellite (GOES). Technically, the acquisition is handled by *managers*. Each manager provides a link to an additional source of data, e.g., database, XML files. XML files contain static parameters, while the database content is updated with time. The managers are organized hierarchically in a chain of responsibility with the `ManagerRegister` serving as dispatcher. A request for data from the interface classes is handed down from the `ManagerRegister` until a manager is able to retrieve the data.

The event data structure holds the shared information between modules during run-time. It is decoupled from the persistent output data which is typically written to ROOT format. The event is split into the fluorescence detector event (`FEvent`), the air shower reconstruction data (`ShowerRecData`), and the shower simulation data (`ShowerSimData`) (Fig. 4.2). The `FEvent` follows the same physical hierarchy as in the detector description.

The geometrical appearance of the Earth is neither flat nor strictly spherical. Its shape can be approximated by a geocentric, oblate spheroid, standardized as WGS84, and displayed in Fig. 4.3. For a detector spread over about 3000 km^2 like the Pierre Auger Observatory or a telescope orbiting the Earth, the curvature of the Earth cannot be neglected. The longitudinal curvature κ at the equator is about $1.57 \cdot 10^{-4}$ km^{-1}, compared to $\kappa = 2.55 \cdot 10^{-4}$ km^{-1} at a latitude of $52°$.
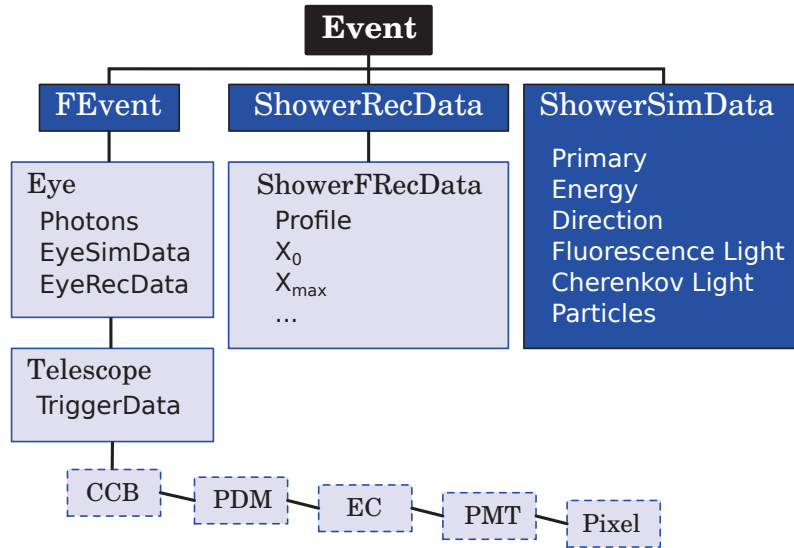
Figure 4.2: Scheme of the $\overline{\text{Off}\underline{\text{line}}}$ event structure. The `FEvent` holds the data of the fluorescence detector following the physical hierarchy. The `ShowerRecData` holds computed reconstruction values, e.g., X_{max}, X_0. The `ShowerSimData` holds the information read from shower simulation, e.g., Conex [73], CORSIKA [43], and computed light production.
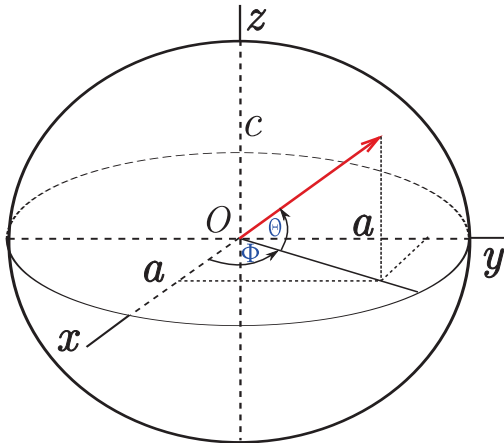
Figure 4.3: Reference Ellipsoid (WGS 84) of the Earth's surface. Semi-major axis or equatorial radius a and semi-minor axis or polar radius c, latitude Θ and longitude Φ.

These numbers translate into a ground distance of about 111 km/° at the former, and about 68.4 km/° at the latter. To account for these varying geometric factors during the computation of the slant depth of showers with zenith angles above 60°, it is necessary to do all calculations within the reference frame of WGS 84. Among many tools, the geometry package shipped with the $\overline{\text{Off}\underline{\text{line}}}$ is therefore quite utile. The `Geometry` package provides abstract geometrical objects like planes, lines, points, and vectors. It can perform intersections, point and cross-products. Different local Cartesian coordinate systems can be defined. By default the x-axis is pointing eastward, the y-axis northward and the z-axis upward. The orientation can be changed by rotation. The transformation of the geometrical objects from one coordinate system to the other is done in the background.

A `TabulatedFunction` is a special `class` to hold a collection (x, y) of points and provide interpolation between them. It also provides sums of x or y. An integration algorithm has been added in the course of this work.

4.2 Atmospheric Profiles for Inclined Shower Incidences

The original algorithm used for calculating the inclined atmospheric profiles was rather slow [4]. A fast computation of the atmospheric depth of air showers with zenith angles exceeding $70°$ is relevant for studying the atmospheric influence on EAS detection from space. Therefore, the code has been revised, and a new algorithm developed.

The atmosphere shall be built of several layers of concentric ellipsoids with a local height z_i^{vert} with respect to the surface of WGS 84. Due to the curvature κ, the z_i^{vert} will slightly deviate from the flat Earth approximation

$$X(\theta, z) = \frac{X_{\text{vert}}(z)}{\cos(\theta)},$$ (4.1)

as will the local zenith angle θ_i with respect to the normal vector of the tangential plane I_i (see Fig. 4.4b). Starting at the top of the atmosphere z_0^{vert} at about 100 km, the atmospheric depth is computed iteratively in steps of $\Delta X_i^{\text{slant}} = 10\,\text{g cm}^{-2}$ along the shower axis, until the surface or in the case of upward going showers space (about 100 km) is reached. Technically, this is true as soon as the difference between the density $\rho_{\text{max/min}}$ and ρ_i changes its sign. The distance d along the shower axis is signed with regard to the intersection point at ground level or another arbitrary point on the shower axis – negative in case of approaching direction and vice versa in the case of leaving.

A simple system of linear equations has to be solved for intersecting a line

$$\mathbf{x} = x_0 + \lambda \mathbf{r}$$ (4.2)

with an ellipsoid

$$(\mathbf{x} - \mathbf{v})^\top \mathbf{A}^{-1}(\mathbf{x} - \mathbf{v}) = \mathbf{1}.$$ (4.3)

The eigenvalues of $\mathbf{A}^{-1}$ represent the square of the semi-axes a^2, b^2 and c^2. In a geocentric Cartesian coordinate system, with b equals a

$$\frac{x^2 + y^2}{a^2} + \frac{z^2}{c^2} = 1,$$ (4.4)

the linear equations yield a quadratic equation of the form

$$ax^2 + bx + c = 0,$$ (4.5)

with the three common solutions for a discriminant $\Delta = b^4 - 4ac$:

$$\Delta \begin{cases} > 0 & \text{two intersections,} \\ = 0 & \text{earth skimming,} \\ < 0 & \text{no intersection.} \end{cases}$$ (4.6)

To adapt to the coding convention of the $\overline{\text{Off}}\underline{\text{line}}$, this calculation has been moved from the `InclinedAtmosphericProfile` to the `Geometry` package. A proper numerical treatment of the square root and cases has been implemented (according to [75]). The function returns a `vector` of intersection points $(0 - 2)$ for given reference ellipsoid, altitude, and line.

(a) Flat (b) Spheroidal
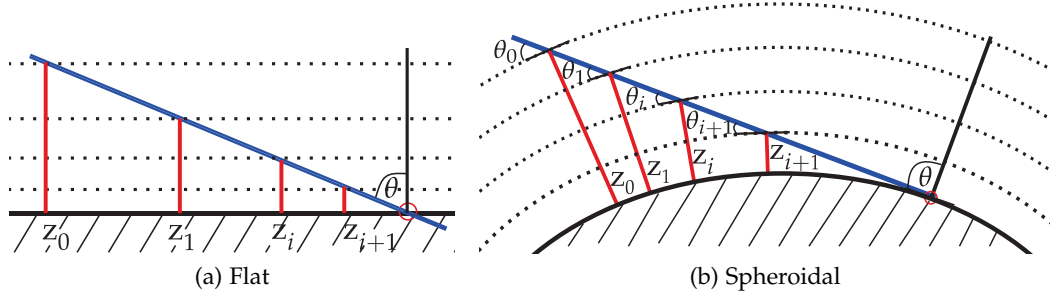
Figure 4.4: Reference surfaces for computation of inclined atmospheric profiles. (a) The atmospheric depth is computed from a vertical atmospheric depth profile using Eq. (4.1). (b) The atmosphere is build by ellipsoids concentric to WGS 84 with the height z_i^{vert}. The zenith angle θ of an EAS refers to the impact point on ground (empty circle), while θ_i are angles between the direction of the shower axis and the corresponding on-shell normal vector.

For each $\Delta X_i^{\text{slant}}$, a corresponding vertical depth

$$\Delta X_i^{\text{vert}} = \Delta X_i^{\text{slant}} \cdot \cos(\theta_{i-1}) \tag{4.7}$$

is calculated. The local height z_i^{vert} is interpolated from the known `TabulatedFunction`, which relates the vertical height with the vertical slant depth. The corresponding θ_i is computed as stated above. For a horizontal shower ($\theta \geq 80°$) the corresponding geometries are shown in Fig. 4.4.

The performance of the new algorithm has been tested by means of speed and reliability. Within a range from 0 to 85° in zenith angle, the slant depth based on the US-StdA 76 has been calculated. A deviation from CORSIKA results of less then 0.03% was found (see Tab. 4.1). The time for computing the slant profile for a shower simulated with Conex in the zenith angle range from 0 to 89° has been logged on the same machine for the old and new algorithm. The new algorithm is about 10% faster for small zenith angles, but exceeds the old one by a factor of about eight at large zenith angles.

Table 4.1: Deviation between $\overline{\text{Off}\underline{\text{line}}}$ and CORSIKA for US-StdA 76 parametrization.

θ $(°)$	$X_{\text{curved}}^{\text{CORSIKA}}$ (g cm^{-2})	$X_{\text{curved}}^{\overline{\text{Off}\underline{\text{line}}}}$ (g cm^{-2})	Deviation (g cm^{-2})
0	1035.9	1036.1	0.20
30	1195.8	1195.9	0.10
45	1463.4	1463.5	0.10
60	2065.0	2064.8	0.20
70	3003.6	3002.9	0.70
80	5765.7	5763.5	2.20
85	10573.0	10569.0	4.00

4.3 Light Reflection on Ground

Because part of the light emitted will backscatter towards the telescope, the albedo or reflectivity of the surface plays a significant role for EAS observation from space. This characteristic footprint depends on the type, and orientation, of the surface encountered by the shower. The implementation realized within this work will be presented in the following.

A flat surface at an adjustable altitude with a homogeneous albedo has been introduced to the $\overline{\text{Off}\underline{\text{line}}}$ as a new class by the name Earth. The implementation of the interface is analogous to the Atmosphere. It can be configured using the EarthInterfaceConfig XML file. The albedos available are identical with the listed surface types in Tab. 3.2. A Test option allows for an arbitrary albedo by the user, e.g., homogeneous, optical thick cloud at a certain altitude. Two types of reflection are provided. According to the *Huygens-Fresnel principle*, backscattering on surfaces can be described by the superposition of spherical wave fronts. The phase function of such a point source is isotropic in the hemisphere of incidence (Fig. 4.5a), hence the number of photons dN within a solid angle element $d\Omega$ is constant

$$\frac{dN}{d\Omega} = \text{const.} \tag{4.8}$$

$$\Rightarrow N \propto \int d\Omega = 2\pi R^2. \tag{4.9}$$

The ideal diffusive reflection is described by the *Lambertian* distribution

$$\frac{dN}{d\Omega} = \cos(\theta) \tag{4.10}$$

$$\Rightarrow N \propto \int d\Omega = \pi R^2. \tag{4.11}$$

The intensity of light reflected is constant on a sphere depicted in Fig. 4.5b, with no reflection in the direction parallel to the surface of scattering. The Earth provides an interface to the ellipsoid-line intersection returning the point of intersection and a Boolean (false in case of no intersection). It is also possible to check whether a point lies below ground level. As displayed in Fig. 4.6, the original algorithm of the ShowerPhotonGenerator leads to a generation of photons below ground level. As enhancement, each photon's position has to be validated before the final creation using Earth member function IsUnderGround().
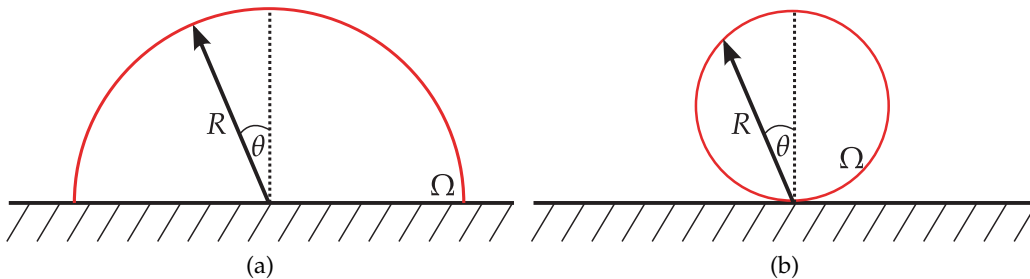
Figure 4.5: Phase functions of ground reflection. (a) Isotropic, e.g., point source, Huygens's principle. (b) Lambertian, e.g., ideal, diffusive scattering.
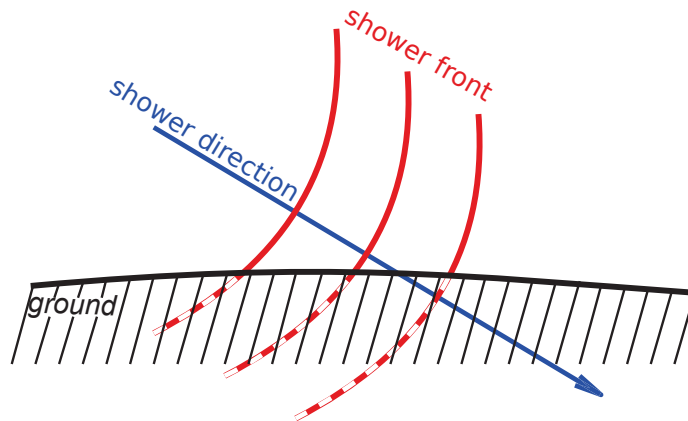
Figure 4.6: Photons are generated below ground level (dashed lines) in the original `ShowerPhotonSimulator`.

The `GroundReflectionSimulator` resorts to already implemented algorithms used for radiative transfer like Mie and Rayleigh attenuation, as well as the newly implemented ozone absorption (Section 4.4). Although the Cherenkov light is emitted continuously, the computation is realized for an adjustable, discrete range of wavelengths[11]. For both, fluorescence and Cherenkov light, the computation is iterative along the shower axis, accessing the previously calculated number of emitted photons (`ShowerLightSimulator`). A random direction of emission is drawn from the appropriate angular distribution, isotropic in case of fluorescence. The distribution assumed for the Cherenkov emission is taken from the parametrization of Nerling [67]. Only trajectories reaching the ground directly are of interest, placing a limit to the range of zenith angles in the fluorescence case. A reasonable number is $85°$. The number of traced bunches N_{sample} is computed in each step relative to the maximum number of bunches $N_{\text{max}}^{\text{raytrace}}$ which can be changed in the XML file, and the number of photons produced per iteration step N_γ^i

$$N_{\text{sample}} = N_{\text{max}}^{\text{raytrace}} \cdot \frac{N_\gamma^i}{N_\gamma^{\text{tot}}}. \tag{4.12}$$

The step width has been set to 100 ns in accordance to the standard value in `ShowerLightSimulator`. It is necessary that the binning is set identically for both modules. The JEM-EUSO native would be 2.5 µs, because of the Gate Time Unit (GTU). Each bunch is then propagated through the atmosphere taking attenuation into account. An intersection with the Earth ellipsoid at local ground level is calculated as described in the previous section. The intensity of the reflected light is a convolution of albedo and phase function in the direction of the detector. For ground based fluorescence detectors, reflection of isotropic or Lambertian type does not play a role.

The reflection phase functions have been compared by means of number of photons/m^2 reaching the aperture of the JEM-EUSO telescope at 400 km altitude. The photon numbers scale as expected from the ratio of photons per area (Eq. (4.9)-

---

[11]$280 - 451$ nm in steps of 9 nm
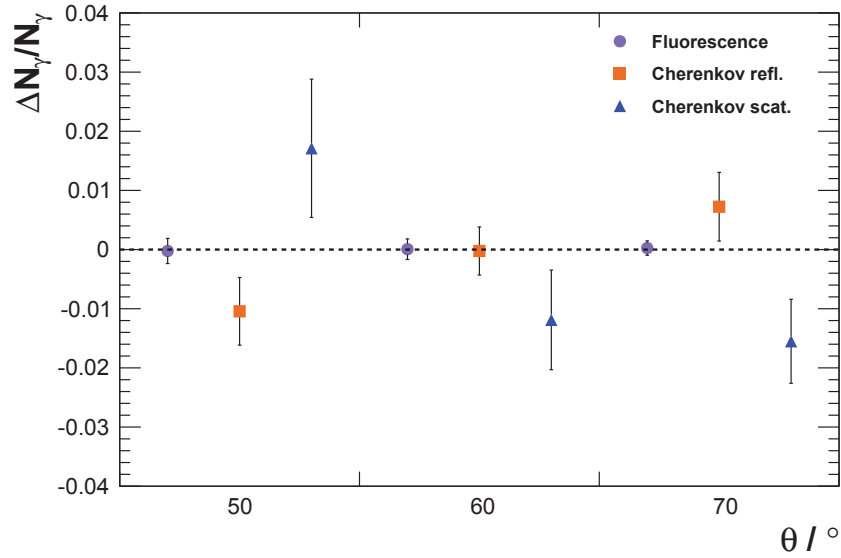
Figure 4.7: Influence of time binning on photon number at aperture. The average deviation for the different time binning $\Delta N_\gamma/N_\gamma$ as a function of zenith angle is shown for direct fluorescence light, ground reflected and scattered Cherenkov light.

(4.11)). In case of Lambertian reflection, the number of photons/m² is twice compared to isotropic reflection.

To study the influence of the time binning on the number of photons at the aperture, shower simulations at three different zenith angles (50°, 60°, and 70°) with 100 showers each have been done for the 100 ns and 2.5 μs binning. The average relative deviation

$$\frac{\Delta N_\gamma}{N_\gamma} = \frac{N_\gamma^{2.5} - N_\gamma^{0.1}}{N_\gamma^{2.5}}$$

as function of zenith angle is depicted for different light components in Fig. 4.7. The number of fluorescence photons is not influenced by the change in resolution. The deviation for components of the Cherenkov light varies between $\pm 1\%$ in case of ground reflected Cherenkov light and $\pm 1.7\%$ for the scattered Cherenkov. Given the standard deviation of the $\Delta N_\gamma/N_\gamma$, the deviation is not significant.

The numerical stability of the ground reflection simulation has been tested for one Conex shower (to prevent shower-by-shower fluctuations) at a primary energy of 10^{20} eV, a zenith angle of 50°, and a first interaction at about 13 g cm^{-2}. The result for $10\,000 \leq N_{\max}^{\text{raytrace}} \leq 500\,000$ is depicted in Fig. 4.8a. Above 350 000, the number of fluorescence photons decreases ($35 \rightarrow 12$) due to numerical restrictions in the implementation of the ray tracing. The upper limit for $N_{\max}^{\text{raytrace}}$ shall be set to 350 000 in the following. With respect to this limit, two factors shall be optimized, the smoothness and the computation time.

In Fig. 4.8b, the angular distribution of Cherenkov photon bunches is shown for different values of $N_{\max}^{\text{raytrace}}$. The plot in the right panel displays a value of 10 000, while the left panel depicts the plot for $N_{\max}^{\text{raytrace}} = 350\,000$ which is quite

smooth. The right panel plot displays many statistical artifacts that should be minimized. The data at $N_{\text{max}}^{\text{raytrace}} = 400\,000$ shall be regarded as reference optimum. The histograms have been normalized by division with the maximum count. The residual with respect to $N_{\text{max}}^{\text{raytrace}} = 400\,000$ has been calculated for each $N_{\text{max}}^{\text{raytrace}}$ in each angular bin. The standard deviation of these residuals is referred to as quality factor Q of smoothness.

In Fig. 4.8c, the quality factor is shown as function of $N_{\text{max}}^{\text{raytrace}}$. It follows an exponential trend, becoming less steep at about $N_{\text{max}}^{\text{raytrace}} = 60\,000$. At the same time, the computation time increases linearly with $N_{\text{max}}^{\text{raytrace}}$ and exceeds 100 s above $N_{\text{max}}^{\text{raytrace}} = 60\,000$ (see Fig. 4.8d). This value has be chosen for this thesis, because the angular distribution is smooth and the computation is fast ($t_{\text{run}} < 100$ s). For higher sampling rates, the value in the XML file can be changed.

Simulation results of photon time traces at the aperture of JEM-EUSO are shown in Fig. 4.9 for different zenith angles. Since multiple scattering is not implemented, the light curves end with the arrival of the Cherenkov flash. The fluorescence and Cherenkov peak separation depends on the zenith angle. In Fig. 4.9c, the Cherenkov flash is barely separable from first order Rayleigh scattered Cherenkov light.

(a)

(b)

(c)

(d)
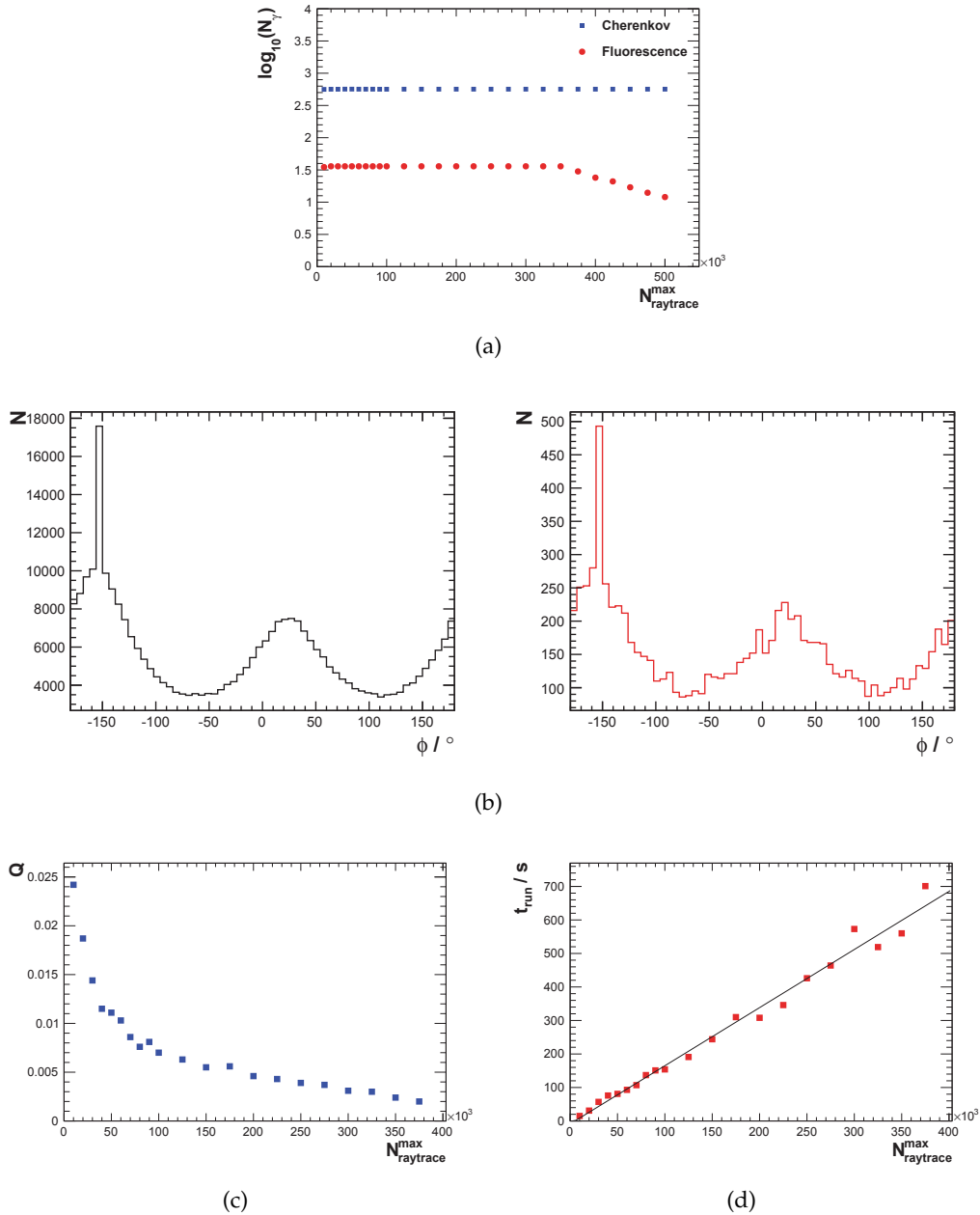
Figure 4.8: Check of the ground reflection simulation. (c) Quality of the angular distribution. (b) Quality of simulation by means of statistical artifacts in angular distribution of Cherenkov photons. Left panel: Azimuthal distribution at $N_{\text{max}}^{\text{raytrace}} = 350\,000$. Right panel: $N_{\text{max}}^{\text{raytrace}} = 10\,000$. (a) Stability of the number of simulated photons N_γ (fluorescence/Cherenkov) versus the maximum number of traced bunches. Above $350\,000$ the number of fluorescence photons drops. (d) The computation time increases linearly with $N_{\text{max}}^{\text{raytrace}}$ (above $60\,000$ $t_{\text{run}} > 100$ s).

(a) $\theta = 50°$
(b) $\theta = 60°$
(c) $\theta = 70°$
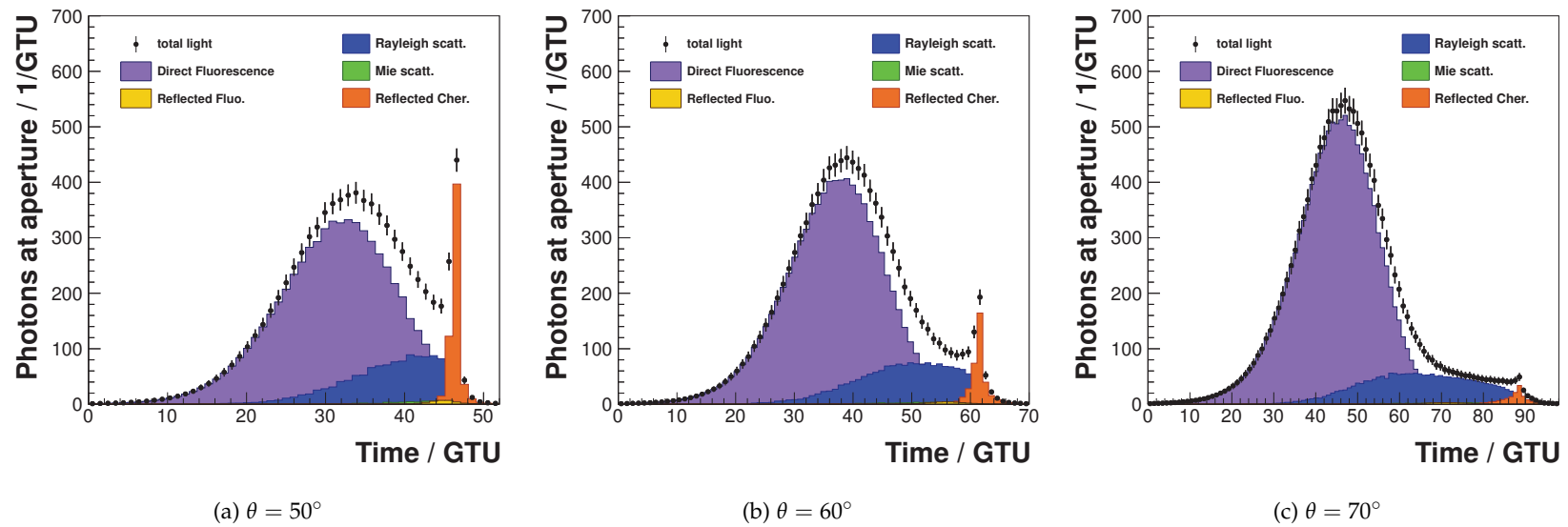
Figure 4.9: Light curves for various zenith angles. Contributions of different components, as simulated, are shown in differing color. The reflected fluorescence and Mie scattering components are very small.

4.4 Ozone Attenuation

Treating the attenuation of the generated light by ozone had not been foreseen in the original $\overline{\text{Off}}\underline{\text{line}}$ framework. The modular structure, however, allows for a straight forward implementation. The `Atmosphere` class serves as public interface to all atmosphere related methods provided by its subclasses. The implementation of the `OzoneModel` is loosely based on the `MieModel` and `RayleighModel`. A virtual `VOzoneModel` class inheriting from the virtual class `VModel` is defined. Every actual implementation of the `OzoneModel` has to inherit from `VOzoneModel`. Within `VOzoneModel` all methods are defined, which have to be implemented by each subclass

```
virtual AttenuationResult EvaluateOzoneAttenuation(...)
virtual double EvaluateOzoneAttenuation(...)
virtual double GetOzoneAttenuationLength(..)
virtual const ProfileResult& EvaluateOzoneDensityVsHeight()
virtual const ProfileResult& EvaluateOzonePressureVsHeight()
virtual double EvaluateTotalOzone().
```

Common member variables are also defined

```
ProfileResult* fTabOzoneDensityVsHeight
ProfileResult* fTabOzonePressureVsHeight
std::map<double,utl::TabulatedFunctionErrors>*
fTabOzoneOpticalDepth
mutable double fTotalOzone.
```

`AttenuationResult`, `ProfileResult` and `TabulatedFunctionErrors` are special subclasses of `TabulatedFunction`.

The current implementation of the methods is realized within the subclasses `ParametricXMLOzoneModel` and `OzoneModelOff`. The latter hosts dummy methods in case, the user wants to disable ozone attenuation in the atmosphere via the user interface. The `ParametricXMLOzoneModel` reads an XML file with a table of ozone pressure and height, stored in `fTabOzonePressureVsHeight`. The ozone data is described in Section 6.2. The attenuation is computed according to the equations Eq. (3.24)-(3.29) in Section 3.2.2. For each discrete wavelength, the attenuation as function of height had to be cached in `fTabOzoneOpticalDepth`. Without caching the computation time for a single shower simulation including ozone attenuation increased to roughly half an hour. Using the caching method the computation time has been reduces to a few minutes. In this context, an integration method based on the trapezoidal algorithm was added to `TabulatedFunction`.

4.5 Summary & Conclusion

A new algorithm for calculating the atmospheric depth of inclined showers has been developed and tested. At high zenith angles it performs 8 times better compared to the old algorithm. The maximum deviation from the parametrization used in CORSIKA is $4\,\mathrm{g\,cm^{-2}}$ at $\theta = 85°$.

A new class by the name `Earth` has been included to handle the light reflection from the Earth's surface. For the computation of the reflected component of Cherenkov and fluorescence light, the new module `GroundReflectionSimulator` has been developed. The module has been thoroughly tested.

A model for UV attenuation by ozone has been implemented as part of the atmosphere related algorithms. In this context, an integration algorithm has been added to the `TabulatedFunction` class based on the trapezoidal algorithm.

The work to fully adopt to the needs of JEM-EUSO is still ongoing. The supporting data structures are being reorganized and sub-components of the detector added. The JEM-EUSO $\overline{\text{Off}}\underline{\text{line}}$ will be able to provide a perfect platform for further simulation and reconstruction tasks, complementary to the existing ESAF.

Atmospheric Data for JEM-EUSO

The state of the atmosphere, and its state variables, as described in Chapter 3, has influence on the development of the air shower, as well as on the amount of light produced. Information about the current state can be received by conducting meteorological soundings at the site of an Earth-based observatory (e.g., Pierre Auger Observatory, TA). The effort, however, is huge. For an Earth-orbiting telescope, such as JEM-EUSO, real-time sounding is not feasible. The atmospheric monitoring group of the Pierre Auger Observatory has been using meteorologic *data assimilation* products successfully for many years. It has been shown that a high accuracy in air shower event reconstruction can be achieved [2]. For JEM-EUSO, however, the reconstruction results for X_{max} are expected to be roughly $100 \ \mathrm{g\,cm^{-2}}$ [12] [31]. The influence of states of the atmosphere diverging from the US-StdA 76 shall be studied in this section by means of atmospheric depth, and light emission. Exemplarily, a few locations within $\pm 52°$ geographical latitude have been selected, defined by the inclination of the ISS orbit. Boundary conditions, such as the wide FOV of JEM-EUSO, as well as the target EAS zenith angle range, on the selection of atmospheric profiles will be studied.

5.1   Global Atmospheric Models and Data Assimilation

Numerical solutions for the set of non-linear differential equations of the atmosphere are called GAMs. Based on spherical harmonics, GAMs work without boundary conditions. Big meteorological centers, e.g., US National Centers for Environmental Prediction (NCEP), and European Centre for Medium-Range Weather Forecasts (ECMWF), use their own GAM. The models' results differ only slightly [87]. All GAMs employ data assimilation techniques that consist of a continuous three step analysis cycle (Fig. 5.1). The real state of the atmosphere is determined by observation data from weather stations, ships, buoys, radiosondes, and satellites since the 1970s. Data reports are received every six hours. The GAM is used for a global short term forecast based on the current state of the atmosphere and simulation parameters of the previous cycle. In the analysis step, the model parameters are adjusted to the real state of the atmosphere. This is done by minimizing the deviation between weighted observation data and forecast. The result is a global 3D image of the state of the atmosphere.

  Long term observation data of all atmospheric parameters are re-analyzed periodically with state-of-the-art GAMs, e.g., NCEP Re-Analysis (R1/R2), ECMWF Re-Analysis (ERA) (ERA-15, ERA-40, ERA-Interim). Both can be accessed from the corre-

---

[12] $\theta = 60°$, $E = 10^{20}$ eV, $X_{\mathrm{max}}^{\mathrm{reco}} - X_{\mathrm{max}}^{\mathrm{real}} = 0^{+99}_{-89} \ \mathrm{g\,cm^{-2}}$
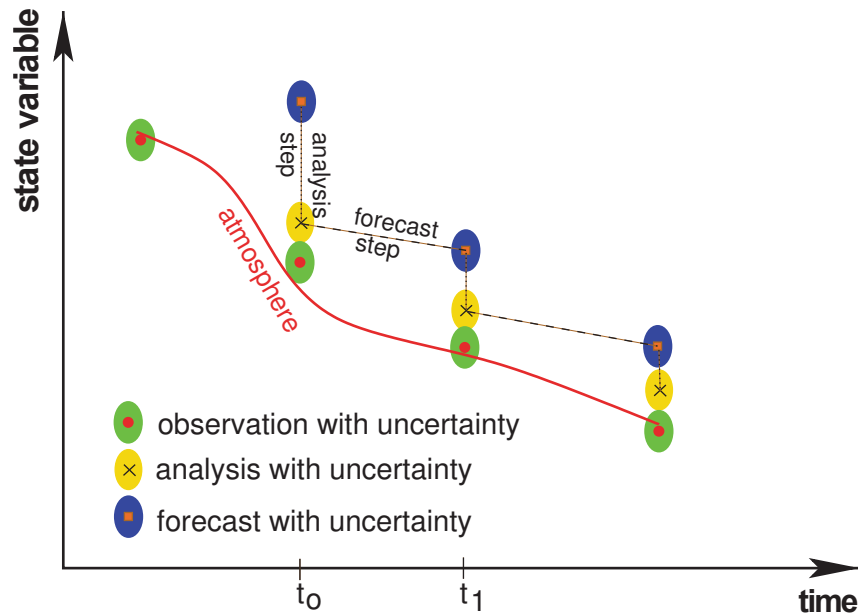
Figure 5.1: Data assimilation. The real state of the atmosphere is described by observation data, reported every six hours. State-of-the-art numerical weather prediction is used for short term forecast based on known atmospheric state. In the analysis step, the model is adjusted to the real atmosphere by assimilating data [2].

sponding institution's web page. In case of the ECMWF products, the open access is limited, e.g., the horizontal resolution of the ERA-Interim provided is $1.5° \times 1.5°$ compared to $0.75° \times 0.75°$ for full access. Full access to the whole archive via the Meteorological Archival and Retrieval System (MARS) can be granted by the national weather services (e.g., Deutscher Wetterdienst (DWD)). However, the access to the MARS is carried out by a one time key, generated with a *token*[13]. This is rather insufficient for remote access, e.g., scheduled update of atmospheric monitoring databases. The National Oceanic and Atmospheric Administration (NOAA) provides full open access to the regularly updated archive of it's Global Data Assimilation System (GDAS) [65]. Likewise, NCEP allows for full access of it's Re-Analysis (R1/R2). Compared to ERA-Interim, the NCEP-R2 cannot be considered as a state-of-the-art GAM, since it only corrects for known issues and errors of the NCEP-R1.

The data fields available from the above GAMs include temperature, pressure, geopotential height, and humidity, as well as wind velocity components, cloud cover, albedo, radiative flux, and several more. ERA-Interim provides additional information about the total column ozone and the cloud top altitude. The cloud top altitude is generally divided into three categories (low, middle and high). The levels listed in Tab. 5.1 refer to pressure levels. All atmospheric profile data from GAMs are available with respect to these. The altitude is typically given as geopotential height. In the following sections, GDAS data will be used, if not noted otherwise.

---

[13]a small, physical generator

Table 5.1: Comparison of open access meteorological products of NCEP/NOAA, and ECMWF.

	GDAS	Re-Analysis (R2)	ERA-Interim
Institution	NCEP/NOAA	NCEP	ECMWF
Time period	2004/12 - present	1979/01 - 2012/12	1979/01 - present
Temporal res.	3-hourly	6-hourly	6-hourly
Vertical res.	23 levels	28 levels	37 levels
Horizontal res.	$1° \times 1°$	$2.5° \times 2.5°$	$1.5° \times 1.5°$

5.2 Global Diversity of Atmospheric State

It is known that the variation of atmospheric state has significant influence on the detection and reconstruction of EAS events [2]. For better comprehension of the significance with respect to JEM-EUSO, ten sample locations have been chosen worldwide:

- Boulder   (USA; 40° N, 105°,W),
- Hilo   (USA; 19° N, 155° W),
- Pago Pago   (American Samoa; 14° S, 171° W),
- Timmins   (Canada; 48° N, 81° W),
- Pico   (Azores; 38° N, 29° W),
- Antofagasta   (Chile; 23° S, 70° W),
- Malargüe   (Argentina; 35° S, 69° W),
- Alëutian islands   (North Pacific; 52° N, 172° E),
- San Cristóbal   (Ecuador; 0° S, 89° W),
- Andaman island   (India; 11° N, 90° E).

The climate classification after Walter/Lieth, and Geiger/Köppen [33] has been used to distinguish different locations. Examples for Geiger/Köppen-diagrams of two selected locations are displayed in Fig. 5.2, wherein the monthly mean rainfall is depicted as histogram, and monthly mean temperature as line. According to Walter/Lieth (not depicted in the diagrams), the temperature (in °C) and rainfall (in mm) scale as 1:2. If the temperature lies above the rainfall graph, evaporation will be higher than rainfall and the climate will be classified as *arid* (marked as dotted area). If the opposite is true, the climate classification will be *humid* (marked as hatched area).

Malargüe, the site of the Pierre Auger Observatory on the southern hemisphere, is located on a high-altitude plane, at mid-latitude, in the southern temperate zone with the Andes to the west. It can be classified as arid, cold steppe climate after Geiger/Köppen.

Boulder is located at the foot of the Rocky Mountains at high altitude in the US state of Colorado. Like Malargüe, it is governed by a arid, cold steppe climate.

The city of *Antofagasta* is located in a transition zone of a humid ocean climate and the driest desert on Earth, the Atacama desert. Its climate is classified as cold desert.

(a) Malargüe   (b) Boulder
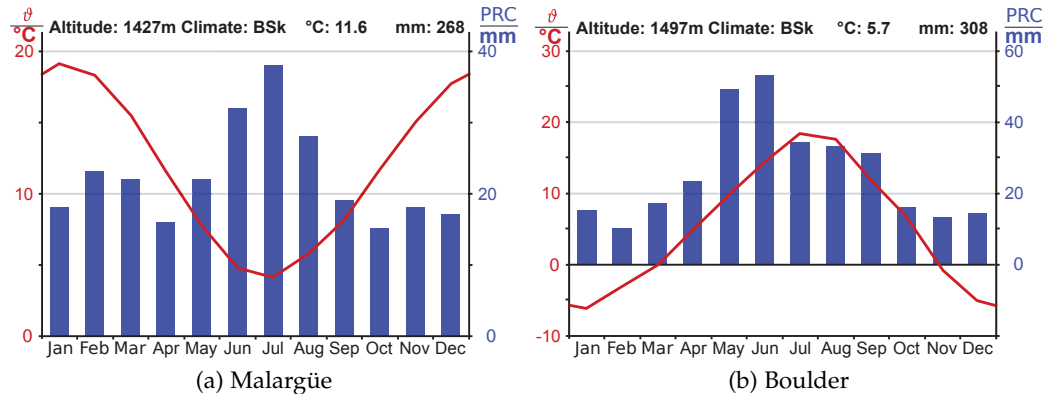
Figure 5.2: Climate diagram after Geiger/Köppen [6]. Monthly mean temperature (line, in °C), monthly mean rainfall (histogram, in mm). The ratio between temperature and rainfall scales as 1:2, following the climate diagrams after Walter/Lieth.

The launching site for the EUSO-Balloon, *Timmins* is located close to the Great Lakes in the state of Ontario, Canada. The climate is cold temperated and humid.
Between 52° N and 52° S approximately 82% of the Earth's surface is covered by ocean. For this reason, different places in midst the oceans have been chosen. *Pico* is located on the Azores islands, close to the Mid-Atlantic Ridge, with a warm humid, summer dry climate.
The *Alëutian islands* are at the northernmost observable region for the JEM-EUSO mission. They lie within a thermohaline sinking zone in the North Pacific between the shores of Alaska and east Siberia, with a humid, subarctic climate.
Hilo is located on Hawaii. Its climate is tropical and humid. The same holds for *Pago Pago*, which lies on American Samoa, south of the equator, *San Cristóbal* on the Galapágos islands, and *Andaman island* which belongs to India and is located in the Bay of Bengal. A global overview of the referred locations is given in Fig. 5.3.

The atmospheric model currently used for JEM-EUSO is the US-StdA 76. The air is assumed as dry herein (zero humidity at all altitudes). Therefore, all atmospheric profiles will be compared with respect to that model. The deviation of the mean spring GDAS profiles of atmospheric state variables are displayed in Figs. 5.4-5.6 for all above locations. "Spring" shall refer to April on the northern hemisphere and October on the southern. Boulder and Malargüe are highlighted blue/red. Both do not differ much in terms of temperature and pressure in comparison to the US-StdA 76, for it is evaluated at a latitude of 45° – about the same as Boulder and Malargüe. The largest positive deviation in spring pressure is found in data of Pago Pago and the Andaman island (also highlighted), while the largest negative deviation becomes visible in the data of the Alëutian islands. The latitude plays an important role herein. The further towards the equator or away from the evaluated latitude of the US-StdA 76, the greater the differences. Most of the locations are actually close to the equator, hence the overall positive deviation. Only two locations are further north. These are the Alëutian islands and Timmins, displaying a negative deviation. In terms of temperature, Pago Pago and the Andaman island is outstanding – warm close to the ground and cold in the upper troposphere.
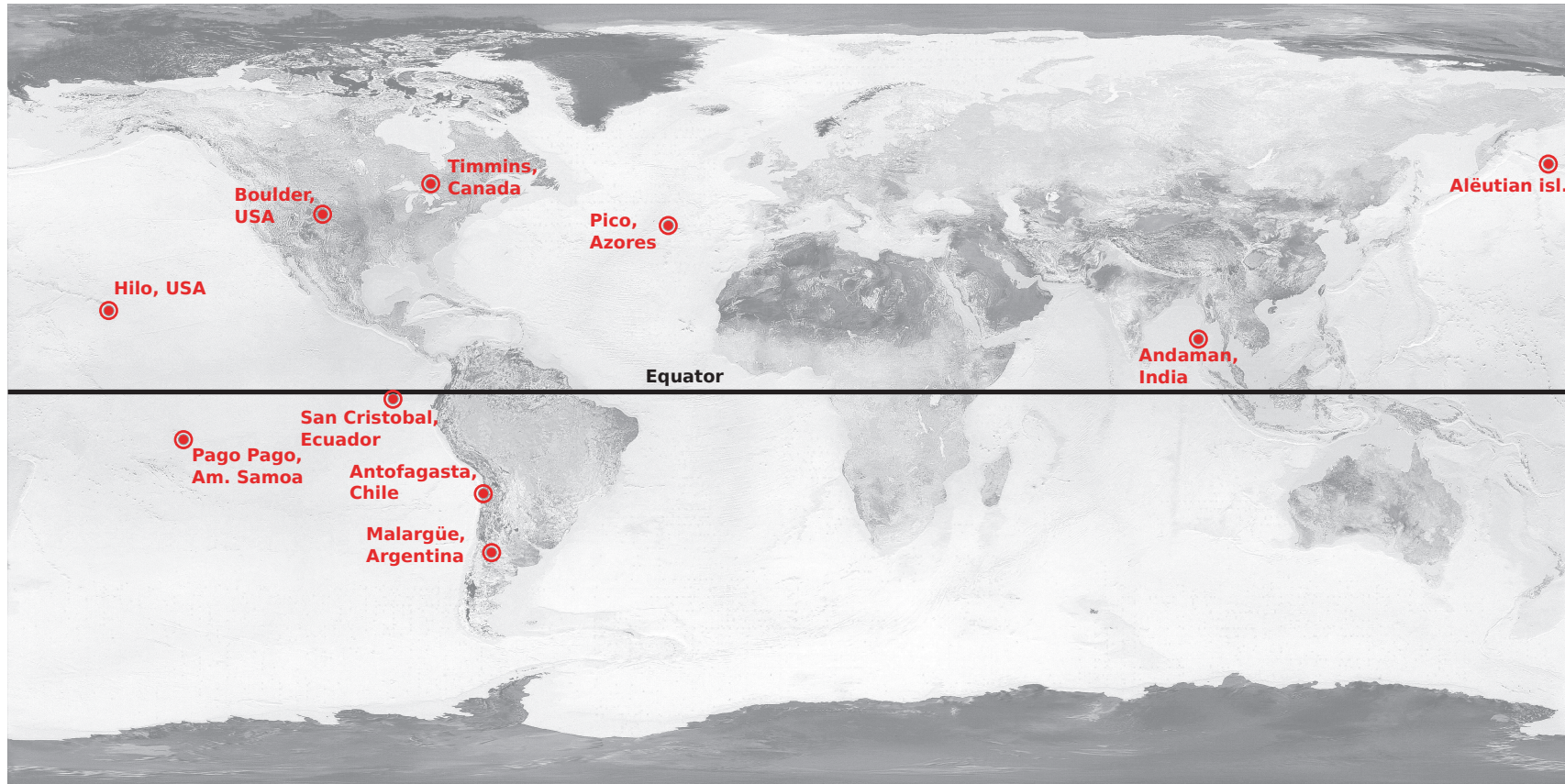
Figure 5.3: The chosen sample locations used in this section and the following. Boulder, Hilo (both USA), Pago Pago (American Samoa), Timmins (Canada), Pico (Azores), Antofagasta (Chile), Malargüe (Argentina), Alëutian islands, San Cristóbal (Ecuador) and Andaman island (India).

They also display the highest humidity (max. 80% in case of Andaman island). The Alëutian islands are cold at ground level, but warmer at higher altitudes.

For Boulder, the monthly mean atmospheric parameter profile deviations are displayed in Figs. 5.7-5.9. The largest deviation is actually found in data for July, while a low deviation appears in January. The corresponding profiles of the remaining locations are found in Appendix B.1.

The maximum of an EAS with a zenith angle of $0°$ is typically at about 3 km height, while at $60°$ zenith angle X_{max} is at about 7 km. The calculated vertical atmospheric depth profiles for Boulder are depicted in Fig. 5.10 (for the other locations consult Appendix B.2). At a height of 3 km, the deviation is about $12\,\mathrm{g\,cm^{-2}}$, increasing to about $25\,\mathrm{g\,cm^{-2}}$ at 7 km. All locations close to the equator display a similar positive trend in the deviation, with little variance over the year, while Timmins and the Alëutian islands display a negative trend. The largest deviations occur between $5-10$ km in altitude. The largest negative 3 km-deviation is found in data of the Alëutian islands in January ($\Delta X = -28\,\mathrm{g\,cm^{-2}}$), the largest positive deviation on the Azores islands in August ($\Delta X = 22\,\mathrm{g\,cm^{-2}}$). The maximum variance at 3 km between different months is at the Alëutian islands ($\Delta(\Delta X) = 30\,\mathrm{g\,cm^{-2}}$), the lowest in Antofagasta and on the Andaman island ($\Delta(\Delta X) = 2\,\mathrm{g\,cm^{-2}}$). Seasonally grouped profiles are displayed in Fig. 5.11.

The atmospheric influence on the photon emission has been studied exemplarily for Boulder and the Alëutian islands. Boulder has been chosen, since it is similar to the US-StdA 76 by means of geographical latitude, and the Alëutian islands as one of the most extreme locations. The monthly mean profiles of Boulder and the Alëutian islands have been processed with JEM-EUSO $\overline{\text{Off}\underline{\text{line}}}$ for a single Conex simulated shower of 10^{20} eV and zenith angle $0° \leq \theta \leq 70°$. The amount of fluorescence and Cherenkov photons emitted per m, as well as the total amount of photons as deviation from the average is displayed in Figs. 5.12-5.13 for a shower with a zenith angle of $60°$. In case of the Cherenkov light, only the emission of light with the wavelength 334 nm is displayed. In Figs. 5.12a-5.12b and Figs. 5.13a-5.13b, the emission profiles of fluorescence and Cherenkov light with respect to the distance from the shower core at ground level are displayed. A shift of the maximum with respect to the reference profile (US-StdA 76), is visible. On average, the maximum of the Cherenkov light is about 800 m closer to ground level, hence deeper in the atmosphere. The largest difference in position of one maximum to another is at the utmost $\sim 1\,300$ m (see Fig. 5.12b: December (957 m), October (-332 m)). In the lower panel, the deviation from the average of the integral amount of photons is shown by month. The largest variance from the average value of emitted fluorescence photons is about $\pm 3\%$ in both cases. The total amount of Cherenkov photons emitted varies by up to $\pm 4\%$. Throughout the year, there is less light emitted in winter, and more in summer. The emission in spring and fall is similar to the the US-StdA 76 case, as expected. Fluorescence and Cherenkov ratios of the integral amount of light behave similar. The relative difference of the shifted light profiles with respect to the US-StdA 76 is shown in Fig. 5.14. The wiggles displayed are numerical artifacts from interpolation of the data points of the profiles. All lines intersect at the position of the maximum of the US-StdA 76 light profile. For Boulder the deviation is almost positive in all cases at large distances, and negative after the intersection point. At the Alëutian islands,
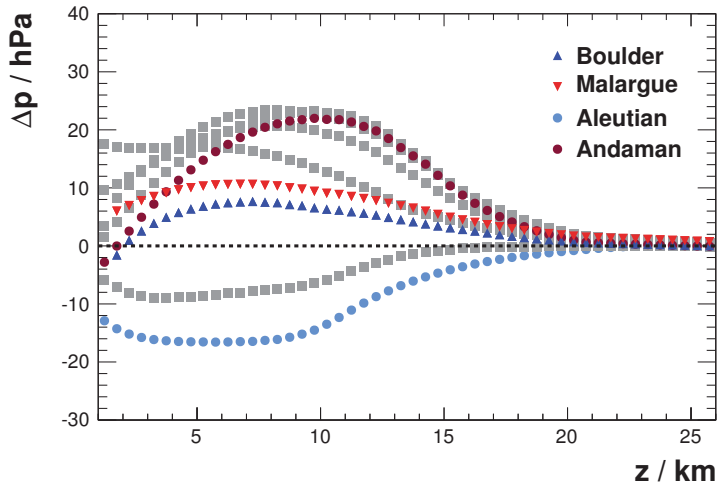
Figure 5.4: The deviation in atmospheric pressure with respect to US-StdA 76 for all locations. Boulder and Malargüe are highlighted, as well as Alëutian and Andaman island.
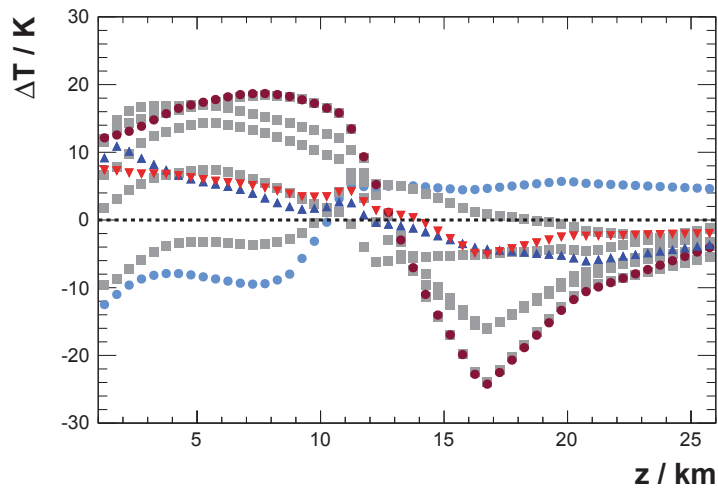
Figure 5.5: The deviation in temperature with respect to US-StdA 76. Boulder and Malargüe are highlighted, as well as Alëutian and Andaman island.
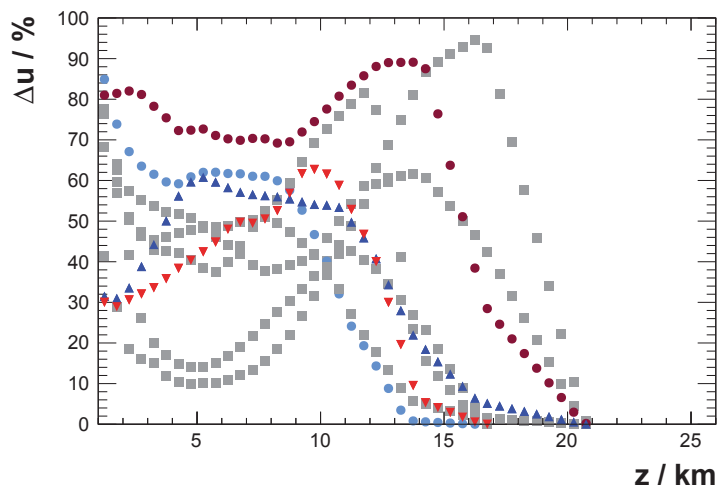
Figure 5.6: The deviation in humidity with respect to US-StdA 76 (zero humidity). Boulder and Malargüe are highlighted, as well as Alëutian and Andaman island.
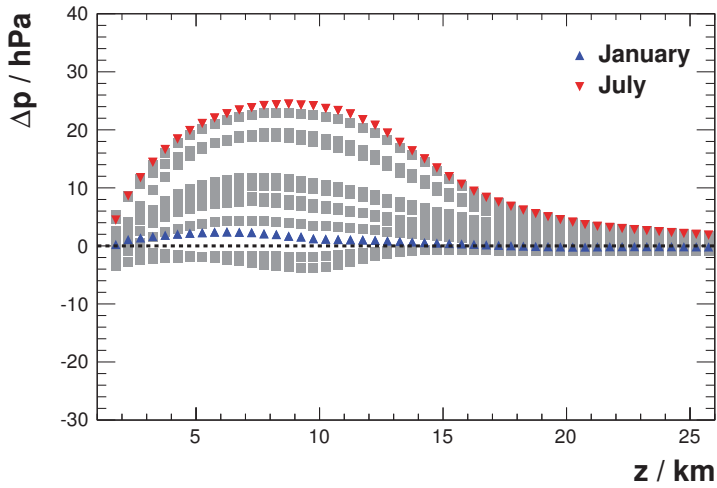
Figure 5.7: The deviation in pressure with respect to US-StdA 76. January and July are highlighted. GDAS data for Boulder (Colorado, USA), 2012.
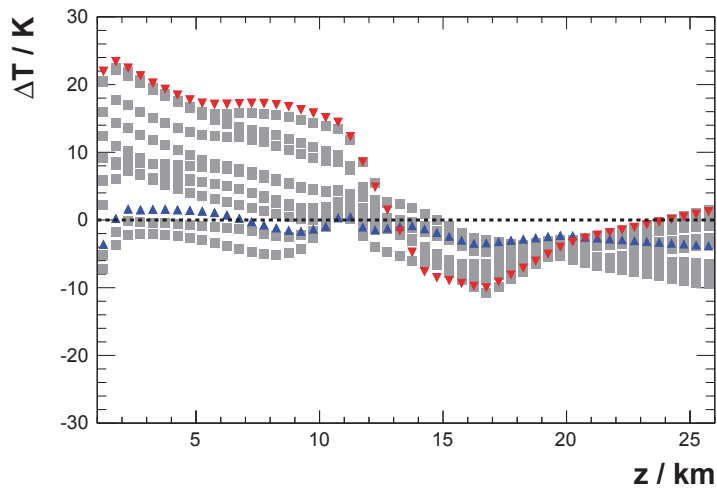
Figure 5.8: The deviation in temperature with respect to US-StdA 76. January and July are highlighted. GDAS data, Boulder (Colorado, USA), 2012.
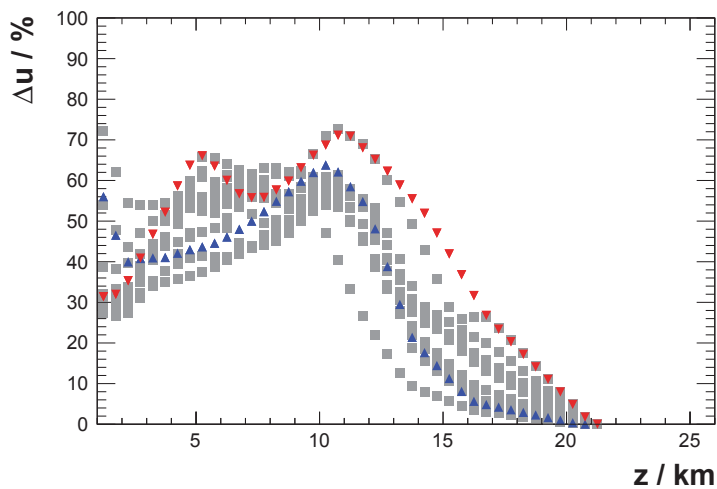
Figure 5.9: The deviation in humidity with respect to US-StdA 76. January and July are highlighted. GDAS data, Boulder (Colorado, USA), 2012.
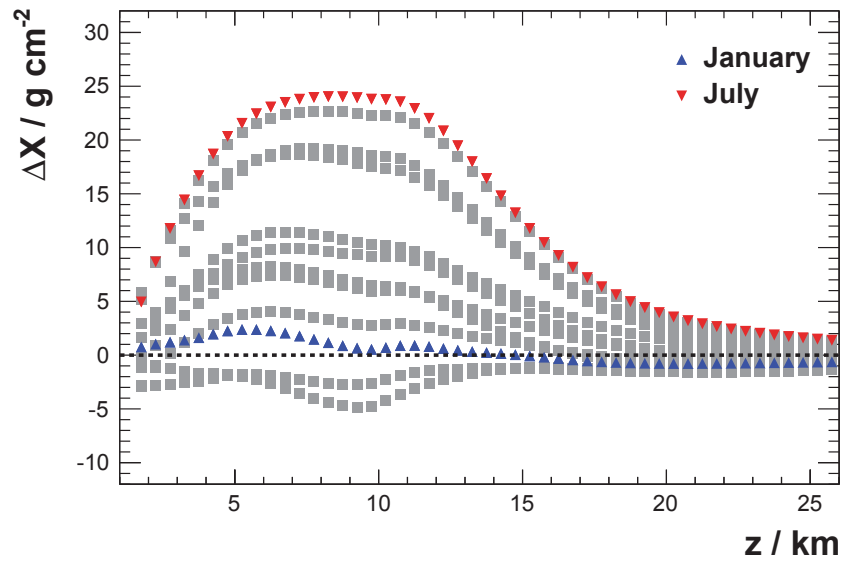
Figure 5.10: The deviation in vertical atmospheric depth with respect to US-StdA 76. January and July are highlighted. GDAS data, Boulder (Colorado, USA), 2012.

2/3 are negative at large distances. Almost all are positive close towards ground level.

The general asymmetry in Fig. 5.14 is due to the known asymmetry of the longitudinal profile of air showers which is steeper after the shower maximum. As shown e.g., in Fig. 5.4, the difference of the pressure and density of the atmosphere from US-StdA 76 is altitude dependent. Since fluorescence and Cherenkov light yields are proportional to the density/pressure of the atmosphere, the light emission will mimic these profiles dependent on the details of the mechanism.

A zenith angle dependence of the relative amount of emitted light has been seen below a zenith angle of 40°. This is due to the different atmospheric depth at which the shower encounters the ground at the simulated altitude.

(a) Spring

(b) Summer

(c) Fall
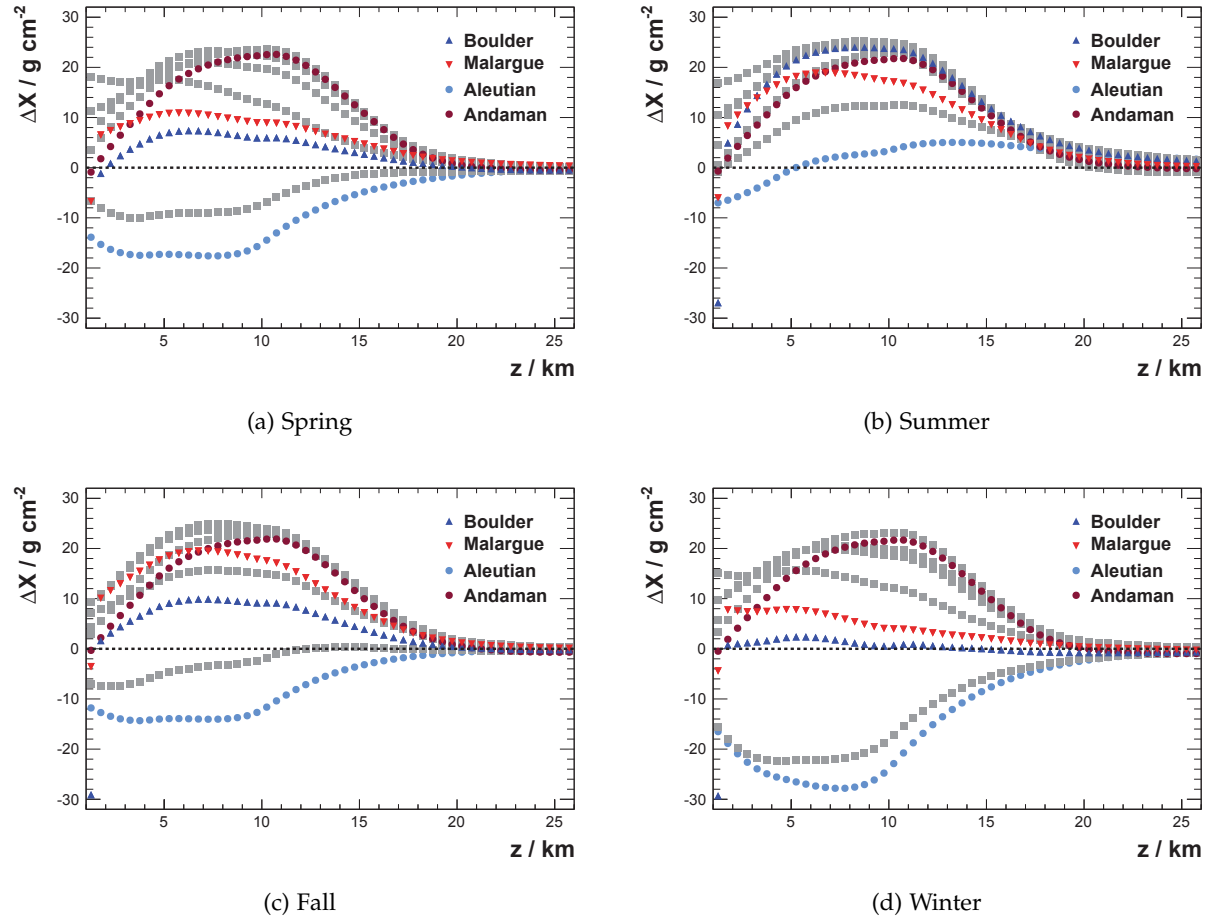
(d) Winter

Figure 5.11: Deviation of vertical depth profiles, grouped according to season. Spring covers April/October. Summer covers July/January, Fall covers October/April, and Winter January/July.
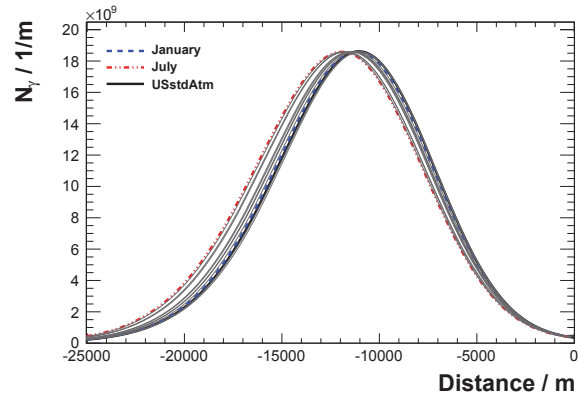
(a) Boulder
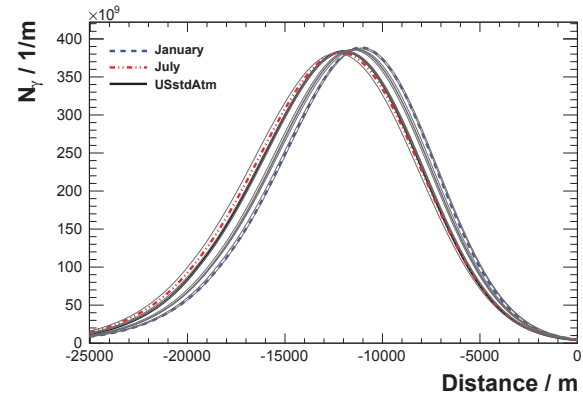
(b) Alëutian islands
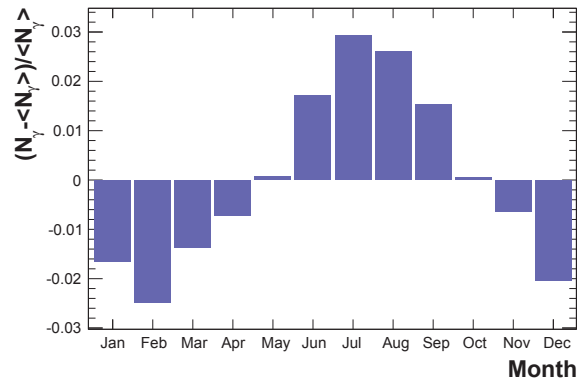
(c) Boulder
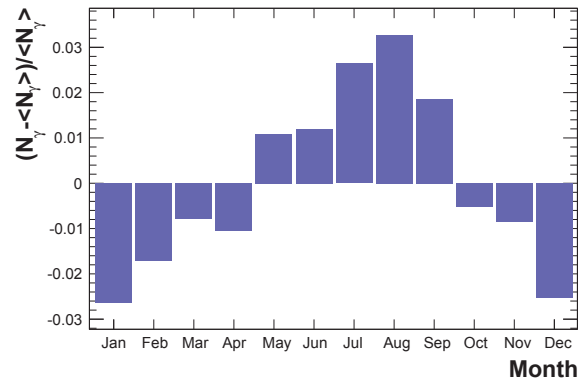
(d) Alëutian islands

Figure 5.12: Emission of fluorescence photons per m ($E = 10^{20}$ eV, $\theta = 60°$) in the range 25 km distance to shower core. (a), (b) As function of distance to shower core at sea-level. The reference amount using US-StdA 76 is displayed as the dashed line. A shift with respect to the US-StdA 76 is visible. (c), (d) Total amount as deviation from average of the total shower profile range.
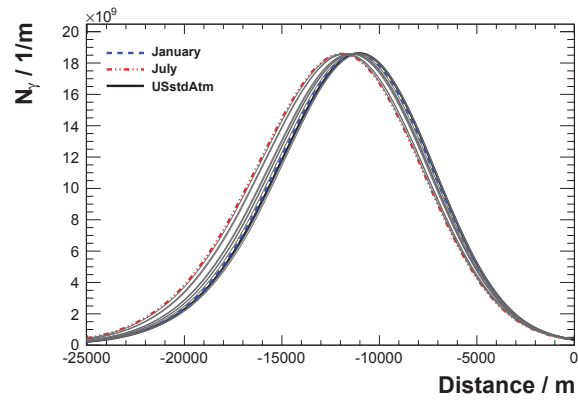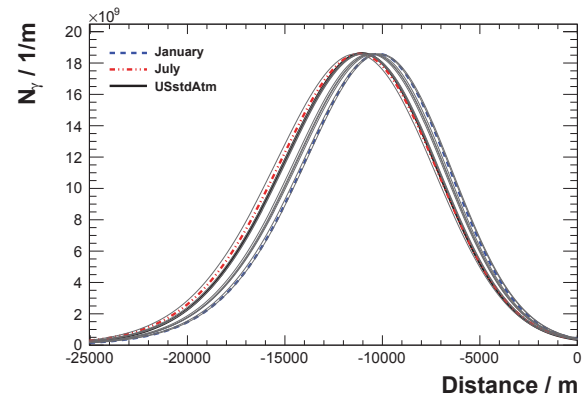
(a) Boulder

(b) Alëutian islands
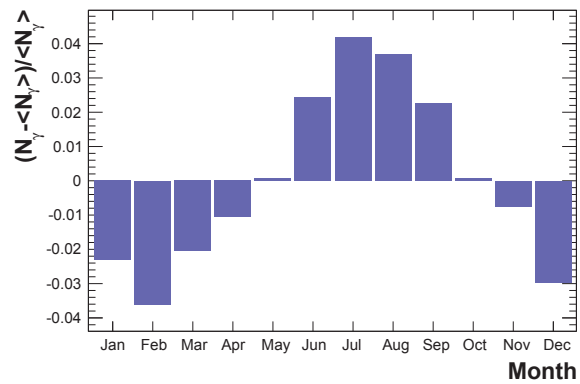
(c) Boulder
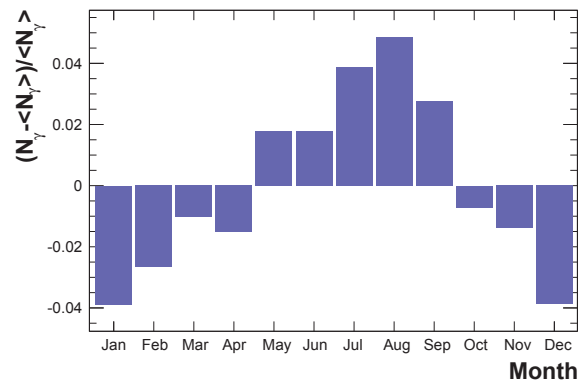
(d) Alëutian islands

Figure 5.13: Emission of Cherenkov photons per m ($E = 10^{20}$ eV, $\theta = 60°$) in the range 25 km distance to shower core. (a), (b) As function of distance to shower core at sea-level. The reference amount using US-StdA 76 is displayed as the dashed line. A shift with respect to the US-StdA 76 is visible. (c), (d) Total amount as deviation from average of the total shower profile range.
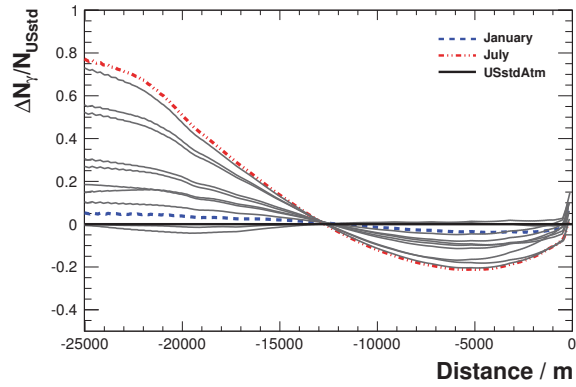
(a) Boulder, fluorescence
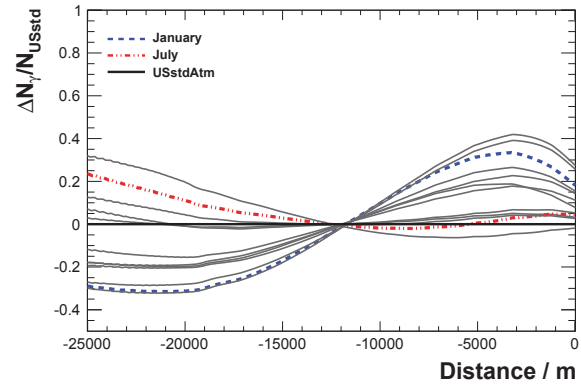
(b) Alëutian islands, fluorescence
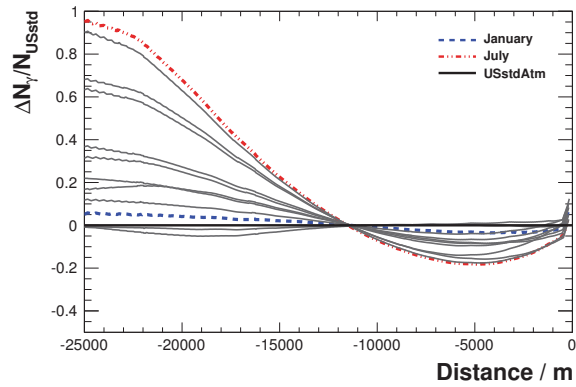
(c) Boulder, Cherenkov
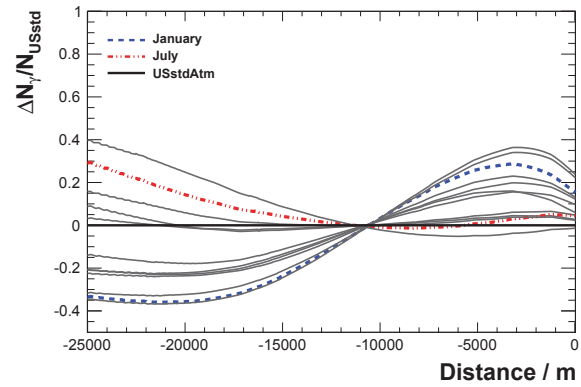
(d) Alëutian islands, Cherenkov

Figure 5.14: Relative difference of the shifted light profiles with respect to the US-StdA 76 in the range 25 km distance to shower core. January and July are highlighted blue and red.

5.3 Local Diversity of Atmospheric State

A remarkable aspect of JEM-EUSO is its wide FOV. The ground projection area has a radius of about 250 km. The atmospheric conditions will differ within this range. Moreover, a main subject of JEM-EUSO are very inclined showers with zenith angles exceeding $50°$. Showers of this type cover about $35 - 100$ km distance over ground. Since atmospheric data are provided with respect to the geographical grid, the impact of such local diversity of the atmosphere on later shower reconstruction, shall be studied in this section.

Depending on the geodetic coordinates and incoming direction, an EAS can breach several grid points. Examples of photon emission profiles for air showers with $E = 10^{20}$ eV as a function of distance to the shower core on ground level are displayed in Fig. 5.15a. The first interaction of the primary particle marks the beginning of the particle cascade, and the end by the shower core at ground level. The maximum distance from start to its end in this definition amounts to $40 - 250$ km depending on the zenith angle. For a fluorescence telescope, the amount of light transmitted is an important measure. At a rough estimate, about 500 of $270 \cdot 10^9$ photons emitted at the shower maximum reach the telescope (cf., Fig. 4.9b and Fig. 5.15a). For a single photon to be detected[14] (see Fig. 2.5), neglecting the photon background of roughly 500 photons $m^2 sr^{-1}$ ns^{-1} [83], $10 \cdot 10^9$ m^{-1} have to be emitted. The corresponding distances in Fig. 5.15a amount to $35 - 130$ km. In the ideal case, it will be possible for JEM-EUSO to observe air showers over their whole extent.

The length of a shower profile, incoming from east with respect to degree longitude, is evaluated at three different latitudes (equator, mid-latitude, and high-latitude), corresponding to San Cristóbal, Malargüe, and the Alëutian islands (Tab. 5.2). In Fig. 5.15b, the open symbols depict the length of the shower only, the solid symbols cover the whole distance to the shower core at ground level. The length of the air shower profiles ranges from $0.27°$ close the equator at a zenith angle of $60°$ to $1.89°$ at the Alëutian islands and a zenith angle of $85°$. An example shower above the Alëutian islands could cover about $4°$ in longitude from its start to the shower core at ground level.

Table 5.2: Longitudinal length of air shower profiles for different zenith angles and different latitudes. The numbers in parentheses refer to the distance covered from start of the shower profile to the ground level.

Location	θ			
	$60°$	$70°$	$80°$	$85°$
San Cristóbal	$0.27(0.31)°$	$0.38(0.51)°$	$0.73(1.20)°$	$1.17(2.24)°$
Malargüe	$0.33(0.38)°$	$0.46(0.62)°$	$0.89(1.46)°$	$1.42(2.74)°$
Alëutian isl.	$0.44(0.51)°$	$0.62(0.82)°$	$1.19(1.94)°$	$1.89(3.63)°$

From the locations listed in Section 5.2, four have been selected as center to a $5° \times 5°$-grid (Fig. 5.16). A positive $\Delta\Theta$ points northwards, and a positive $\Delta\Phi$

---

[14]Detection efficiency $\propto 20\%$
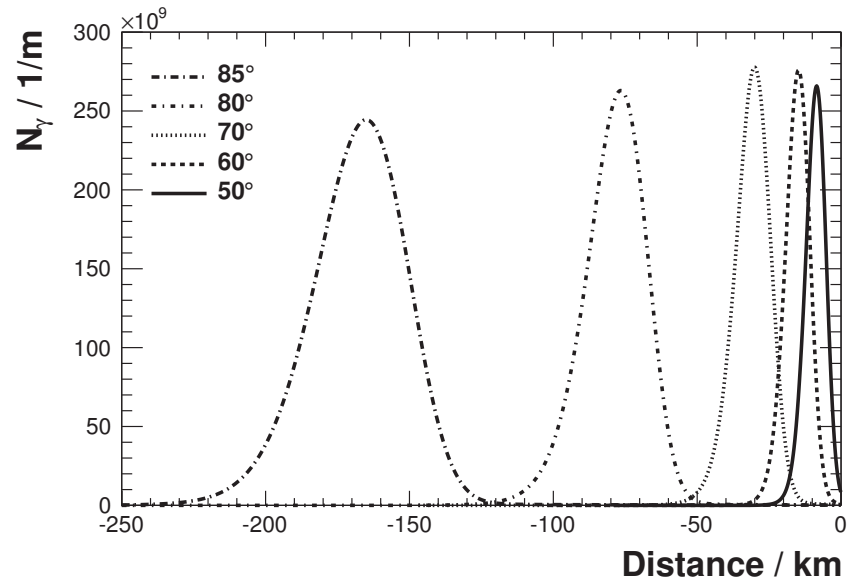
(a)
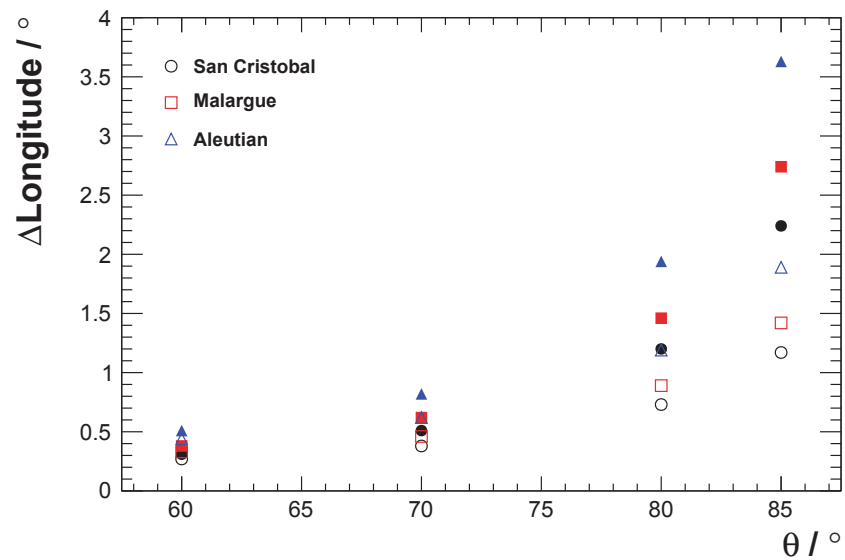
(b)

Figure 5.15: Length of shower profiles for different zenith angles ($60° \geq \theta \geq 85°$, $E = 10^{20}$ eV) (simulated with Conex). (a) Extent as a function of distance to the shower core on ground level. (b) Extent as a function of zenith angle θ for different latitudes. The open symbols depict the length of the shower only, the solid symbols cover the whole distance to the shower core at ground level.
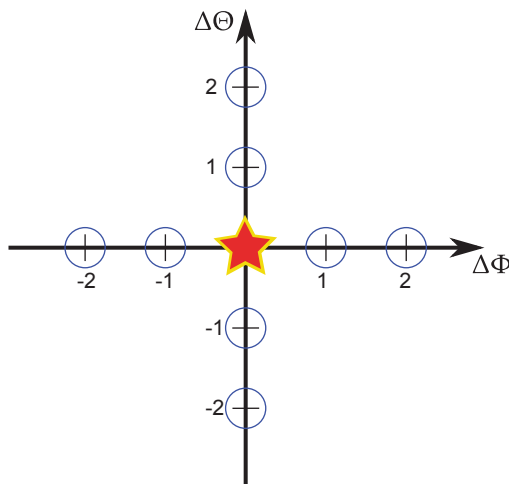
Figure 5.16: Definition of the grid used for the comparison of different atmospheric profiles. The base is marked by the star. The geodetic coordinates of the base are (Φ, Θ). A positive $\Delta\Phi$ points to a location further east, a positive $\Delta\Theta$ further north.

eastwards. For each, two months are chosen to represent seasonal extremes. The profiles have been truncated with respect to the highest surface level among the grid points. The variation of atmospheric parameters with respect to the central location are presented as a function of pressure in Figs. 5.17-5.18, as well as in the Appendix (Figs. B.33-B.34).

For *Malargüe*, two prominent months are May and November, January and July for the remaining. "Latitude" refers to grid points east and west from the central location, while "Longitude" refers to points north and south. The north-south variation for center *Malargüe* is depicted in Fig. 5.17 (a),(b). The temperature varies within ± 2 K. The course is symmetric with respect to the horizontal axis. The location further north starts warmer in the stratosphere and turns colder in the troposphere with a turning point in the tropopause. The location further south starts colder and turns warmer in the troposphere. Also the variation of height is symmetric with respect to the horizontal axis. It reaches its maximum at the tropopause ($15 - 20$ km $\Rightarrow 120 - 50$ hPa). Since pressure is a exponential function of height (Eq. (3.7)), a positive deviation in height means higher pressure. The relative humidity varies within $\pm 10\%$. The east-west variation is depicted in Fig. 5.17 (c),(d). The variation profiles are quite asymmetric. The largest variation in temperature appears in the lower troposphere (up to 6 K). The humidity at ground level is lower compared to the central location.
The north-south variation for center *Pico* behaves similar as for Malargüe (see Fig. 5.18 (a),(b)), with the largest deviations in January. The east-west variation Fig. 5.18 (c),(d) is not significant.
Data of the *Alëutian islands* (Fig. B.33) and *Antofagasta* (Fig. B.34) display the same trends more or less pronounced.

The vertical atmospheric depth has been calculated for the prominent months. The variation with respect to the central location Malargüe/Azores is displayed as profile histograms in Figs. 5.19-5.20, the remaining locations it is displayed in Appendix Figs. B.35-B.36. The colored bands represent the monthly variation by display of the standard deviation on the mean in each bin. They follow the variation of pressure, as expected. The largest deviation compared to the central location Malargüe is of the order of ± 2 g cm^{-2} at about 10 km height and

becomes smaller towards ground. The variation with respect to the center at Pico is of the same order (± 2.8 g cm^{-2}), except for the east-west deviation which is insignificant. The same holds for the Alëutian islands and Antofagasta.

The atmospheric depth at ground level has been computed for the Azores (January 2009), and Malargüe (November 2009) with respect to the zenith angle using the `InclinedAtmosphericProfile` in Off$\overline{\text{line}}$. The profile inclination reaches from $0 - 80°$ in zenith angle, and is computed in steps of $5°$ (see Fig. 5.21). In case of Malargüe, the ground level had to be raised to about 3 km because of the Andes to the west. The deviations for Malargüe are small and asymmetric (cf., Fig. 5.19d, Fig. 5.21a). Except for one location, all vertical depth profiles deviate negatively. The largest deviation is found for the location $1°$ east of Malargüe. Starting at $\Delta X = -0.6$ g cm^{-2} in vertical depth, the deviation is amplified to -3 g cm^{-2} at $80°$. For the Azores (Fig. 5.21b), the deviations display a reciprocal trend, symmetric with respect to zero, and an asymptote at about $90°$. The small vertical difference in depth (less than ± 5 g cm^{-2}) becomes ± 15 g cm^{-2} for EAS with $\theta = 80°$. The overall asymptotic behavior originates from the integration in a ellipsoidal atmosphere.
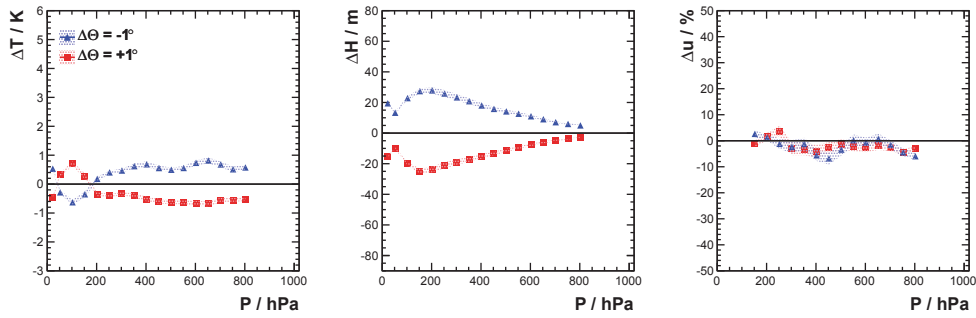
(a) Latitude, May 2009
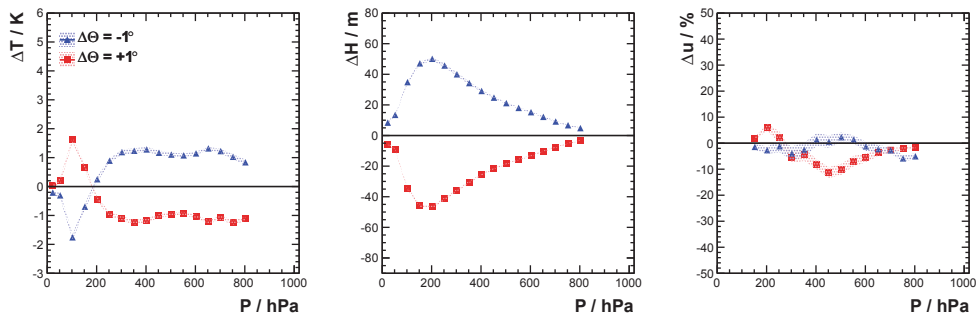
(b) Latitude, November 2009
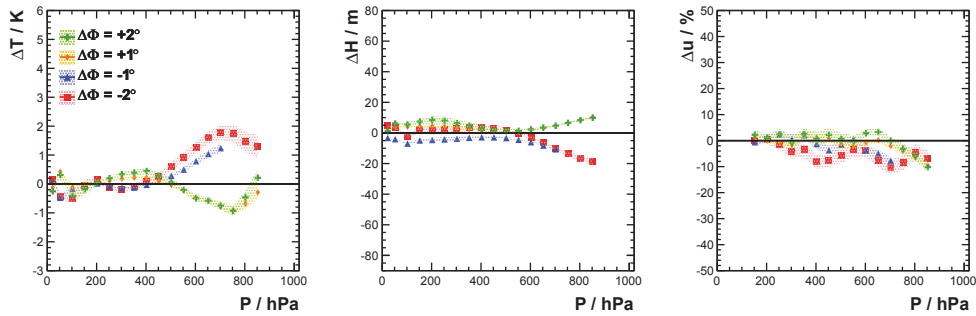
(c) Longitude, May 2009
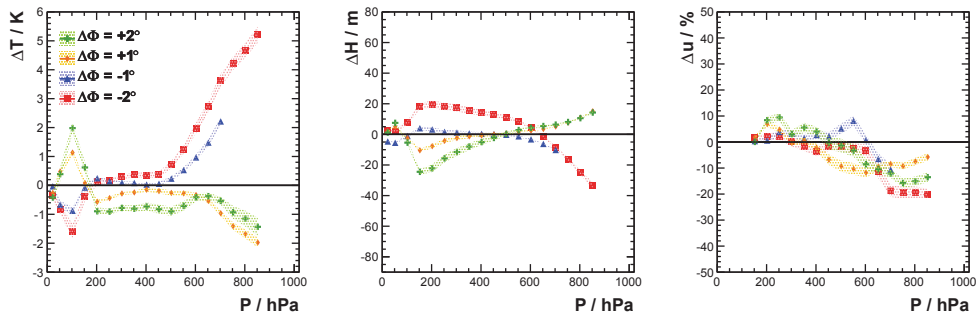
(d) Longitude, November 2009

Figure 5.17: Deviation of atmospheric profiles (T, h, u) at surrounding GDAS grid locations as a function of pressure. Malargüe (Argentina). The colored bands represent the standard deviation on the mean in each bin.
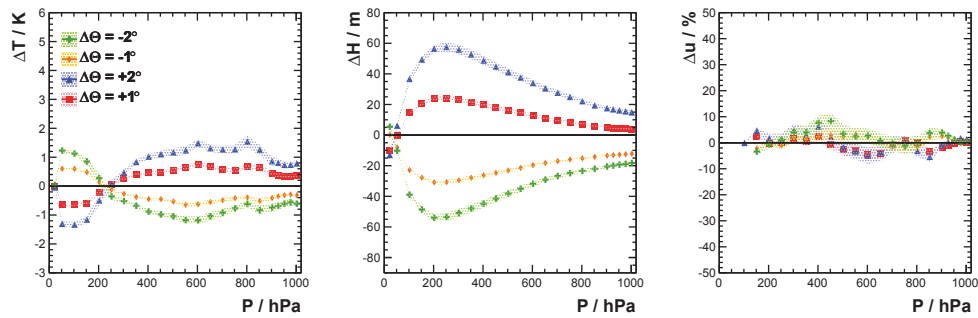
(a) Latitude, January 2009
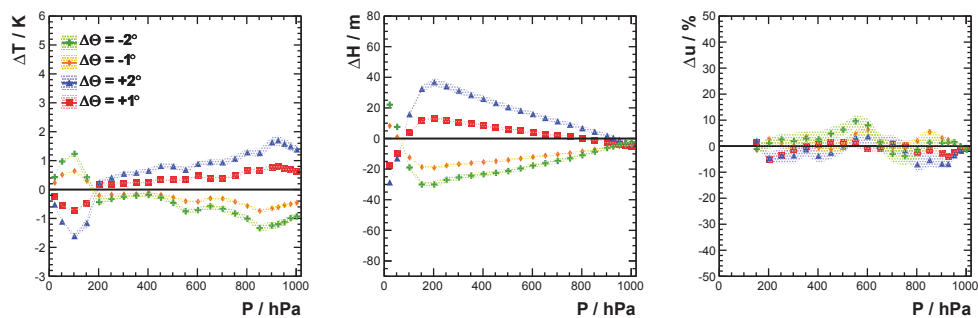
(b) Latitude, July 2009
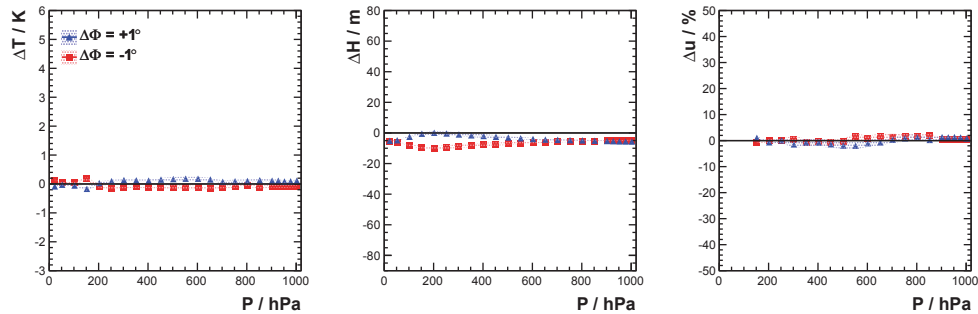
(c) Longitude, January 2009
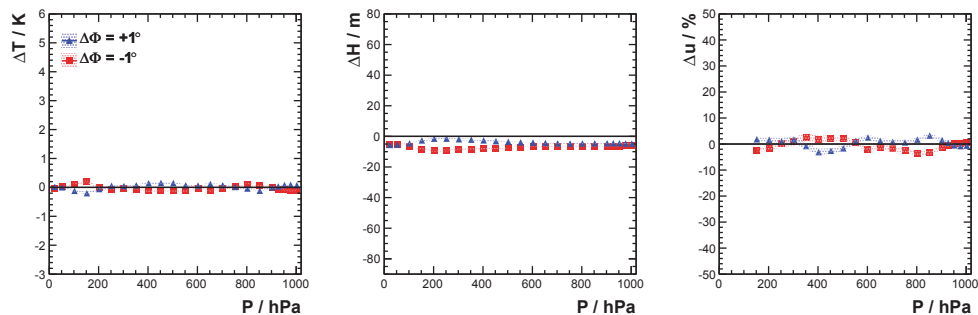
(d) Longitude, July 2009

Figure 5.18: Deviation of atmospheric profiles (T, h, u) at surrounding GDAS grid locations as a function of pressure. Pico (Azores). The colored bands represent the standard deviation on the mean in each bin.
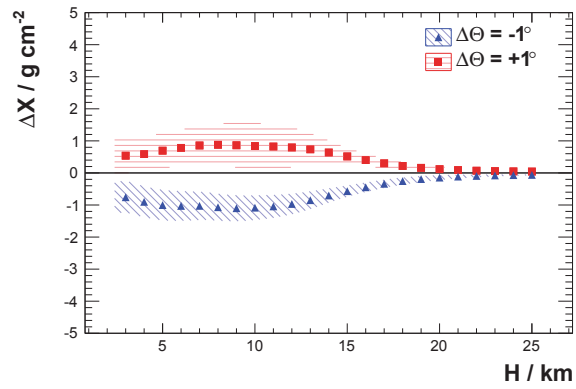
(a) Latitude, May 2009
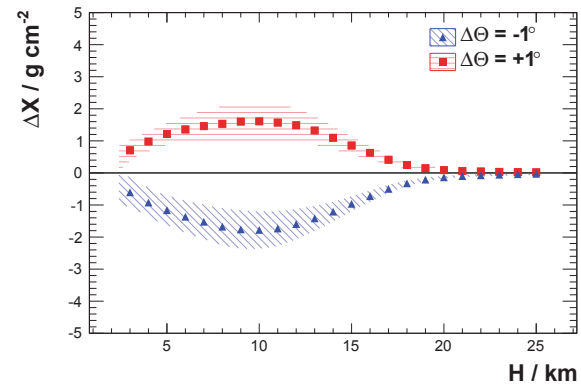
(b) Latitude, November 2009
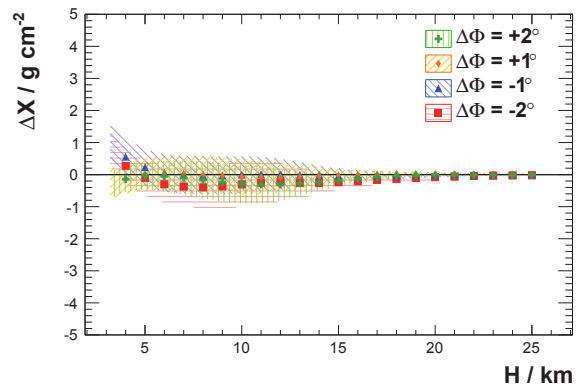
(c) Longitude, May 2009
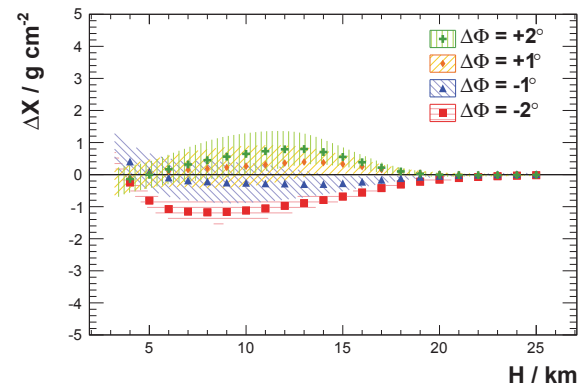
(d) Longitude, November 2009

Figure 5.19: Deviation of atmospheric depth profiles at surrounding GDAS grid locations as a function of height. Malargüe (Argentina). The colored bands represent the standard deviation on the mean in each bin.
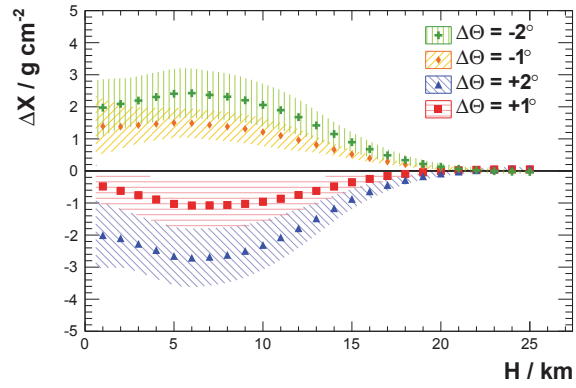
(a) Latitude, January 2009
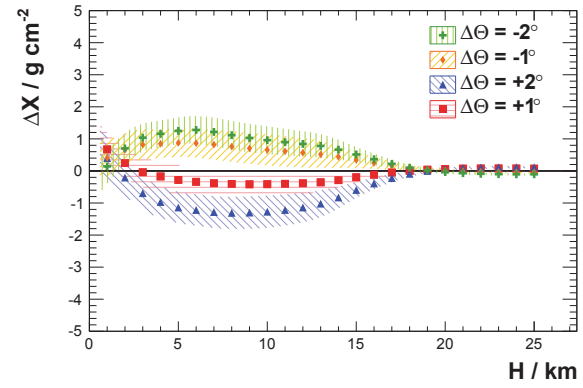
(b) Latitude, July 2009
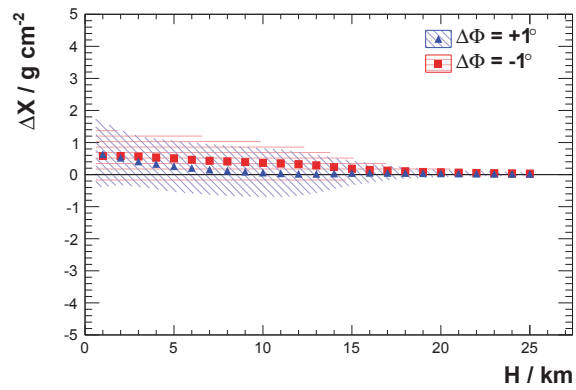
(c) Longitude, January 2009
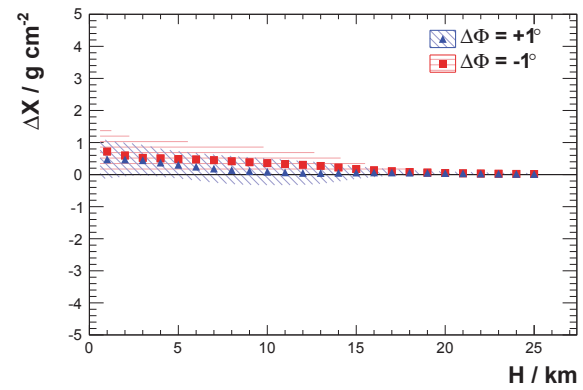
(d) Longitude, July 2009

Figure 5.20: Deviation of atmospheric depth profiles at surrounding GDAS grid locations as a function of height. Pico (Azores). The colored bands represent the standard deviation on the mean in each bin.
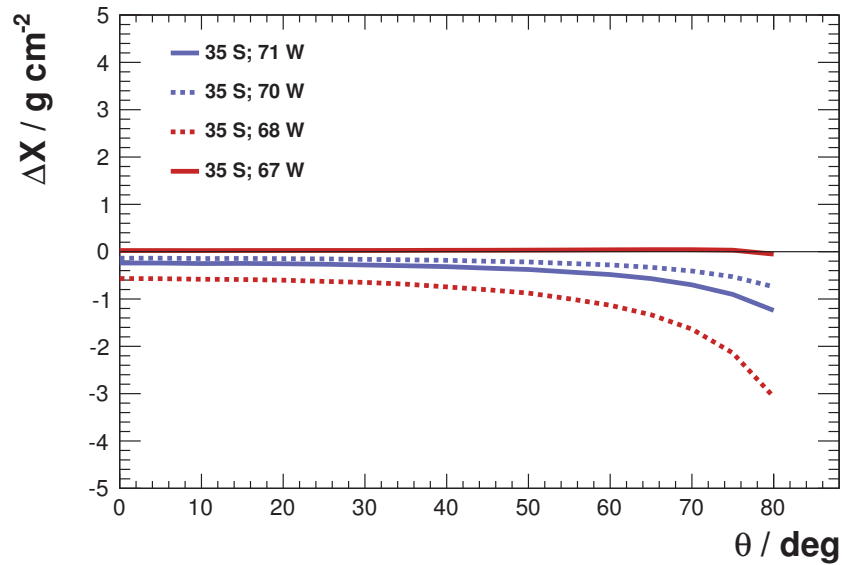
(a)
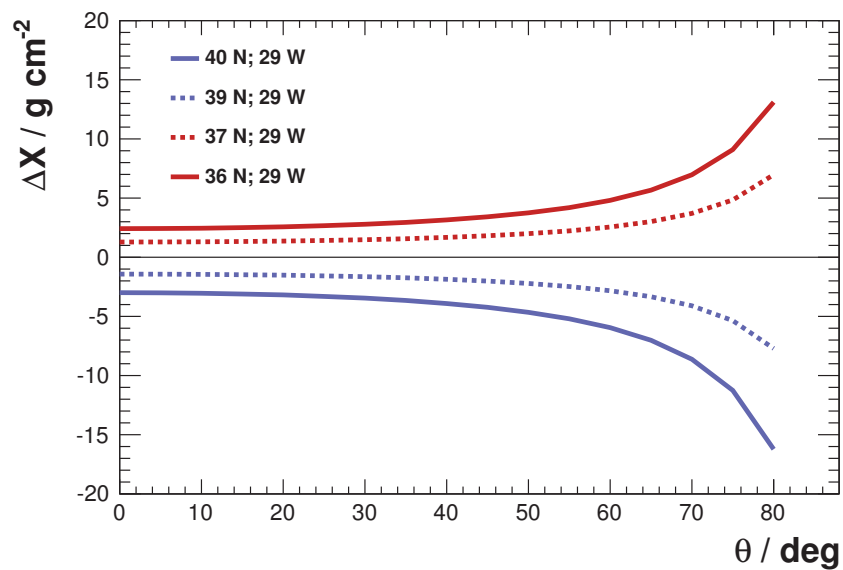
(b)

Figure 5.21: Deviation of atmospheric depth at ground level for every grid-point as a function of zenith angle θ. (a) Malargüe, November 2009. The ground altitude is 3 km because of the Andes to the west. (b) Azores, January 2009. The ground altitude is set to sea level.

5.4 Summary & Conclusion

There are deviations as large as $30\,\mathrm{g\,cm^{-2}}$ found in atmospheric depth profiles. It will be necessary to use the correct atmospheric profile considering the X_{max}-reconstruction. US-StdA 76-reconstructed events will display a bias towards deeper X_{max}, if the place of observation is close to the equator. In contrary, if the shower is observed far from the equator the bias would point to the opposite direction. These uncertainties are of slightly smaller as the reconstruction results of JEM-EUSO for X_{max}, which are expected to be roughly $100\,\mathrm{g\,cm^{-2}}$.

Applying these profiles to simulation of light production by EAS, the utmost difference of the shower maximum for a $E = 10^{20}$ eV, $\theta = 60°$ shower amounts to $1\,300$ m distance along the incidence direction of the shower. Taking the resolution of JEM-EUSO into account, which is ≈ 500 m close to ground level, the differences might be resolvable. However, the deviation in emitted fluorescence photons, amounting to about $\pm(5-6)\%$, will influence the energy reconstruction as well. The latest results on the energy reconstruction by the JEM-EUSO collaboration $E_{\mathrm{reco}}/E_{\mathrm{real}}$ display a $\approx 10-15\%$ reconstruction bias, while the precision is $\pm 20\%$ at best, taking the atmosphere not into account [31]. Since Cherenkov light is not directly observed, no conclusion can be drawn at this point. For quick reconstructions the US-StdA 76 is sufficient, but an actual atmospheric profile at the time and place of the EAS event is necessary for an elaborate analysis. This can be achieved by inclusion of GDAS data into the reconstruction of individual events.

Taking the spatial resolution of JEM-EUSO into account, small variations in the atmospheric conditions of different locations within the FOV have no significant influence on the reconstruction of the depth. Even the largest deviation is within the general experimental uncertainties. A conservative approach for reconstruction would be using an atmospheric profile at the nadir position on ground. In extreme cases, e.g., a shower at the edge of the field of view, it can be necessary to evaluate several atmospheric conditions.

Radiative Transfer in view of JEM-EUSO

In this chapter, details on the results of the radiative transfer simulation for JEM-EUSO will be given. Radiative transfer is addressed in two ways, the attenuation of light during propagation from its source to the detector via scattering and absorption and scattering of source light towards the detector. The former reduces the light flux, while the latter increases the number of detected photons. For the energy reconstruction, a proper estimation on attenuation and scattering is needed. First, the attenuation due to Mie and Rayleigh scattering for a space-borne experiment will be presented in comparison with the known case of a ground-based observatory. Multiple scattering will not be addressed in this chapter. The influence of ozone absorption in the UV band of interest has been studied in detail for three selected NOAA ozone sounding stations. Finally, the combined impact of the atmospheric conditions and albedo on emission and transmission will be presented as comparison between all example locations.

6.1 Atmospheric Scattering

Mie and Rayleigh attenuation play a significant role for Earth-based fluorescence detectors. To fathom the importance for a space-based observatory, the transmission factors T has been calculated for Rayleigh and Mie scattering (see Fig. 6.1). Taken from measurements of the Pierre Auger Observatory, the Mie attenuation length is 52.645 km in a homogeneous mixing layer below 3 km. This shall represent a very clear atmosphere. The ratio between the height of the mixing layer and the attenuation length is $\tau \approx 0.027$. The Rayleigh attenuation length is computed using the US-StdA 76. A fictive light source was placed on a plane at an altitude of 1400 m (e.g., Pampa Amarilla), the detector at the ISS altitude of 400 km above ground, as well as in a distance of 40 km on ground level. In case of a detector at the ISS altitude (Fig. 6.1a), the attenuation by Rayleigh scattering dominates, especially at lower wavelengths. At 280 nm, the transmission only amounts to about 20% increasing to about 80% at 450 nm. Mie attenuation affects the transmission less than 10%. For a smaller Mie attenuation length ($\tau \approx 0.25$), the Mie transmission factor drops to $50 - 60\%$. For a detector at ground level (Fig. 6.1b), the atmosphere is quite opaque for light of wavelengths below 340 nm ($T \leq 2\%$). The Rayleigh attenuation is still dominant, but the Mie attenuation ($\tau \approx 0.027$) contributes much stronger ($40\% \leq T \leq 54\%$). The total transmission only reaches 20% at 450 nm. Aerosols, except for clouds and fog, are not directly related to the state of the atmosphere. As shown above, Mie attenuation does not play a major
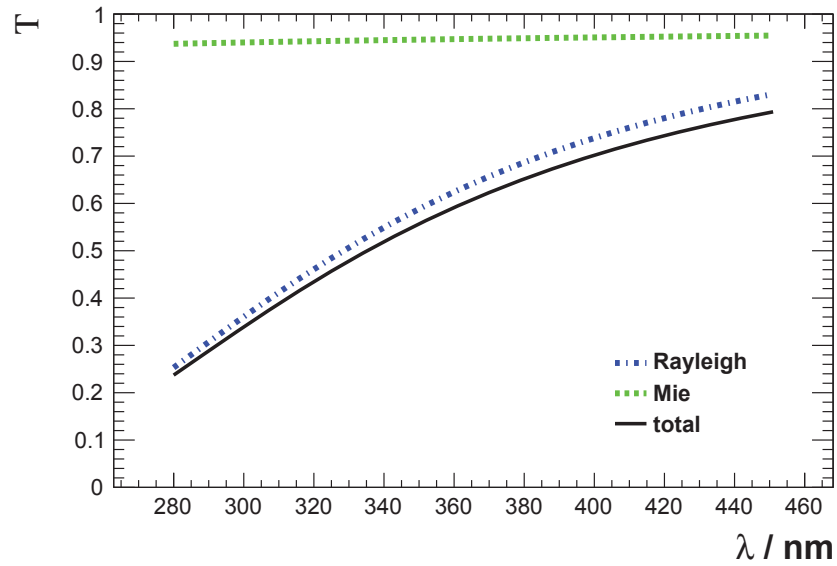
(a)
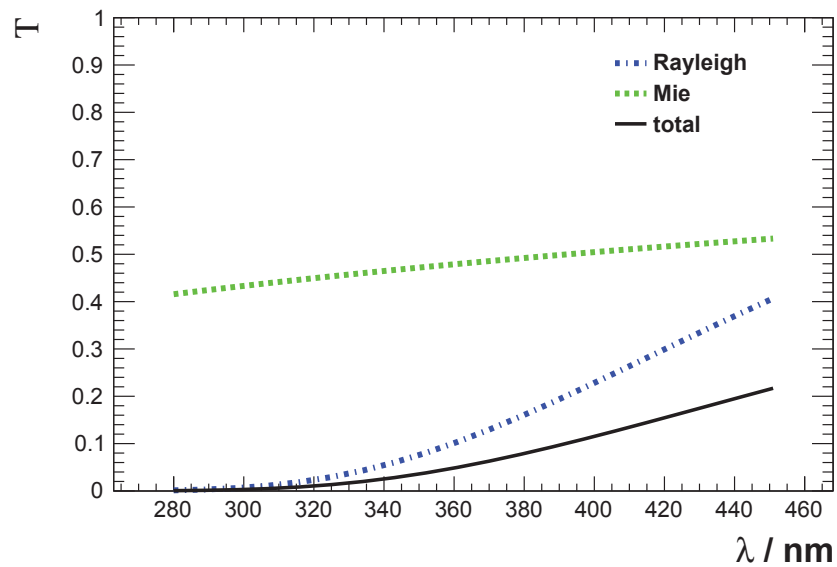
(b)

Figure 6.1: Comparison of the transmission factor *T* for Mie and Rayleigh scattering. The Mie attenuation length is 52.645 km in a homogeneous mixing layer below 3 km, taken from measurements of the Pierre Auger Observatory. The Rayleigh attenuation length is computed with respect to the US-StdA 76. The detector was placed (a) at the ISS altitude 400 km above ground, (b) in 40 km distance at ground level.
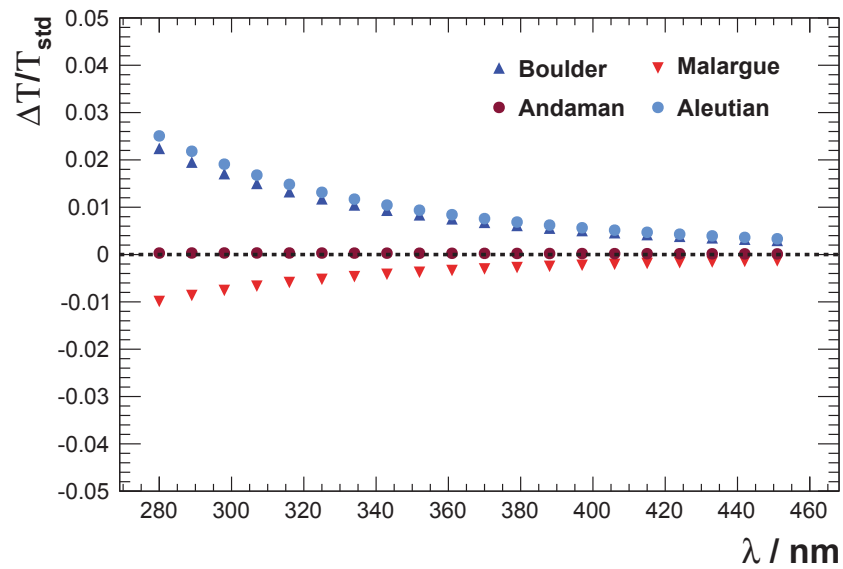
(a)
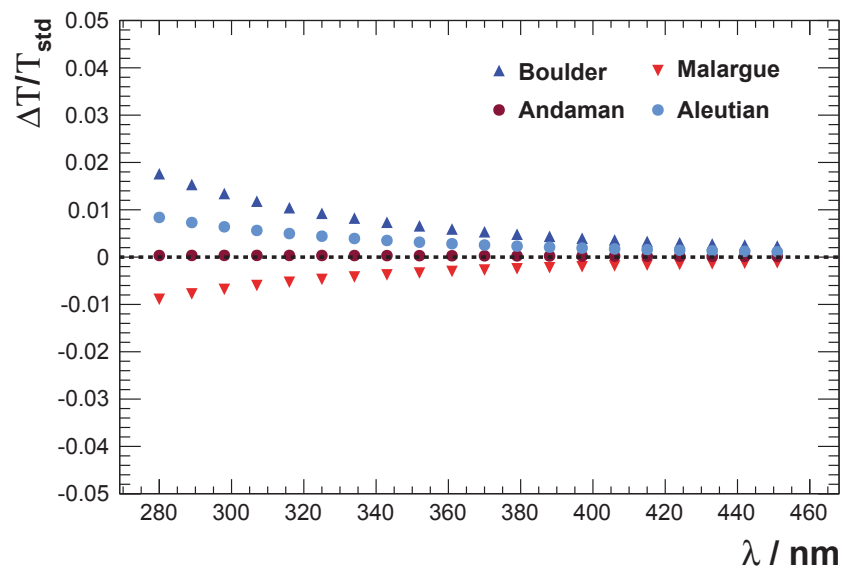
(b)

Figure 6.2: Rayleigh attenuation as function of wavelength λ. The deviation to US-StdA 76 divided by US-StdA 76. (a) Winter atmospheric profiles. (b) Summer atmospheric profiles.
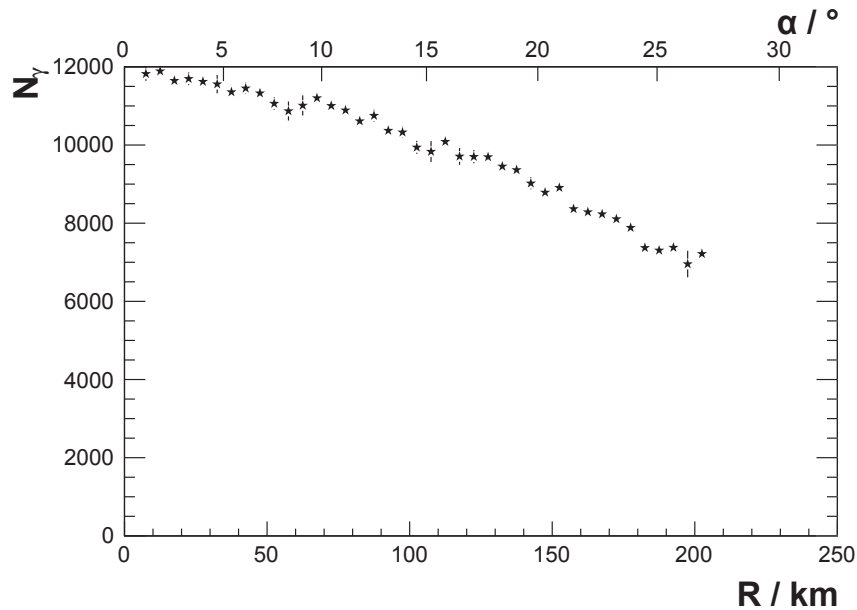
Figure 6.3: Dependence of the light transmission in the distance R from nadir position of shower core. 500 showers from Conex simulation ($E = 10^{20}$ eV, $\theta = 60°$) have been processed with the $\overline{\text{Off}}\underline{\text{line}}$. On top the corresponding off-axis angle α is shown. The shower core on ground has been placed randomly. No ozone attenuation has been applied.

role in case of clear atmospheric conditions, hence it shall not be further studied here. The Rayleigh attenuation for different atmospheric profiles is displayed in Fig. 6.2. Only Malargüe displays a higher attenuation compared to US-StdA 76 in winter, as well as in summer ($\Delta T/T \approx -1\%$ at 280 nm). The Boulder data display $\sim (2 \pm 0.2)\%$ less attenuation. The deviation from US-StdA 76 decreases with wavelength. A seasonal change of transmission is only significant for the Alëutian islands (winter $\sim 2.6\%$, summer 1% more transmission). The Andaman islands reproduce the US-StdA 76 Rayleigh attenuation well.

Since JEM-EUSO will have a wide FOV, the further from the center of the FOV a shower, the fainter it will appear due to the larger amount of atmosphere the light has to pass. To quantify this effect, 500 showers simulated with Conex ($E = 10^{20}$ eV, $\theta = 60°$) have been processed with the $\overline{\text{Off}}\underline{\text{line}}$[15] at varying core positions, randomly selected at a distance R relative to the nadir center of the FOV on ground. The maximum R was about 250 km. No ozone attenuation was applied (see Section 6.2). The result is depicted in Fig. 6.3. The number of transmitted photons drops from 12 000 to $\sim 7\,000$ at a distance of 225 km from the nadir position ($\sim 40\%$). This result, however, does not take possible inefficiencies of the optical system at the edges of the FOV into account. The decrease in the amount photons at the aperture is comparable with 40.3% (Section 2.2 cf., Fig. 2.6). The total number of photons differs, probably due to a different assumed size of the aperture.

---

[15]Version February 2014, Simulation chain according to Section 4.1

6.2 Ozone Absorption

For a ground-based observatory, and fluorescence light emission in a height of about 20 km, a previous study had shown that the influence of ozone absorption is negligible [50]. In the following section, the extraction of ozone profiles, and a cross check with total column ozone from literature, as well as a study on light transmission for various ozone profiles will be presented.

The GAM discussed in Section 5.1 provide total column ozone Σ_{O_3}. For calculation of the radiative transfer from EAS, the actual profile of the ozone distribution is needed. The data of ozone concentration in the atmosphere were taken from balloon soundings conducted by NOAA in the years $1993 - 2012$. The ozone sondes used by NOAA consist of a small Teflon air pump blowing ambient air onto an electrochemical ozone sensor [64]. The processed data are available in ASCII format from an open-access ftp-server at NOAA. The maximum altitude of an ascent is typically reached between 30 and 40 km, referred to as *balloon burst altitude*. Entries tabulated in the files are:

- Level ID
- Pressure (in hPa)
- Altitude (in km) (in steps of 100 m)
- Temperature (in °C)
- Relative Humidity (in %)
- Ozone Partial Pressure (in mPa, ppmv, atmcm)
- Ozone Number Density (in 10^{-11}/ cm^3)
- Ozone Density (in DU).

From nine available sounding sites, three have been chosen for this study (Boulder (Colorado, USA), Hilo (Hawaii, USA), and Pago Pago (American Samoa)). All locations are depicted in Fig. 6.4.

Overall, ozone profiles from 2042 ascents have been selected. The selection comprises 957 (664) for Boulder, 998 (638) for Hilo, and 187 (124) for Pago Pago. For comparison with satellite data [57], two data samples have been drawn. The sample referred to as "decadal" contains data from $2000 - 2012$ soundings only (given by the numbers in parenthesis above). The second sample, referred to as "annual", contains data from 1993 only which is closest to the time frame of the satellite data. Two of the sites are located in the Pacific, north and south of the equator. They have been chosen as representatives for oceanic ozone conditions, and the two hemispheres. For comparison, the one at Boulder represents continental ozone.

6.2.1 Ozone Profiles

In Fig. 6.5, all ozone profiles from ascents between 2000 and 2012 are shown as color coded two dimensional histograms for the sounding stations at Boulder and Hilo. Typical ozone profiles were described in Section 3.1.3. The actual examples shown here confirm these profiles. In both cases, the amount of ozone increases within the troposphere towards ground level. It is more pronounced for Boulder,
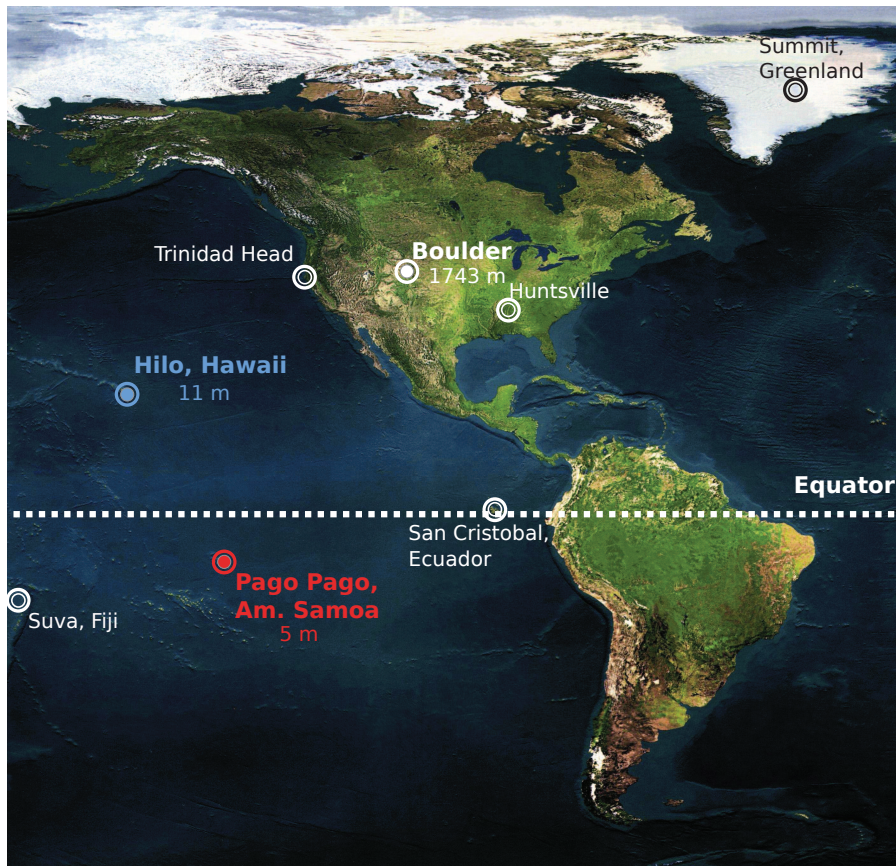
Figure 6.4: Locations from NOAA ozone soundings. Of nine available stations (Amundsen-Scott South Pole Station not shown) three have been chosen for this study: Boulder (Colorado, USA), Hilo (Hawaii, USA), Pago Pago (American Samoa).

because there is less humidity to dissolve the tropospheric ozone and more human activity in that region compared to Hilo. The variation of stratospheric ozone is lower above Hilo. Most of the variation visible in the stratosphere above the ozone peak (Fig. 6.5a) is related to the change of season. Since seasons are not as pronounced in an oceanic climate, the above applies to data from Pago Pago soundings, too. The wide spread of data throughout the tropopause may relate to temporal weather phenomena.

Details on the seasonal behavior become visible in Fig. 6.6. Less seasonal variation is found in the data sample of Hilo. The mean profiles of Boulder display a higher ozone concentration during winter and spring. Significance and influence on light transmission will be discussed later in this section.

For the simulation routines, complete ozone profiles are needed. It is necessary to extrapolate the ozone profiles beyond the balloon burst altitude. Two different extrapolation functions have been tested by means of robustness and minimum bias. Following the ozone model given by US-StdA 76, an exponential extrapolation from 35 km to about 100 km has been assumed and for comparison, a linear extrapolation has been done (Fig. 6.7), which confines ozone to a maximum height between $40 - 50$ km. For statistical reasons, only the last ten bins with more than ten entries in case of the decadal sample, and more than four entries in case of the
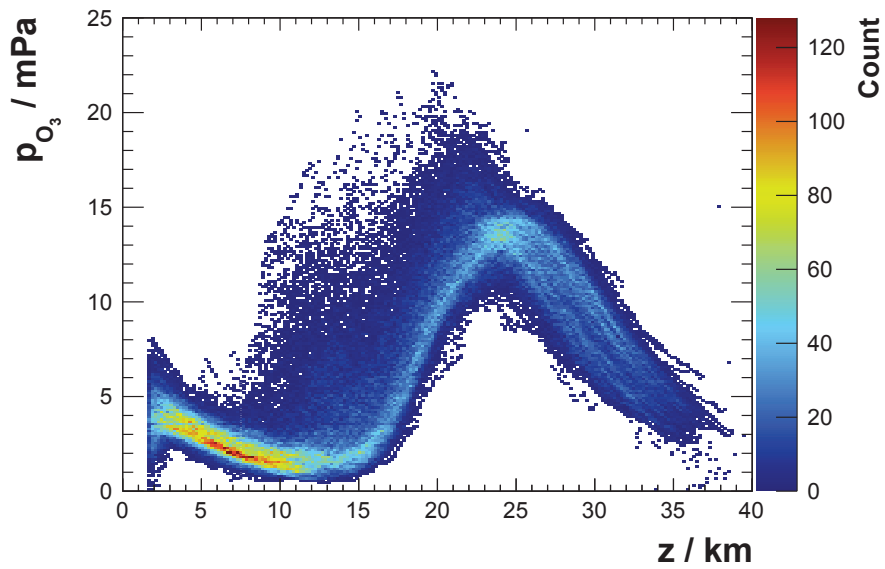
(a) Boulder
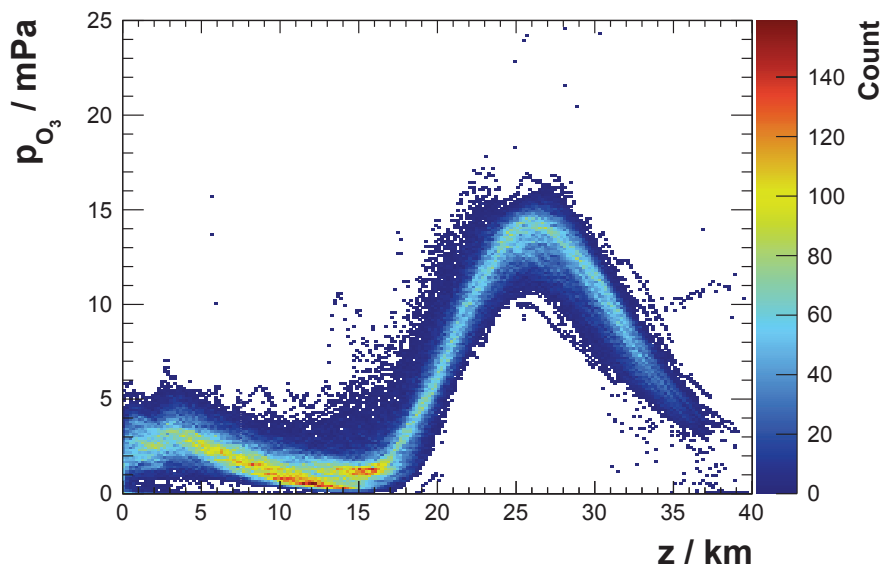
(b) Hilo

Figure 6.5: Ozone partial pressure profiles of raw data from ozone soundings $2000 - 2012$ by NOAA. The color code displays the number of counts per bin.
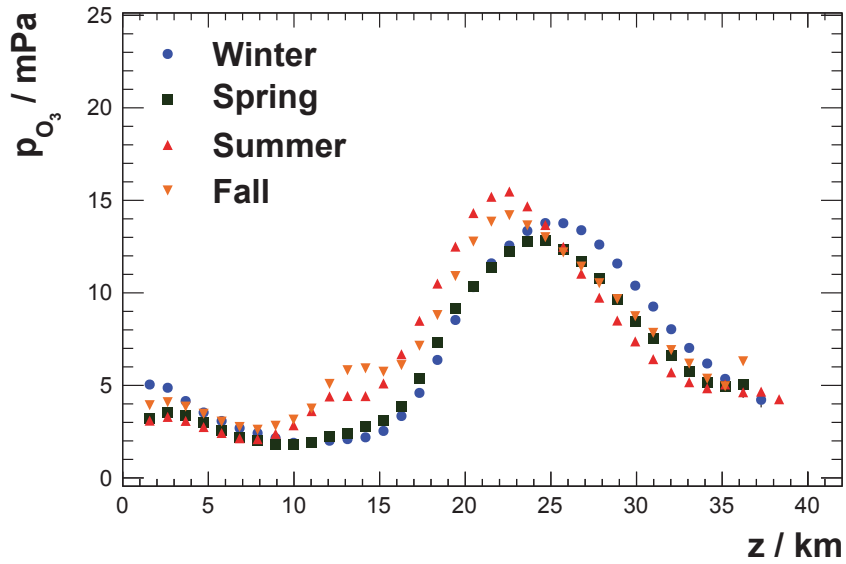
(a) Boulder
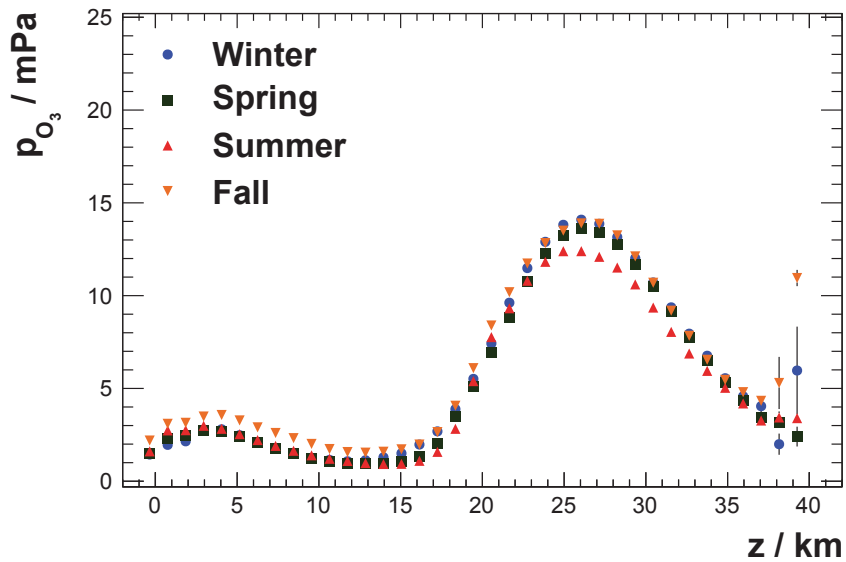
(b) Hilo

Figure 6.6: Mean profiles from ozone sounding $2000 - 2012$. Raw data have been selected by month. Mean is shown for winter (December-February), spring (March-May), summer (June-August), fall (September-November).
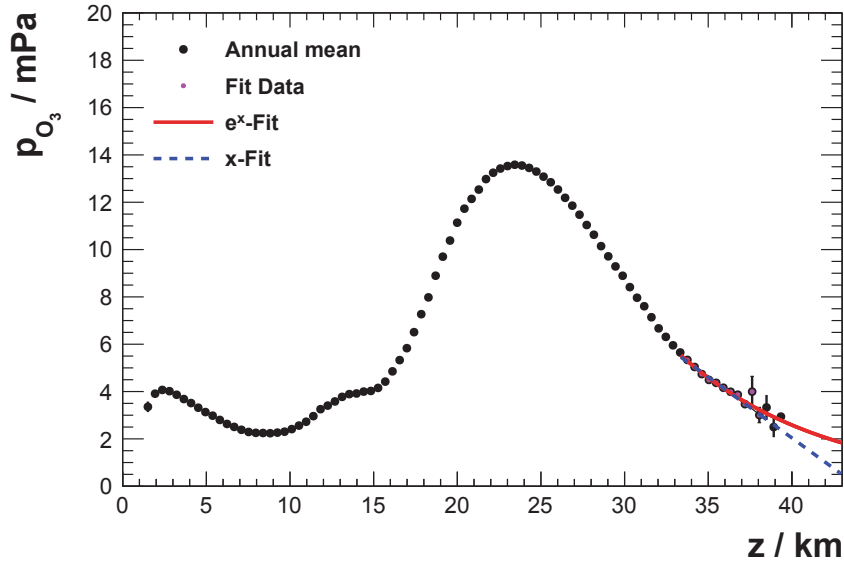
Figure 6.7: Linear and exponential fits to profile of Boulder $2000 - 2012$ ozone sounding data.

annual sample have been chosen. In addition, the Poissonian uncertainty within one bin should be less than 0.01.

The profile results are compared in terms of Σ_{O_3} to climatological ozone tables derived from measurements by the Nimbus 7 solar backscattered ultraviolet (SBUV) instrument [57]. The processed measurements of SBUV are summarized in tabular form as total ozone residuals Σ_{res} between 0 and 30 mbar and tabulated in steps of $10°$ latitude.

The two different samples drawn from sounding data at Boulder consist of twelve monthly mean values. The chosen years are 1993 (annual sample) and a span of twelve years starting in 2000 (decadal sample). For each set, $\Delta\Sigma_{O_3}$ has been computed which is the extrapolated, missing amount of ozone above the balloon burst altitude. $\Delta\Sigma_{O_3}$ is compared to the residual value from the SBUV tables $\Sigma_{res}(\Theta, p)$, evaluated at the corresponding latitude of the station and balloon burst pressure. The results are displayed in Fig. 6.8. In both sets, the exponential extrapolation overestimates the total column ozone, whereas the linear extrapolation underestimates it.

In 1993 (Fig. 6.8a), the mean deviation is 23 DU in the exponential extrapolation case, otherwise it is -15 DU. With standard deviations per month of 10 DU and 7 DU the deviation from SBUV for both extrapolations is rather small (within 2σ). The second set (Fig. 6.8b) behaves differently. The mean deviation in case of the exponential extrapolation reaches 40 DU, whereas for the linear extrapolation it is -8 DU. The standard deviations are 12 DU and 6 DU. Both are shifted to higher Σ_{O_3} by about 1σ. It is possible that this effect is due to changes in the ozone sondes. Likewise, the SBUV tables could be outdated which might hint to a rise of Σ_{O_3} within the past 20 years (discussed e.g., by Borkowski & Krzyścin [53]). For shift and standard deviation are smaller (below 10% of $\overline{\Sigma}_{O_3}$), the linear extrapolated ozone profiles have been used in the simulation.
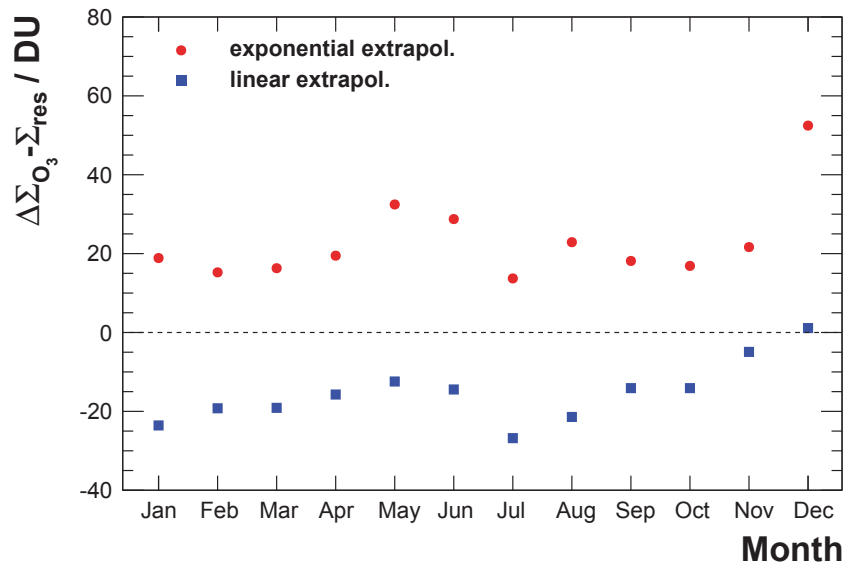
(a)
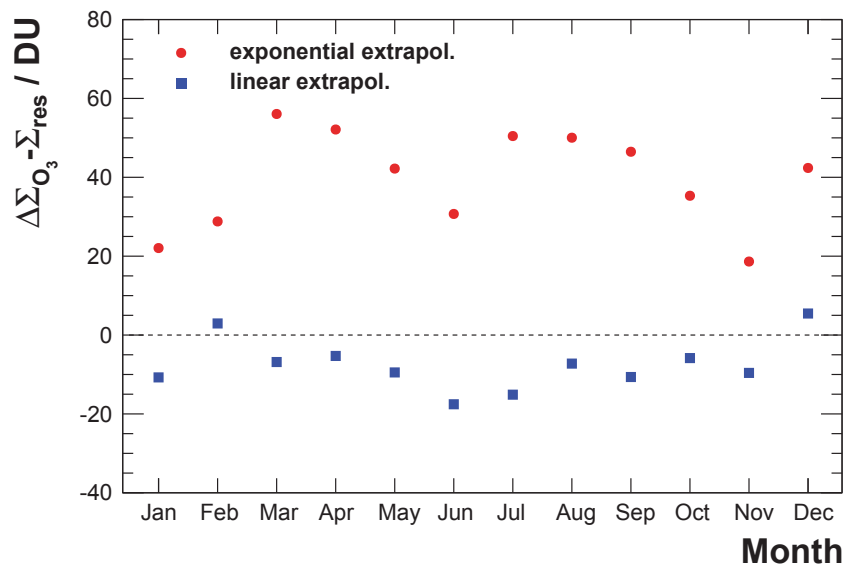
(b)

Figure 6.8: Comparison of exponential and linear extrapolation to total column ozone residuals from SBUV [57] for station Boulder. (a) Raw data from 1993; (b) Decadal sample of data from $2000 - 2012$.
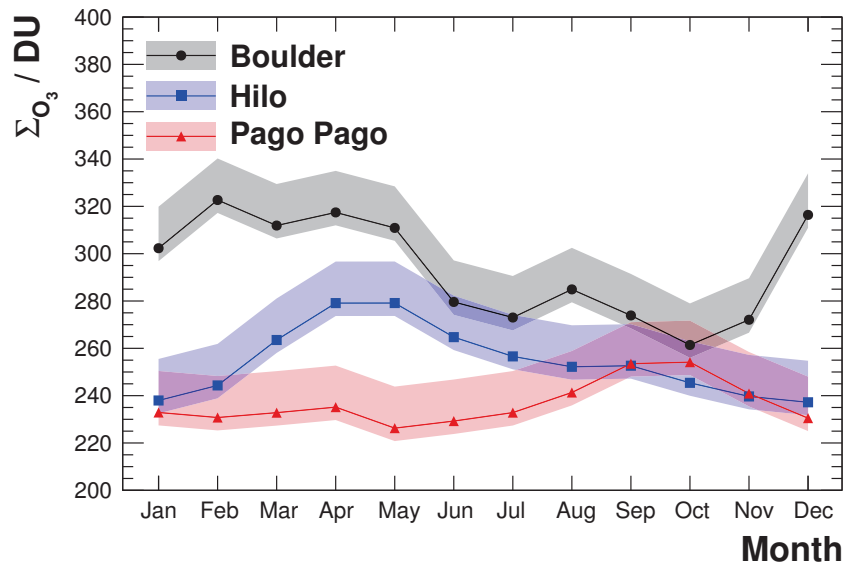
(a)
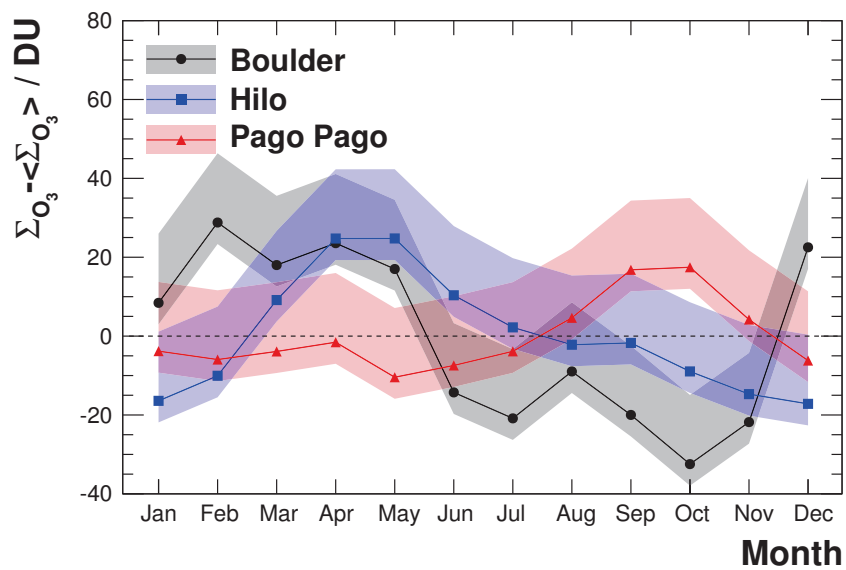
(b)

Figure 6.9: Seasonal variation of total ozone. Shown for Boulder (continental), Hilo (North Pacific) and Pago Pago (South Pacific). Error bands indicate the largest positive/negative deviation from Σ_{O_3} from SBUV [57]. (a) Total column ozone; (b) Monthly deviation from annual sample.

The seasonal behavior (Fig. 6.9a), agrees well with the expectation from the literature (Section 3.1.3). The total column ozone is highest for the northernmost site in Boulder ($\overline{\Sigma}_{O_3} = 301$ DU). It follows an annual cycle with highest ozone values in winter/spring and lowest values in summer/fall (Fig. 6.9b). This cycle is less pronounced for the oceanic sites of Hilo ($\overline{\Sigma}_{O_3} = 254$ DU), and Pago Pago ($\overline{\Sigma}_{O_3} = 237$ DU). The mean column ozone values are lower the closer to the equator. Σ_{O_3} at Pago Pago site follows the seasons on the southern hemisphere. The maximum in the annual ozone cycle is in September/October corresponding to spring on the southern hemisphere.

6.2.2   Influence on Light Transmission

The importance of ozone on the amount of transmitted UV light in case of JEM-EUSO will be studied in the following. The $\overline{\text{Off}\underline{\text{line}}}$ simulation framework has been used to simulate light transmission for 100 longitudinal shower profiles from Conex simulations. For each set of 100 showers, zenith angle and energy were fixed to $50°$, $60°$, and $70°$, and 10^{19} eV, 10^{20} eV, and 10^{21} eV, respectively. The same seeds have been used for the random generator in $\overline{\text{Off}\underline{\text{line}}}$ to allow for a shower to shower comparison. The ground reflection properties, namely phase function and albedo, were set to *forest* ($0.05 - 0.09$ in the given wavelength range) and *Lambertian*. The ground altitude is $1\,400$ m. Ozone shall be considered as decoupled from atmospheric variance by extracting the atmospheric state variables from US-StdA 76.

The total amount of transmitted UV photons at the aperture of the telescope, and separate light components will be compared. The simulation results for mean ozone profiles of Boulder and Hilo will be compared to a simulation without ozone attenuation (WOO). An artificial ozone profile has been created as scenario of ozone depletion localized above Boulder. This means the amount of ozone in the peak region was set to zero, so that $\Sigma_{O_3} \approx 100$ DU.

The results are listed in Tab. 6.1, example light profiles are shown in Fig. 6.10. The total attenuation due to ozone absorption lies at about 8.5% while slightly varying with zenith angle. The fluorescence light component is the least affected ($\approx 4\%$), the most affected is the scattered Cherenkov component ($24 - 25\%$) regardless of zenith angle. The attenuation of the reflected component of the Cherenkov light decreases with zenith angle from about 14% at $50°$ to about 8% at $70°$. At larger zenith angles, however, the contribution of reflected Cherenkov light to the total light at aperture is reduced, from 7% at $50°$ to around 1% at $70°$. Cherenkov light is strongly affected by the absorption of ozone because its emission increases with decreasing wavelength (see Section 1.2) where the ozone absorption is more effective compared to the main fluorescence emission line at 337 nm (cf., Fig. 3.9). No energy dependence on the ozone attenuation was found, since the amount of light produced scales with energy. If ozone is not taken into account for later energy reconstructions, the reconstructed energy would be systematically too low.

The difference of $\overline{\Sigma}_{O_3}$ between Boulder and Hilo amounts to ≈ 50 DU. This yields $\approx 1\%$ less light at the aperture, assuming an ozone profile of the former location. Compared to the overall effect of ozone absorption, this small scale ozone variation has no major influence on the light transmission in the UV-band,

but needs to be taken into account to minimize the systematic uncertainties.

The most prominent months in Boulder are February/April (higher overall ozone concentration) and October (less ozone) (see Fig. 6.6a, Fig. 6.9a). The amount of transmitted light at the aperture mimics that trend inversely, as can be seen in Fig. 6.11. The transmitted light decreases between $8 - 10\%$ compared to the case of no simulated ozone absorption. The highest transmission in case of Boulder is found in October (0.7% more photons compared to the mean) and lowest in February/April (0.47% less photons). The most over all light transmittance is observed for Pago Pago ozone profiles. It also reveals the least seasonal variance.

Regarding the artificial ozone profile ("ozone hole"), the simulation yields about 3% more light at the aperture compared to the actual ozone profile case.

Table 6.1: Attenuation of transmitted light, component-by-component for a primary energy of 10^{20} eV. The difference is shown as fraction of the number of photons reaching the aperture of JEM-EUSO in an ozone free atmosphere.

Station	Fluo. (dir.)	Cher. (gr.)	Cher. (scat.)	Total
		$\theta = 50°$		
Boulder	-0.043 ± 0.002	-0.146 ± 0.003	-0.25 ± 0.008	-0.092 ± 0.008
Hilo	-0.038 ± 0.002	-0.138 ± 0.003	-0.24 ± 0.008	-0.087 ± 0.009
		$\theta = 60°$		
Boulder	-0.044 ± 0.002	-0.124 ± 0.004	-0.25 ± 0.006	-0.089 ± 0.001
Hilo	-0.040 ± 0.002	-0.117 ± 0.004	-0.24 ± 0.006	-0.084 ± 0.001
		$\theta = 70°$		
Boulder	-0.045 ± 0.0014	-0.082 ± 0.005	-0.26 ± 0.006	-0.082 ± 0.002
Hilo	-0.041 ± 0.0014	-0.077 ± 0.004	-0.24 ± 0.006	-0.077 ± 0.002
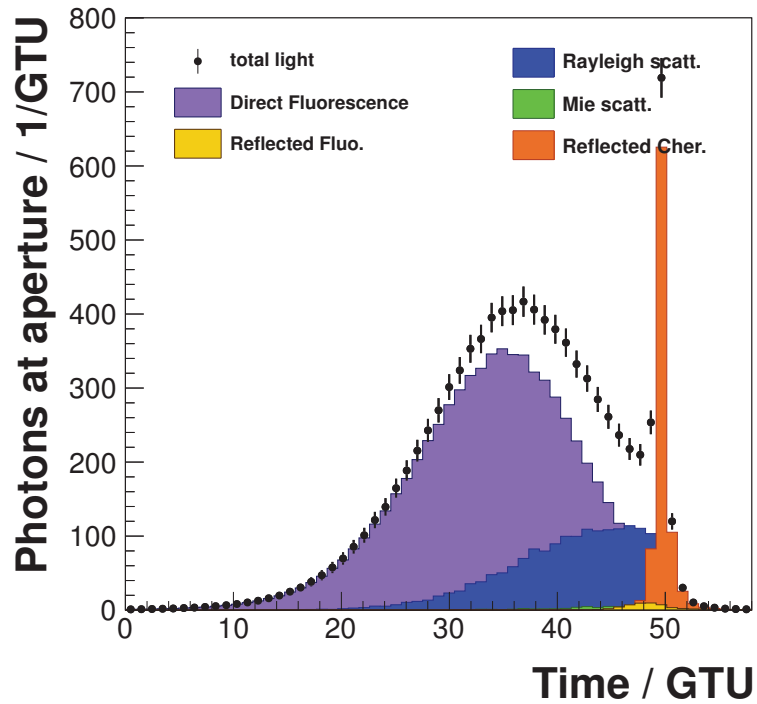
(a) No ozone
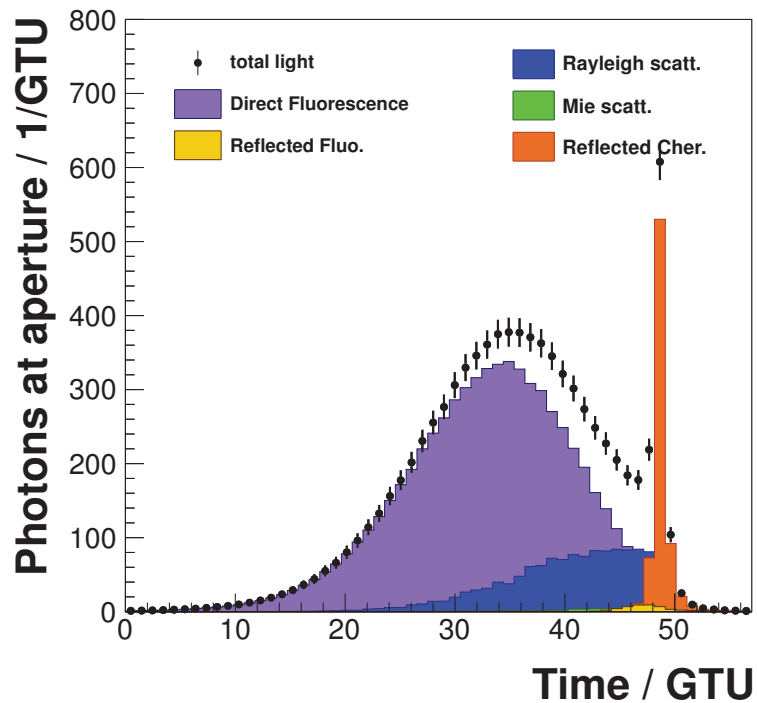
(b) Boulder ozone profile

Figure 6.10: Example light profiles for attenuation by ozone simulated with $\overline{\text{Off}}\underline{\text{line}}$ ($E = 10^{20}$ eV, $\theta = 50°$).
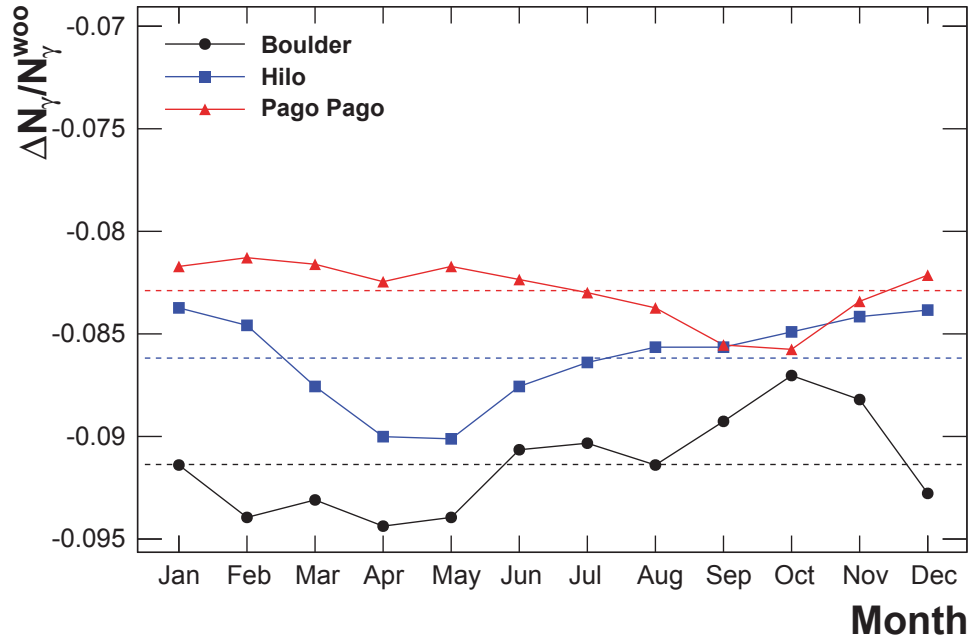
Figure 6.11: Monthly change of light transmission due to ozone absorption as ratio of divergence $\Delta N_\gamma = N_\gamma - N_\gamma^{\text{WOO}}$ and number of photons without ozone absorption N_γ^{WOO}. The dashed lines indicate the annual sample for the three locations Boulder, Hilo, and Pago Pago.

6.3 Atmospheric Scenarios

Different atmospheric scenarios have been simulated for 100 showers each. A scenario comprises monthly mean atmospheric profiles, an ozone profile of the same month, and a probable albedo. First, the local variations of the atmosphere and albedo will be studied regarding the light reaching the aperture of JEM-EUSO (cf., Section 5.3). Afterward, a comparison for nine of the global locations will be done. Finally, the same study has been conducted on selected dates at four locations to verify the appropriate use of monthly mean atmospheric profiles in the case of JEM-EUSO.

In case of Pico (Azores), the albedo selected was *water* for each simulation. In the Malargüe scenario *Savannah* was selected for $-2° \leq \Delta\Phi \leq 0$, *snow* for $\Delta\Phi = +1°$ (representing a glacier in the Andes), and *forest* for $\Delta\Phi = +2°$. The resulting total number of photons, as well as the component-by-component numbers of photons at the JEM-EUSO aperture are listed in Appendix Tab. C.1. The statistical uncertainty is of the order of 1%. In both cases, the number of fluorescence photons varies by less than 1% with respect to the base location (Pico (8517 photons), Malargüe (7919 photons)) if the albedo and surface altitude are similar. Within the resolution of JEM-EUSO, all locations around Pico will be the same by means of energy reconstruction. The largest divergence is found for the Andes ($\Delta\Phi = -1°$), where the surface altitude is above 3 km. While the total number of photons increases by 120% due to the high snow albedo,

the number of fluorescence photons decreases by about 6%. In Fig. 6.12, the number of photons of each simulated light component is displayed relative to the total amount of photons. A strong dependence of the light profiles on the albedo becomes obvious in Fig. 6.12b. Especially the high albedo of the simulated glaciers alters the total light, as well as the ratios significantly. The simulated glacier at an altitude of 3 km is comparable to an albedo of a low altitude cloud. Since proper treatment of clouds has not yet been implemented to $\overline{Off\underline{line}}$, no quantitative conclusions can be drawn. Qualitatively, the detected light could be dominated by the reflected light components. A further study of the albedo and phase functions in the UV would be reasonable.

The comparison of the ratio of light at aperture for different atmospheric conditions is shown for all locations in Appendix Fig. C.1, winter and summer separately. The albedo had been set to Savannah in all cases. Ozone profiles of Hilo, Boulder, and Pago Pago have been used in accordance to month and location. The ratios between the different light components vary only slightly from location to location. In Fig. 6.13, the mean relative deviation from the averaged amount of fluorescence light at the aperture is shown for different atmospheric conditions. The maximum negative divergence from the corresponding average in summer is found for the Alëutian islands (-3%) and the maximum positive divergence 1% for Antofagasta. In winter, the divergences are -6% for the Alëutian islands and 4% for Pago Pago. The Azores and Malargüe display the smallest divergence from the average (below $\pm 1\%$). The difference in the amount of photons between winter and summer is $\leq 3\%$ for most locations. The amount of scattered Cherenkov light behaves similarly in summer ($^{+4}_{-6}\%$), but the divergences are larger in winter ($^{+6}_{-10}\%$).

For four of ten locations, the Alëutian islands, Andaman island, Antofagasta, and the Azores, a monthly mean atmospheric profile has been compared to a selected date with respect to the amount of emitted and transmitted light. The selected dates represent a typical or an extremely warm/cold atmospheric condition at the corresponding location [59]. The results are depicted as average amount of light at the aperture with error bars representing the standard deviation of the distribution (Fig. 6.14) and listed in Appendix Tab. C.4. The standard deviation lies between about 11% for fluorescence and scattered Cherenkov light, and about 6% for reflected fluorescence and Cherenkov light. The absolute divergence of the total amount of transmitted light between the monthly mean profile and a selected date is 5% for the Alëutian islands, 1% for Antofagasta, and below 1% for Andaman island and for the Azores. The closer to the tropics, the more uniform are the atmospheric conditions even on short terms. With respect to the resolution in energy of JEM-EUSO, the actual atmospheric profiles should be taken into account for any elaborated analysis.
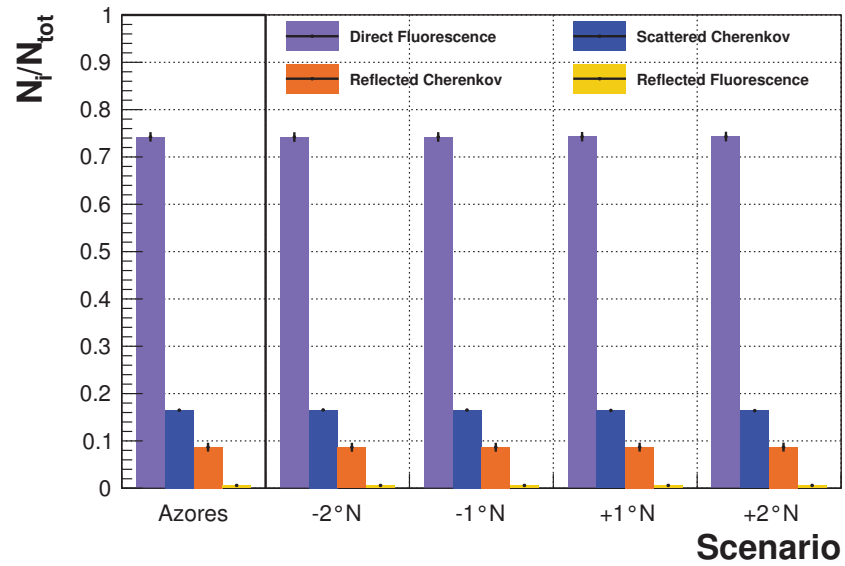
(a)
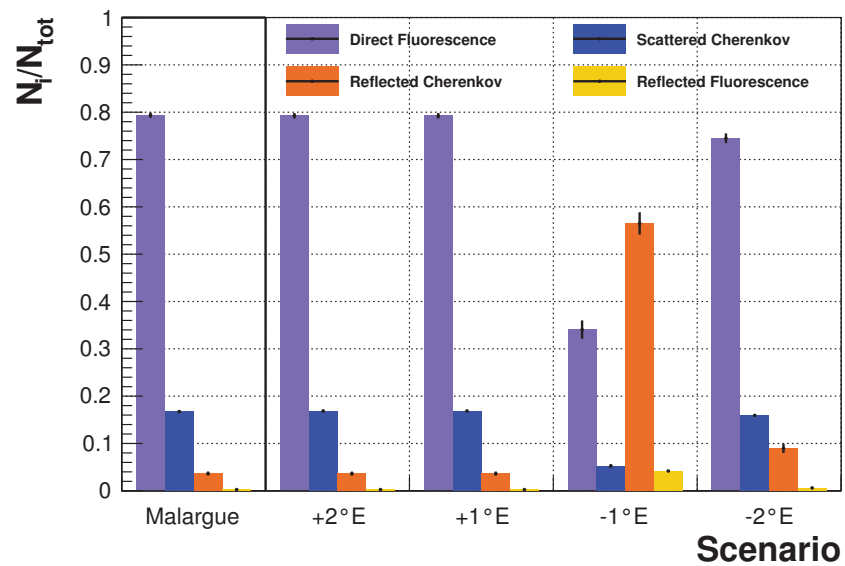
(b)

Figure 6.12: The ratio of light at aperture for different atmospheric conditions. (a) Azores, January 2009. The January ozone profile of Hilo data has been used. (b) Malargüe, November 2009. The May ozone profile of Boulder data has been used.
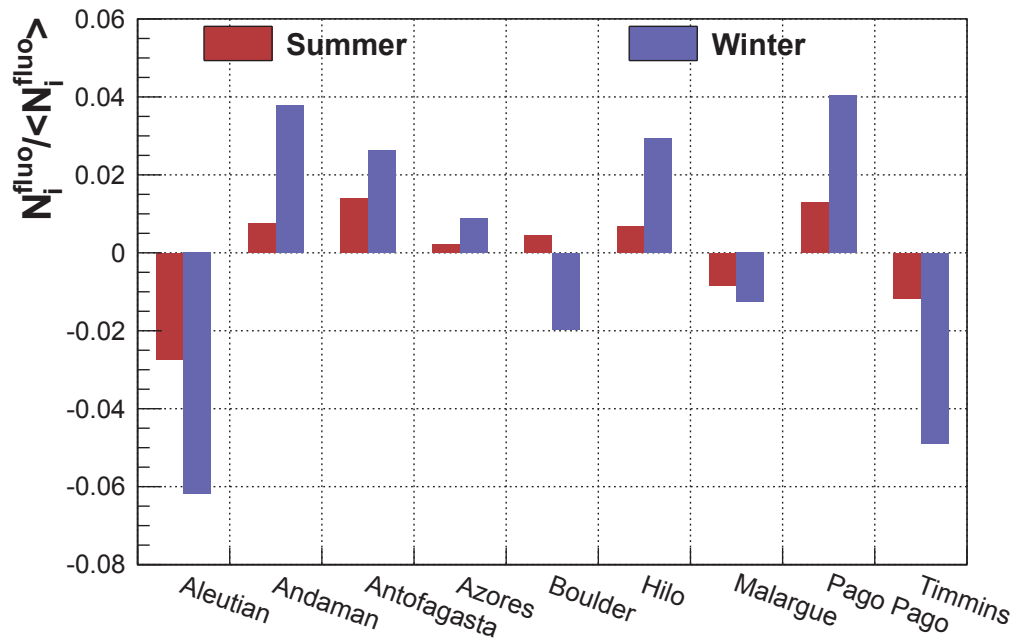
(a)
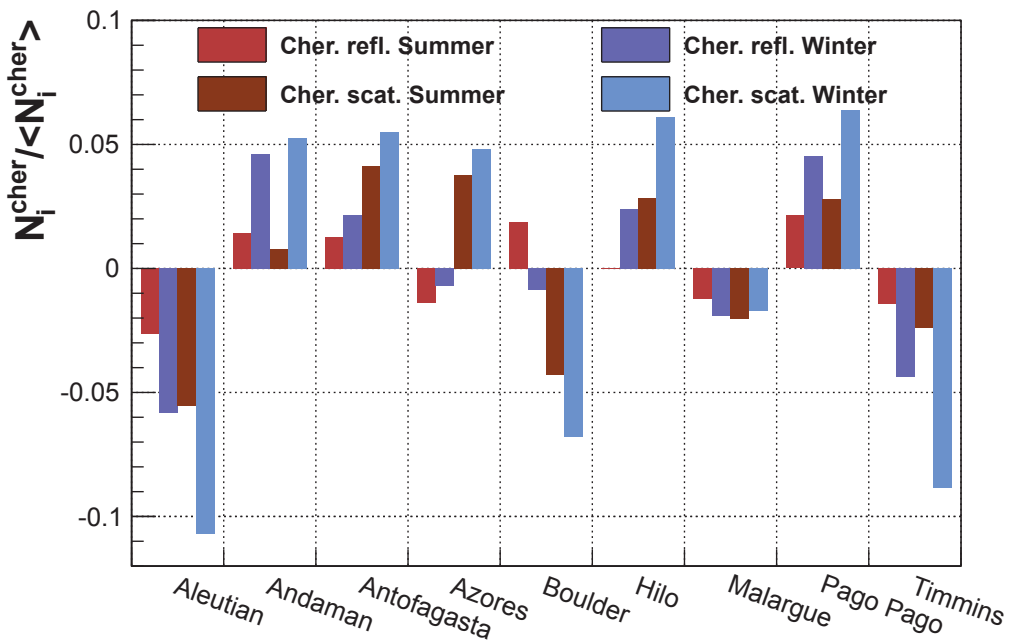
(b)

Figure 6.13: Mean relative deviation from average of light at aperture for different atmospheric conditions. The albedo had been set to Savannah in all cases. Ozone profiles of Hilo, Boulder, and Pago Pago have been used according to month and location. Winter refers to January on northern hemisphere, July on southern, summer vice versa. (a) Direct fluorescence light. (b) Reflected and scattered Cherenkov light.
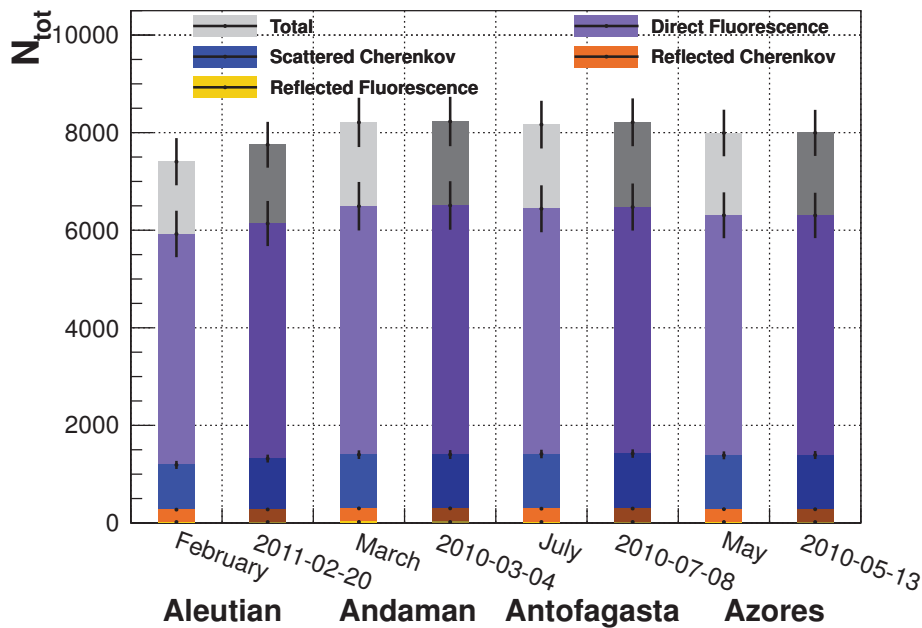
Figure 6.14: Average light at aperture for typical atmospheric conditions at selected locations. The error bars represent the standard deviation of the distribution. The light transmission is compared for a selected date (dark hue) and a mean atmospheric profile.

6.4 Summary & Conclusion

For a space-borne observatory, the attenuation through Rayleigh scattering is far more significant than the attenuation by Mie scattering. Most aerosols occur in the lower troposphere (3 km from ground), whereas a typical shower at zenith angle $60°$ develops at about 10 km height. If affective, Mie attenuation will mainly influence the ground reflected components of the light emitted by an EAS. An energy reconstruction using the Cherenkov reflection peak, should therefore take a proper aerosol profile into account.

The attenuation by ozone is important for any space-borne experiment. The total impact on the UV light transmission is about 8.5% less compared to an ozone free atmosphere. Therefore, the attenuation by ozone needs to be taken into account for the energy reconstruction. The seasonal variance in transmission, as well as the variance between different example locations is at the level of 1%, but it should be taken into account for the systematic uncertainties.

The study on the overall impact of the atmosphere on emission and transmission of the UV light from EAS yields a strong dependence on the actual simulated albedo which should be studied further. Regarding the global operation of JEM-EUSO, the amount of light diverges by about 10% between locations at high latitude and close to the equator. The comparison between the monthly mean profile and a single date yields that, though monthly mean profiles are a good choice for locations in the tropics, in the temperated zone the actual atmospheric profile should be taken into account for the energy reconstruction.

Conclusion

Together with colleagues from the JEM-EUSO collaboration, a reduced version of the $\overline{\text{Off}}\underline{\text{line}}$ software framework has been adopted to JEM-EUSO. In this context, the existing atmospheric simulation has been revised. Improvements by means of computation time for the atmospheric profiles and depth in case of very inclined shower geometries have been made. The new algorithm gives reliable results compared to the spheroidal CORSIKA parametrization of atmosphere. The algorithm is up to eight times faster compared to the old $\overline{\text{Off}}\underline{\text{line}}$ algorithm. In this process, new functions have been added to existing classes, e.g., trapezoidal integration and line-ellipsoid intersection. New classes and modules had to be developed to adjust to the space-borne observation. Crucial to the later analysis, the UV absorption by ozone has been included in the simulation. The concept of an Earth surface, consisting of albedo and outgoing phase function, has been introduced to handle the computation of UV reflection at ground level. The reflected Cherenkov and fluorescence light observed by JEM-EUSO is calculated by a new module in the simulation chain. Photon trajectoried from under ground are discarded from simulation. All algorithms have been thoroughly tested.

The Global Data Assimilation System (GDAS) has been chosen as a global atmospheric model (GAM) to provide atmospheric data such as temperature, pressure, and humidity profiles. From 181×360 possible GDAS grid points, ten have been selected as examples. The locations cover the subarctics, northern and southern temperate zone, subtropics, and tropics, as well as land and ocean sites. They have been compared to the U.S. Standard Atmosphere 1976 (US-StdA 76) by means of atmospheric depth and light emission. Monthly mean atmospheric profiles have been compiled for each location and used for simulation. For some locations, deviations in the vertical atmospheric depth up to $30\,\mathrm{g\,cm}^{-2}$ compared to the values computed with the US-StdA 76 have been found. If not addressed in a later reconstruction of real data, this will lead to a bias towards deeper X_max close to the equator and vice versa in the subarctics. For comparison of these numbers to the spacial resolution of JEM-EUSO of about 500 m, a shower at $E = 10^{20}$ eV and $\theta = 60°$ has been simulated for the most extreme atmospheric profiles. The largest deviation of X_max was about $1\,300$ m which might be resolvable with the resolution of JEM-EUSO. The amount of emitted fluorescence photons changes by $\pm(5-6)\%$. This should also have an influence on the energy reconstruction, although the best reconstruction precision currently reached in clear sky simulation is about 20%. The simulations show a influence on the emission of Cherenkov light of the same order of magnitude as for fluorescence light (up to $\pm 4\%$). However, Cherenkov light is only measured via scattering or

reflection. For a quick analysis, the usage of US-StdA 76 will be sufficient, but real atmospheric profiles need to be taken into account for an elaborated analysis. From the comparison of different locations within the wide field of view (FOV) of JEM-EUSO, the atmospheric profile closest to the nadir position on ground will be sufficient, except for some cases of showers close to the edge of the FOV.

The $\overline{\text{Off}\underline{\text{line}}}$ software has been used to compare the transmission properties for a clear atmosphere, as measured by the Pierre Auger collaboration in Malargüe. A distance of 40 km at ground level (1 400 m) and at ISS orbit (400 km) have been evaluated by means of attenuation of light. The attenuation by Rayleigh scattering dominates in both cases over Mie attenuation where few aerosols are assumed. At the main fluorescence line of 337 nm the attenuation in the ground-based scenario is almost 98% compared to 50% in the space-borne case. Although a significant amount of light is still attenuated, it is far less. The influence of the state of the atmosphere on the Rayleigh attenuation is of the order magnitude of $\pm 1\%$.

The absorption of UV light by ozone has been studied for three examples. Mean monthly profiles of ozone have been calculated from NOAA ozone sounding data and processed with the simulation chain of $\overline{\text{Off}\underline{\text{line}}}$. Though its role is insignificant for ground-based fluorescence detection, it reduces the amount of transmitted light on average by 8.5% for a space-borne experiment. The change of season affects the ozone abundance, hence the transmission varies by about $\pm 1\%$ throughout the year. The least ozone is found close to the equator resulting in about 3% less absorption compared to a continental ozone profile at higher latitude. For systematics, proper ozone profiles should be taken into account.

Last but not least, the overall impact of the atmosphere on emission an transmission has been studied on a set of simulated events in different conditions. The assumed ground properties strongly affect the total amount of light at the JEM-EUSO aperture. UV albedo and phase functions of different natural and anthropogenic surfaces should be studied further. The total amount of transmitted light varies by about 10% between atmospheric conditions at high latitudes ($51°$) and close to the equator. The monthly mean profiles have also been compared to single date profiles by means of total amount of light at the telescope aperture. For locations in the tropics this analysis yields no significant change of the amount of light. For locations in subarctic regions or the cold temperated zone, single date profiles will be the better choice. Although not significant for the shower depth, the monthly mean profiles and single date profiles are important for the energy reconstruction.

From the presented results in this work, it has to be concluded that for any space-based observatory near event-time atmospheric and ozone profiles must be used for the reconstruction of the air shower events. The future data source and resolution of the observatory may vary from the herein presented, though all atmosphere related conclusions hold in general. For the JEM-EUSO experiment, it suggested to provide a database with altitude-dependent atmospheric state variables which will be filled in accordance to the time and position of the ISS. The state variables can be provided from corresponding GDAS data. The ozone profiles can be given for several large-scale regions in parametrized form. The ground albedo of several typical surfaces is also provided in parametrized form.

APPENDIX **A**

List of Acronyms

AGN Active Galactic Nuclei

AMS Atmospheric Monitoring System

ASCII American Standard Code for Information Interchange

BRDF bidirectional reflectance distribution function

CCB Cluster Control Board

CFC Chlorofluorocarbon

CLF Central Laser Facility

CMB cosmic microwave background

CNES French Space Agency

CORSIKA Cosmic Ray Simulations for Kascade and Auger

CR cosmic rays

DAQ Data Acquisition

DWD Deutscher Wetterdienst

EAS extensive air shower

EC elementary cell

ECMWF European Centre for Medium-Range Weather Forecasts

EGM 08 Earth Gravitational Model 2008

EECR extreme energy cosmic rays

ELS Electron Light Source (compact electron linear accelerator)

ERA ECMWF Re-Analysis

ERA-15 15-year ERA (starting 1979)

ERA-40 40-year ERA (September 1957 to August 2002)

ERA-Interim interim ERA as replacement for 40-year ERA (ERA-40) (January 1979 – today)

ESA European Space Agency

ESAF EUSO Simulation and Analysis Framework

EUSO Extreme Universe Space Observatory

EUSO-TA Extreme Universe Space Observatory prototype at the Telescope Array site

EUSO-Balloon Extreme Universe Space Observatory prototype on board a balloon

FOV field of view

GAM global atmospheric model

GDAS Global Data Assimilation System (December 2004 – today)

GLS Global Light System

GEANT4 Geometry And Tracking

GOES Geostationary Operational Environmental Satellite

GTU Gate Time Unit

GZK Greisen-Zatsepin-Kuz'min

HECR high energy cosmic rays

HTV H-II transfer Vehicle

IR infrared

ISS International Space Station

JAXA Japan Aerospace Exploration Agency

GPS Global Positioning System

GRB Gamma Ray Bursts

JEM-EUSO Extreme Universe Space Observatory on board the Japanese Experiment Module

KASCADE Karlsruhe Shower Core and Array Detector

LED light-emitting diode

LIDAR Light Detection and Ranging

MAPMT multi-anode photomultiplier tube

MARS Meteorological Archival and Retrieval System (ECMWF)

MASS Maximum-energy Auger (Air)-Shower Satellite

MC Monte Carlo

NASA National Aeronautics and Space Administration

NCEP National Centers for Environmental Prediction

NIMA National Imagery and Mapping Agency

NOAA National Oceanic and Atmospheric Administration

OWL Orbiting Wide-angle Light-collectors

PDM photo-detector module

PMMA Polymethyl-Metacrylate (UV transmitting)

ROOT Rapid Object-Oriented Technology

ROSCOSMOS Russian Federal Space Agency

SBUV solar backscattered ultraviolet

SNR Supernova Remnants

TA Telescope Array

TLE transient luminous events

UHE ultra-high energy

UHECR ultra-high energy cosmic rays

US United States

US-StdA 76 U.S. Standard Atmosphere 1976

UV ultraviolet

WGS 84 World Geodetic System 1984

XML Extensible Markup Language

Diversity of State Variables

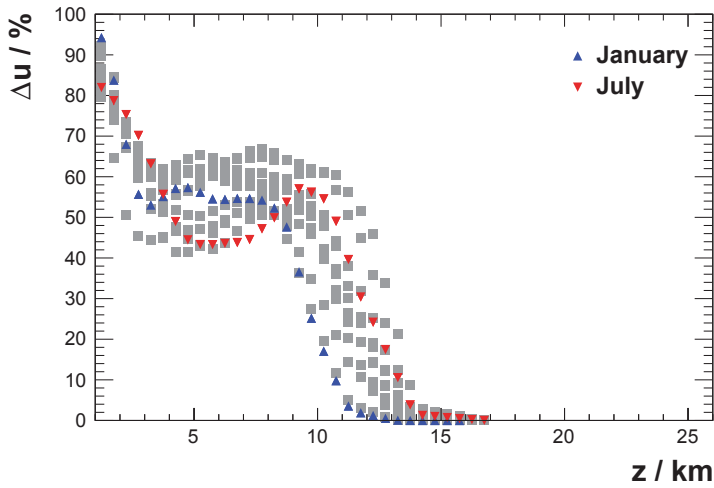## B.1 Monthly Diversity of Atmospheric State

Pressure
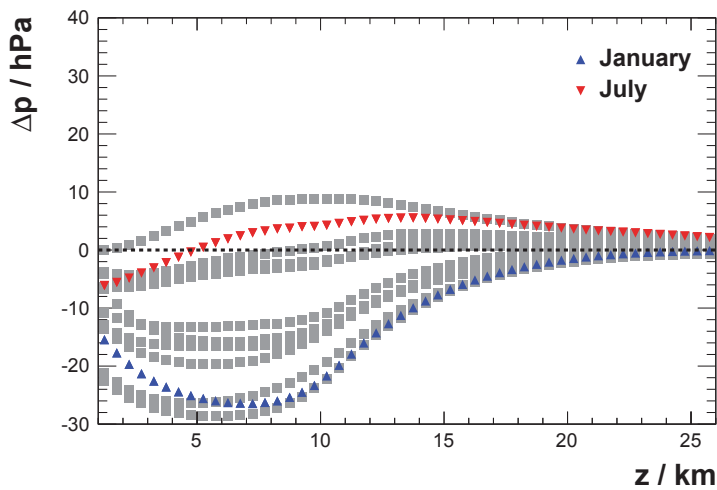
Figure B.1: GDAS data for Alëutian islands, 2009. The divergence in atmospheric pressure with respect to US-StdA 76. January and July are highlighted.
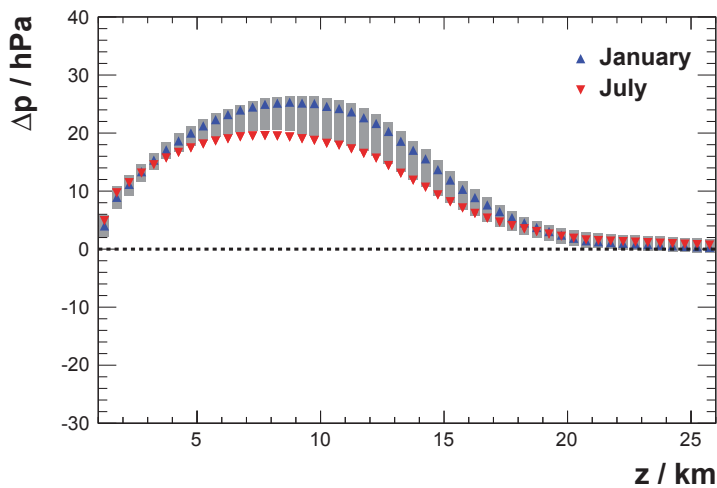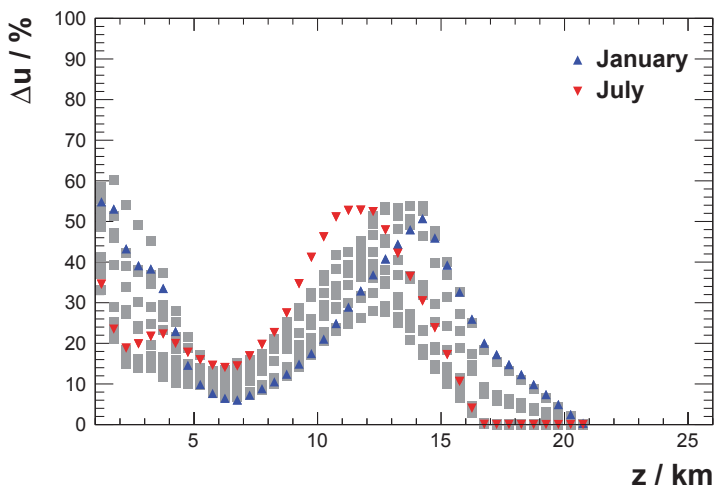

Figure B.2: GDAS data for Antofagasta (Chile), 2009. The divergence in atmospheric pressure with respect to US-StdA 76. January and July are highlighted.
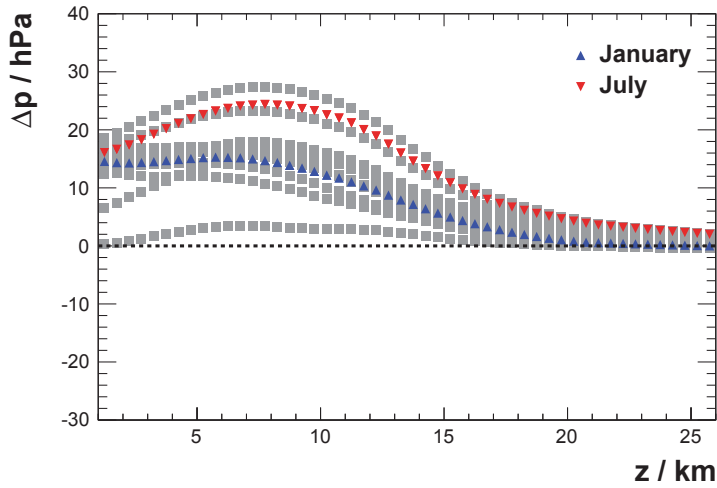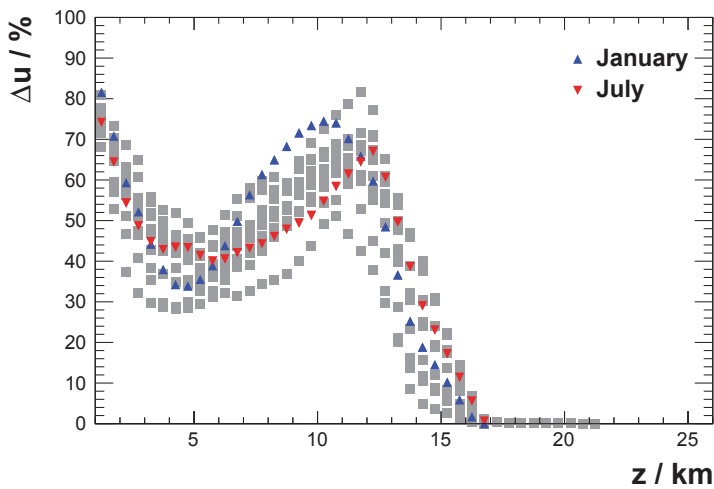
Figure B.3: GDAS data for Pico (Azores), 2009. The divergence in atmospheric pressure with respect to US-StdA 76. January and July are highlighted.
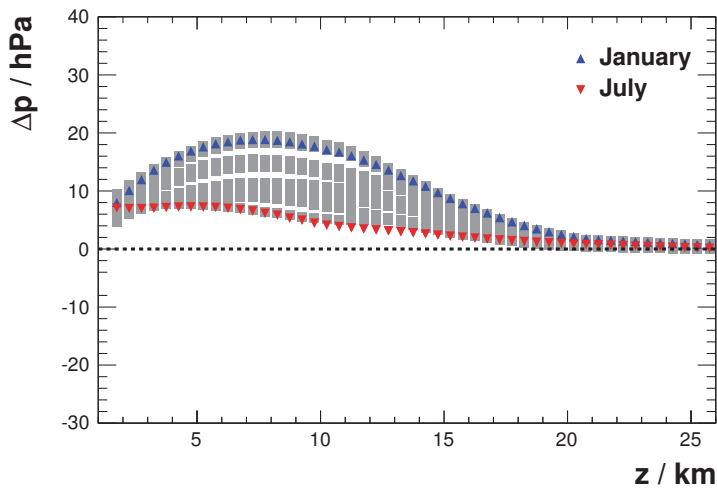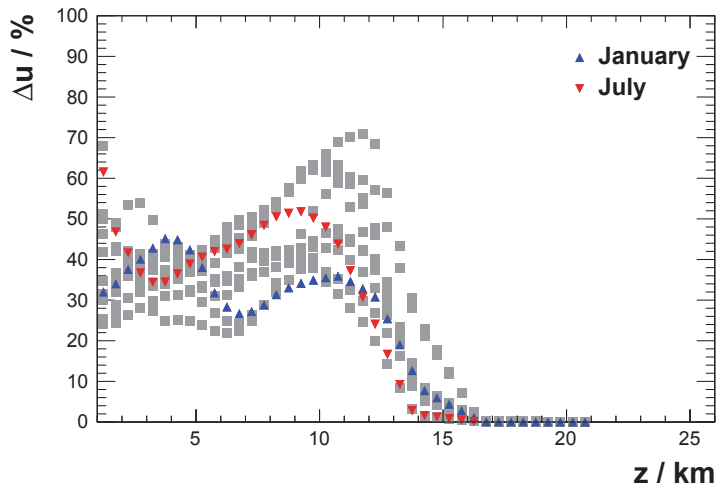

Figure B.4: GDAS data for Malargüe (Argentina), 2009. The divergence in atmospheric pressure with respect to US-StdA 76. January and July are highlighted.
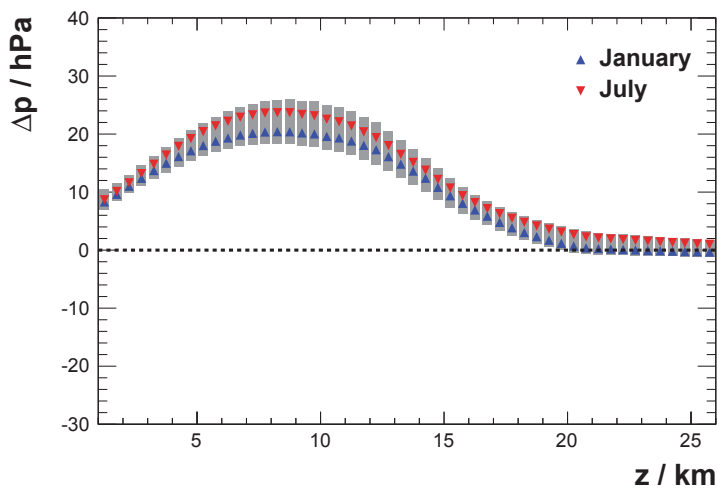
Figure B.5: GDAS data for Hilo (Hawaii, USA), 2012. The divergence in atmospheric pressure with respect to US-StdA 76. January and July are highlighted.
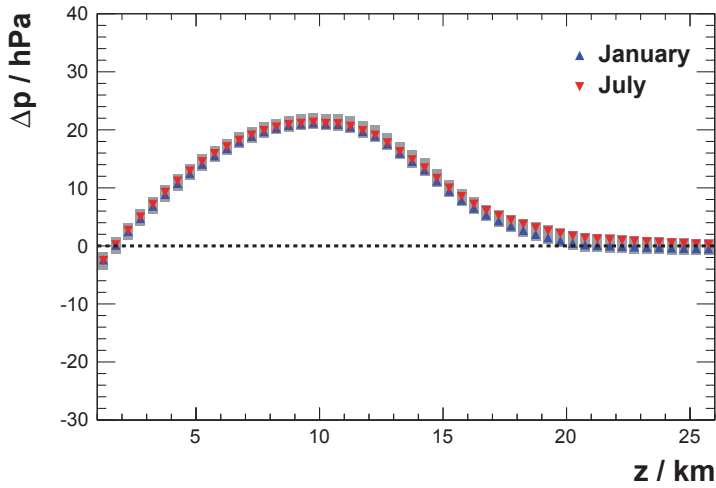
Figure B.6: GDAS data for Andaman Island (Bay of Bengal, India), 2009. The divergence in atmospheric pressure with respect to US-StdA 76. January and July are highlighted.
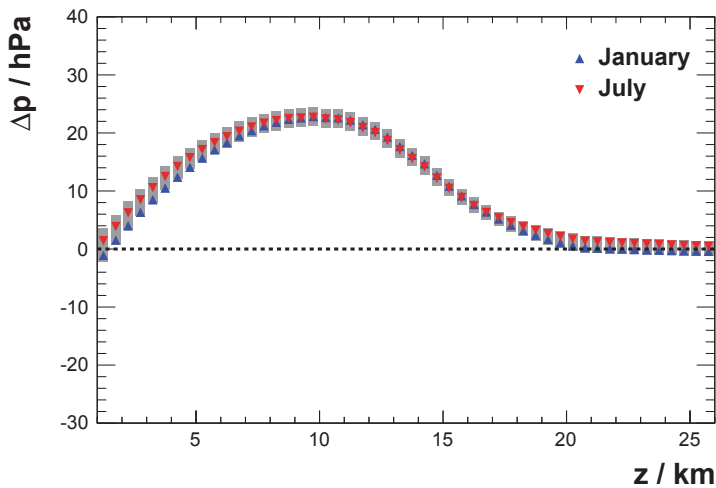
Figure B.7: GDAS data for Pago Pago (American Samoa), 2012. The divergence in atmospheric pressure with respect to US-StdA 76. January and July are highlighted.
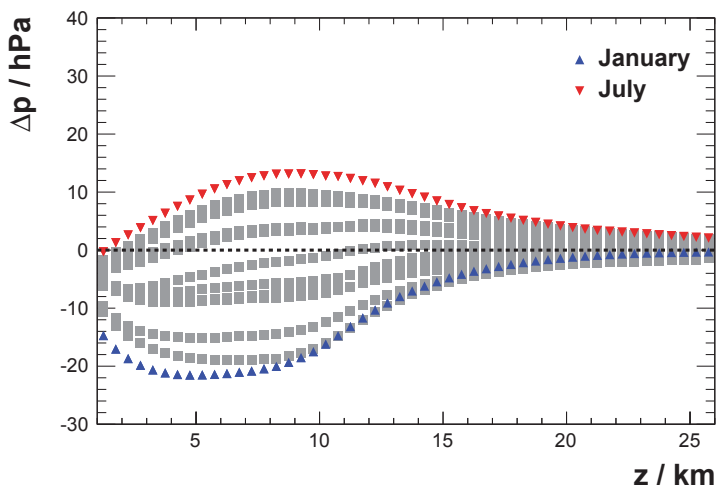
Figure B.8: GDAS data for Timmins (Ontario, Canada), 2012. The divergence in atmospheric pressure with respect to US-StdA 76. January and July are highlighted.

Temperature
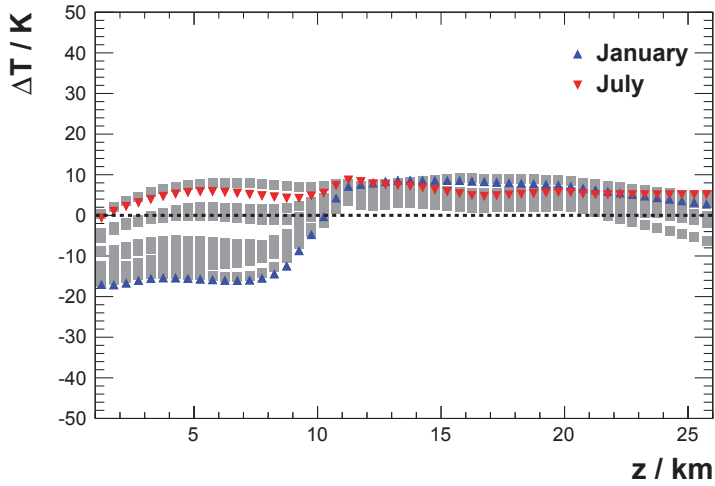
Figure B.9: GDAS data for Alëutian islands, 2009. The divergence in temperature with respect to US-StdA 76. January and July are highlighted.
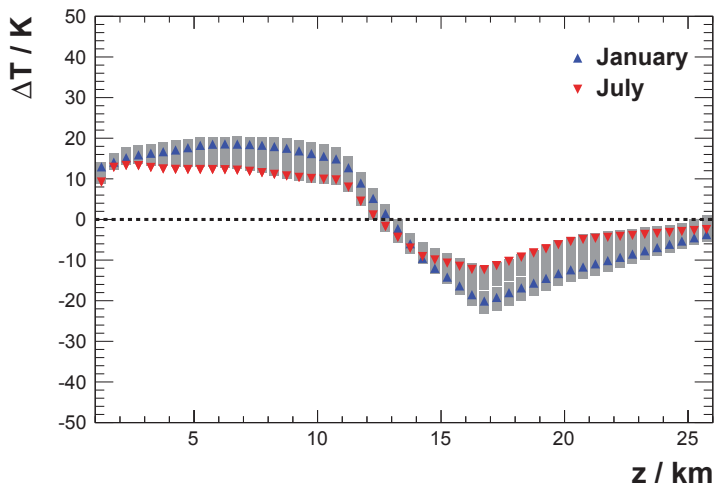
Figure B.10: GDAS data for Antofagasta (Chile), 2009. The divergence in temperature with respect to US-StdA 76. January and July are highlighted.
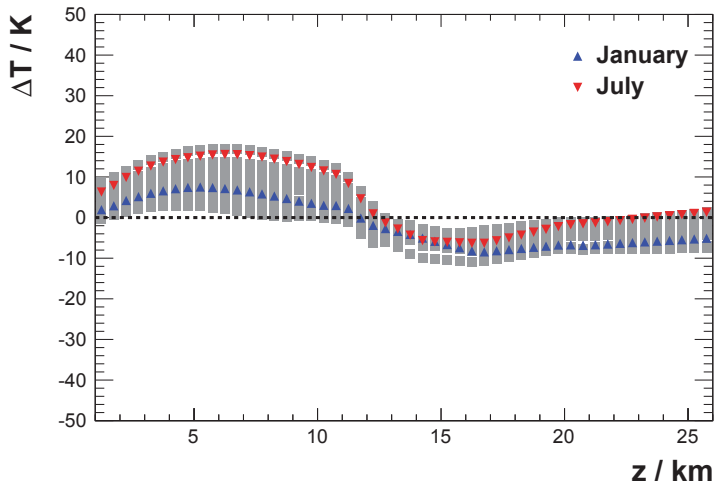
Figure B.11: GDAS data for Pico (Azores), 2009. The divergence in temperature with respect to US-StdA 76. January and July are highlighted.
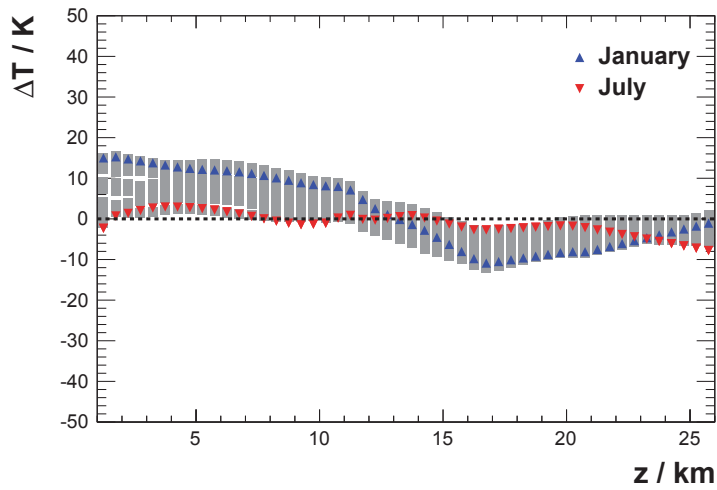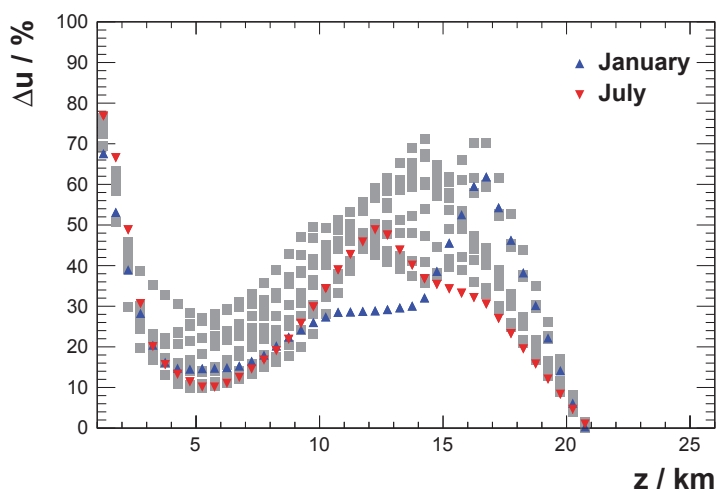
Figure B.12: GDAS data for Malargüe (Argentina), 2009. The divergence in temperature with respect to US-StdA 76. January and July are highlighted.
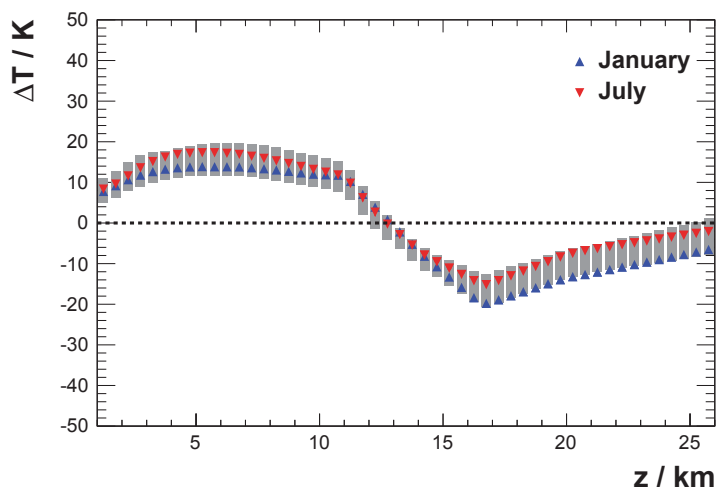
Figure B.13: GDAS data for Hilo (Hawaii, USA), 2012. The divergence in temperature with respect to US-StdA 76. January and July are highlighted.
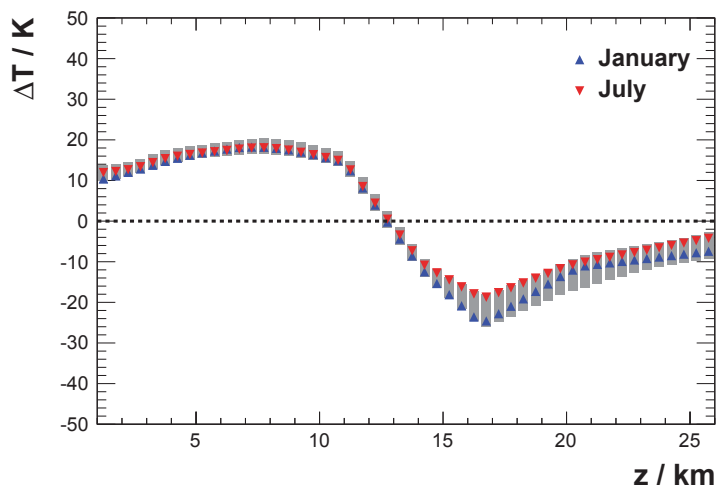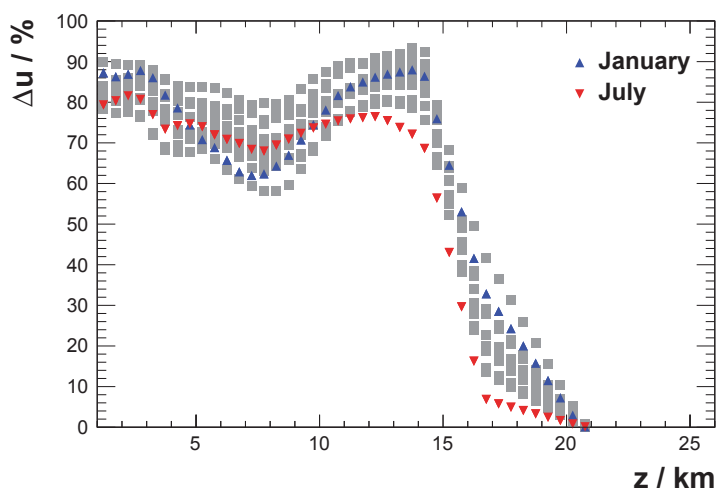

Figure B.14: GDAS data for Andaman Island (Bay of Bengal, India), 2009. The divergence in temperature with respect to US-StdA 76. January and July are highlighted.
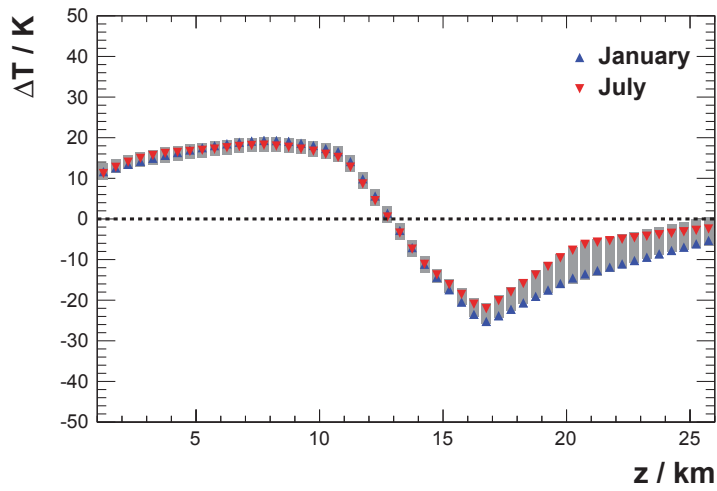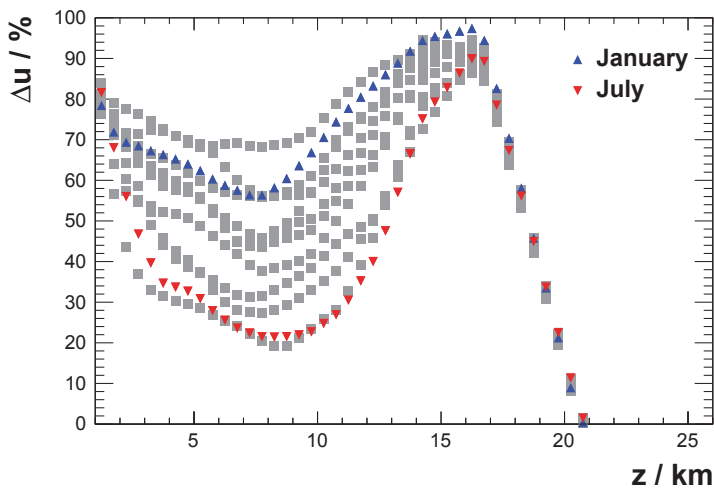
Figure B.15: GDAS data for Pago Pago (American Samoa), 2012. The divergence in temperature with respect to US-StdA 76. January and July are highlighted.
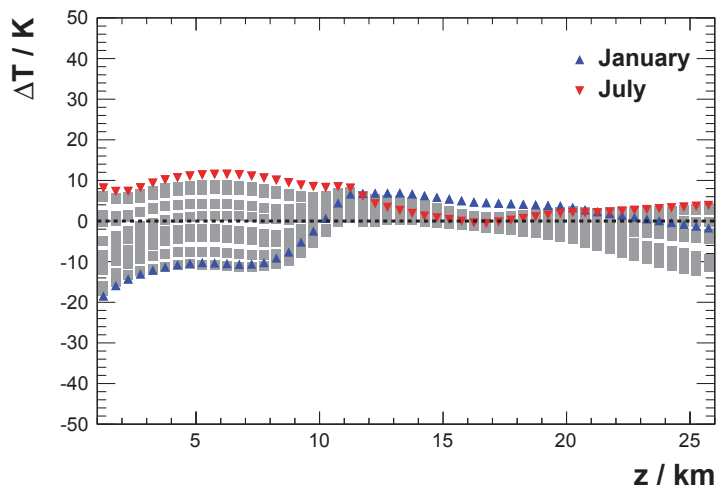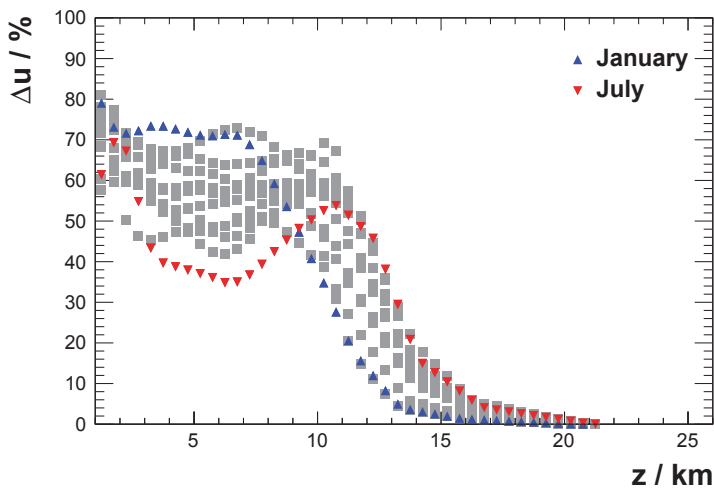

Figure B.16: GDAS data for Timmins (Ontario, Canada), 2012. The divergence in temperature with respect to US-StdA 76. January and July are highlighted.

Humidity
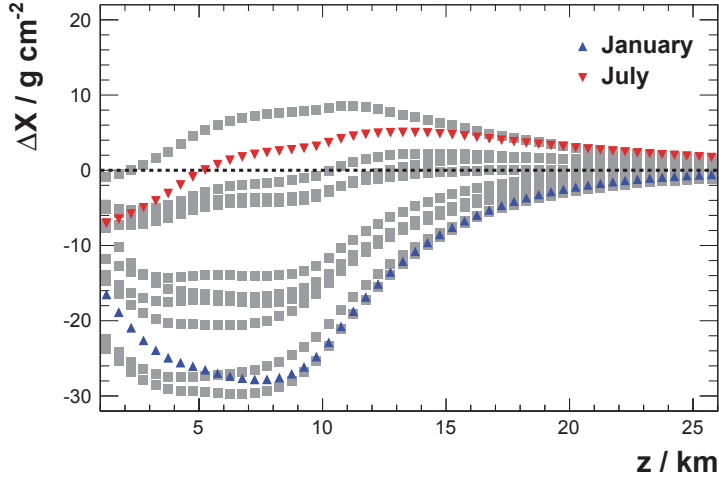

Figure B.17: GDAS data for Alëutian islands, 2009. The divergence in humidity with respect to US-StdA 76. January and July are highlighted.
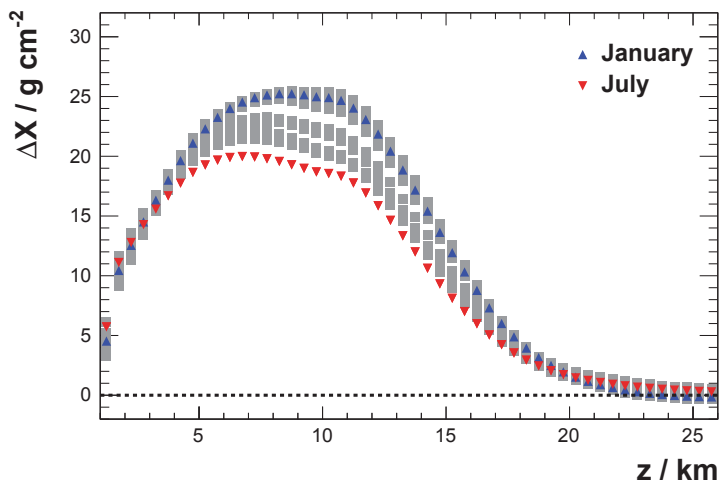

Figure B.18: GDAS data for Antofagasta (Chile), 2009. The divergence in humidity with respect to US-StdA 76. January and July are highlighted.
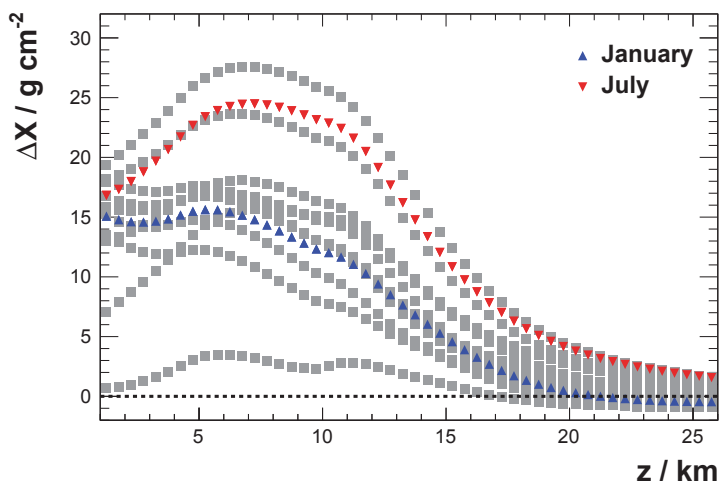

Figure B.19: GDAS data for Pico (Azores), 2009. The divergence in humidity with respect to US-StdA 76. January and July are highlighted.

Figure B.20: GDAS data for Malargüe (Argentina), 2009. The divergence in humidity with respect to US-StdA 76. January and July are highlighted.

Figure B.21: GDAS data for Hilo (Hawaii, USA), 2012. The divergence in humidity with respect to US-StdA 76. January and July are highlighted.

Figure B.22: GDAS data for Andaman Island (Bay of Bengal, India), 2009. The divergence in humidity with respect to US-StdA 76. January and July are highlighted.

Figure B.23: GDAS data for Pago Pago (American Samoa), 2012. The divergence in humidity with respect to US-StdA 76. January and July are highlighted.
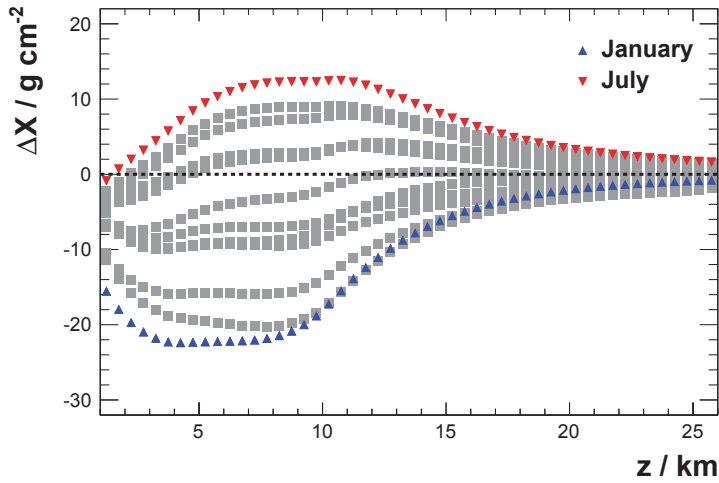

Figure B.24: GDAS data for Timmins (Ontario, Canada), 2012. The divergence in humidity with respect to US-StdA 76. January and July are highlighted.
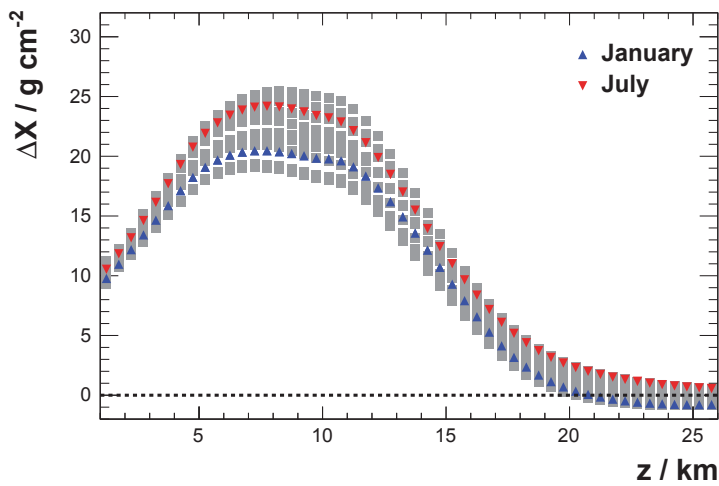
B.2   Monthly Divergence of Vertical Atmospheric Depth

Figure B.25: GDAS data for Alëutian islands, 2009. The divergence in atmospheric depth with respect to US-StdA 76. January and July are highlighted.

Figure B.26: GDAS data for Antofagasta (Chile), 2009. The divergence in atmospheric depth with respect to US-StdA 76. January and July are highlighted.

Figure B.27: GDAS data for Pico (Azores), 2009. The divergence in atmospheric depth with respect to US-StdA 76. January and July are highlighted.

Figure B.28: GDAS data for Timmins (Ontario, Canada), 2012. The divergence in atmospheric depth with respect to US-StdA 76. January and July are highlighted.

Figure B.29: GDAS data for Hilo (Hawaii, USA), 2012. The divergence in atmospheric depth with respect to US-StdA 76. January and July are highlighted.
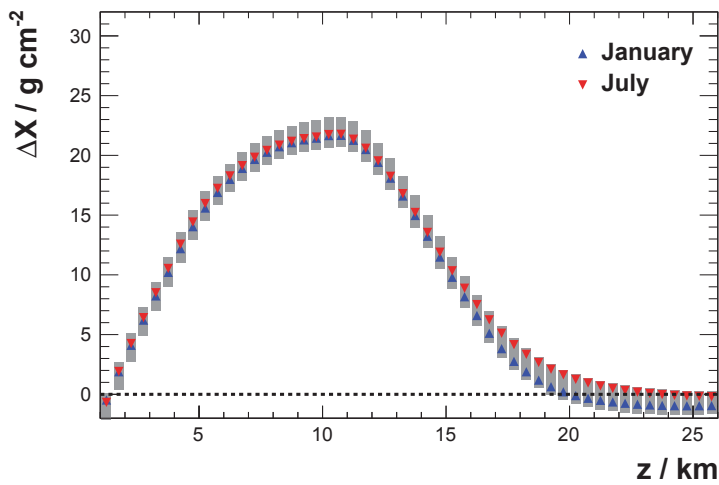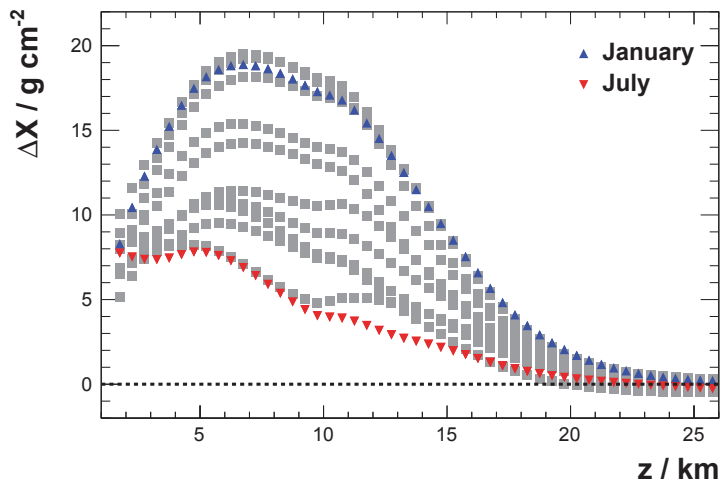

Figure B.30: GDAS data for Andaman Island (Bay of Bengal, India), 2009. The divergence in atmospheric depth with respect to US-StdA 76. January and July are highlighted.

Figure B.31: GDAS data for Malargüe (Argentina), 2009. The divergence in atmospheric depth with respect to US-StdA 76. January and July are highlighted.
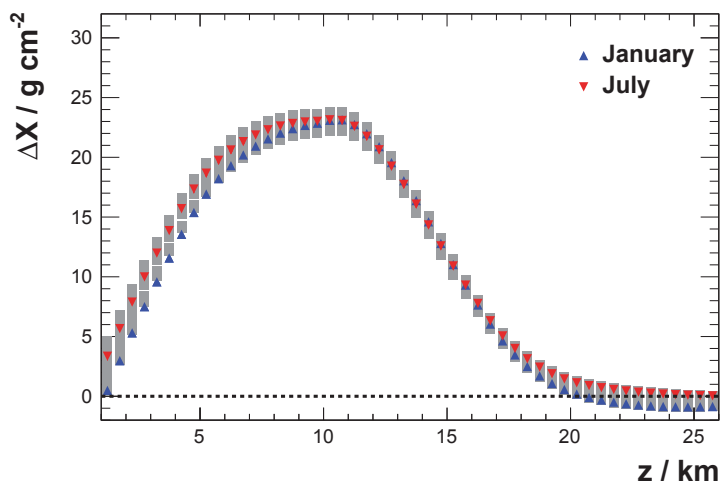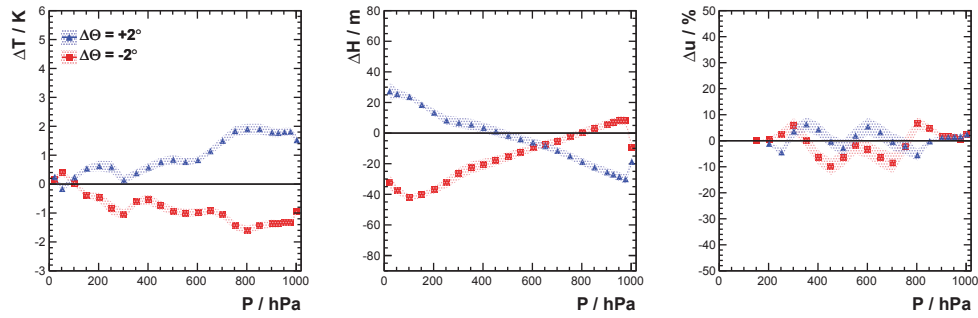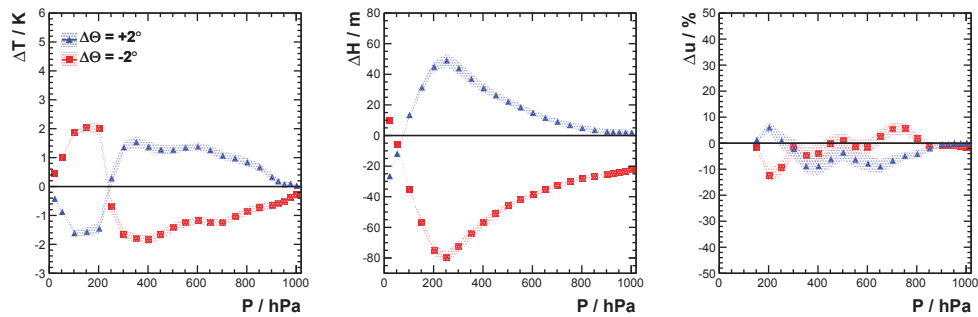

Figure B.32: GDAS data for Pago Pago (American Samoa), 2012. The divergence in atmospheric depth with respect to US-StdA 76. January and July are highlighted.
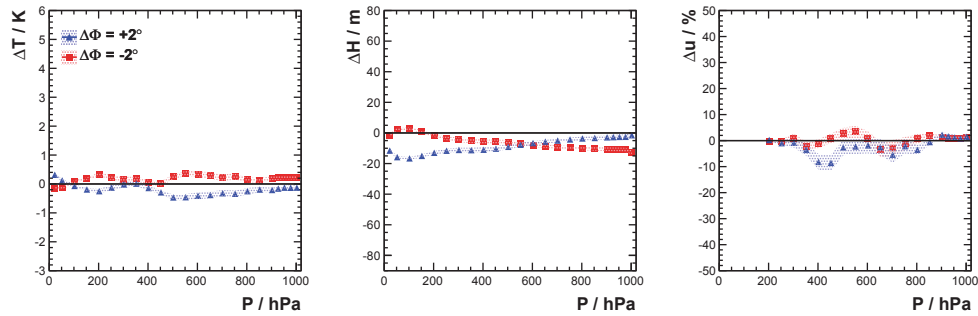
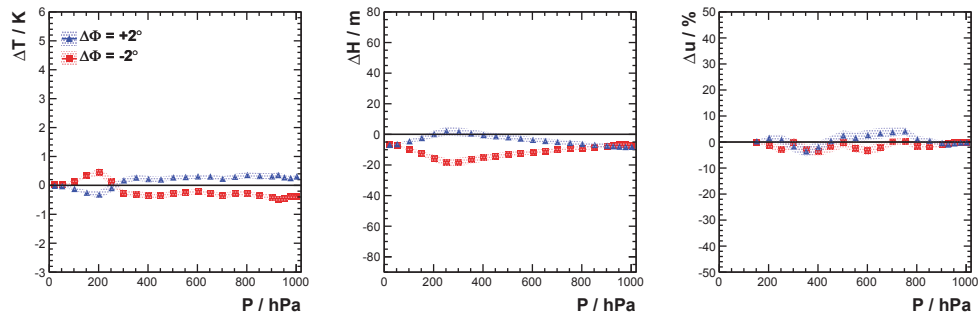# B.3 Local Variability of Atmosphere
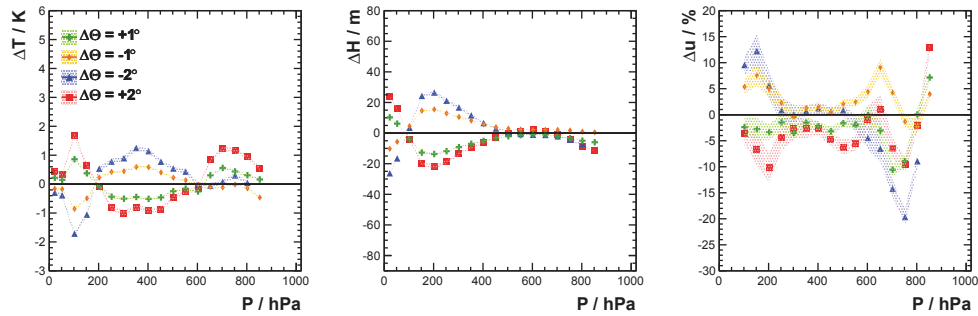
(a) Latitude, January 2009

(b) Latitude, July 2009

(c) Longitude, January 2009

(d) Longitude, July 2009

Figure B.33: Divergence of atmospheric profiles (T, h, u) at surrounding GDAS grid locations as function of pressure. Alëutian islands. The colored bands represent the standard deviation on the mean in each bin.

(a) Latitude, January 2009

(b) Latitude, July 2009
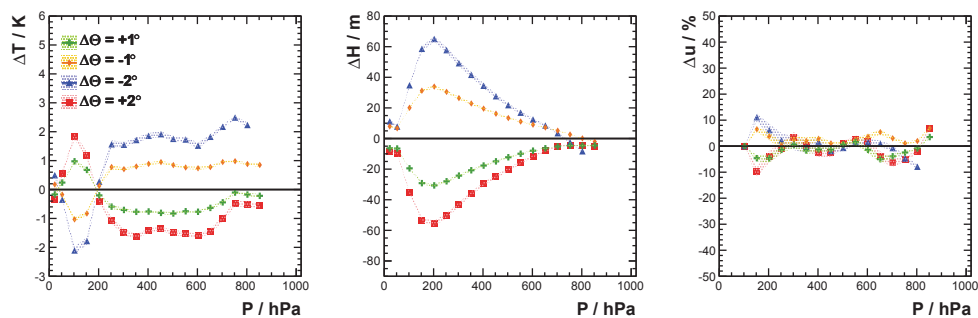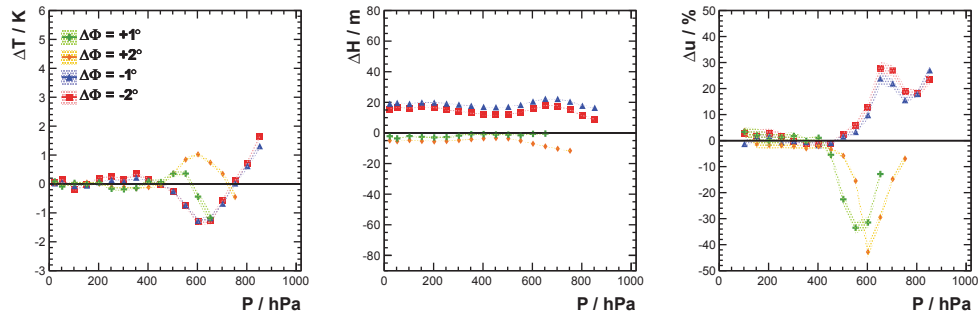

(c) Longitude, January 2009

(d) Longitude, July 2009

Figure B.34: Divergence of atmospheric profiles (*T*, *h*, *u*) at surrounding GDAS grid locations as function of pressure. Antofagasta (Chile). The colored bands represent the standard deviation on the mean in each bin.

(a) Latitude, January 2009

(b) Latitude, July 2009

(c) Longitude, January 2009

(d) Longitude, July 2009

Figure B.35: Divergence of atmospheric depth profiles at surrounding GDAS grid locations as function of height. Alëutian Islands. The colored bands represent the standard deviation on the mean in each bin.
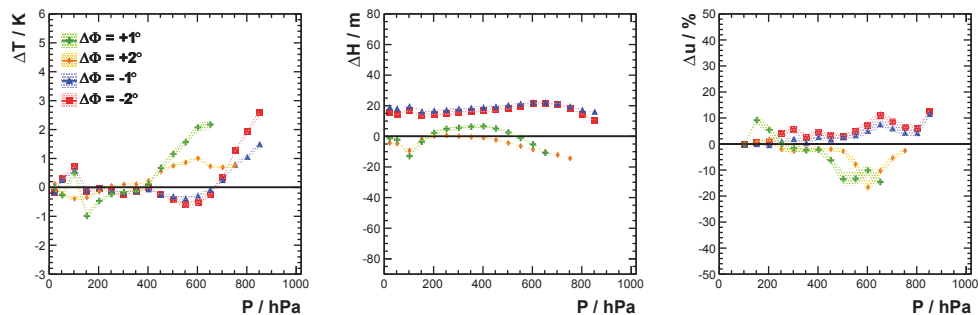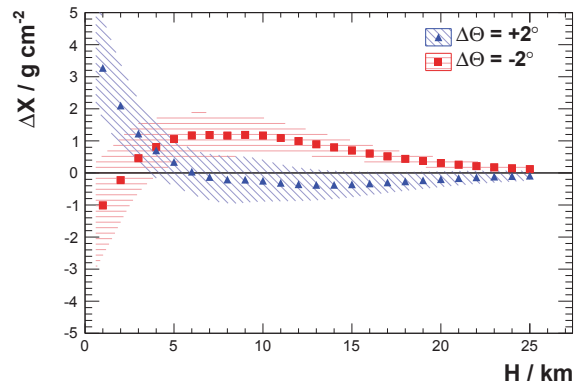
(a) Latitude, January 2009

(b) Latitude, July 2009

(c) Longitude, January 2009
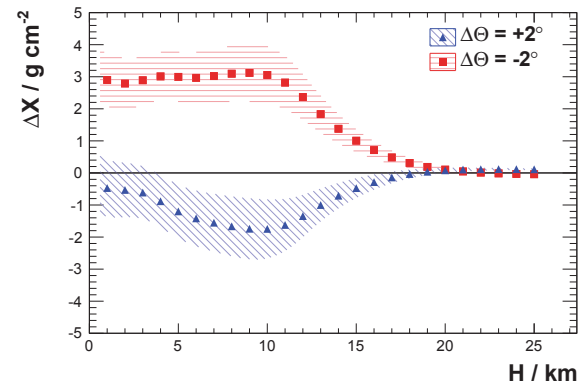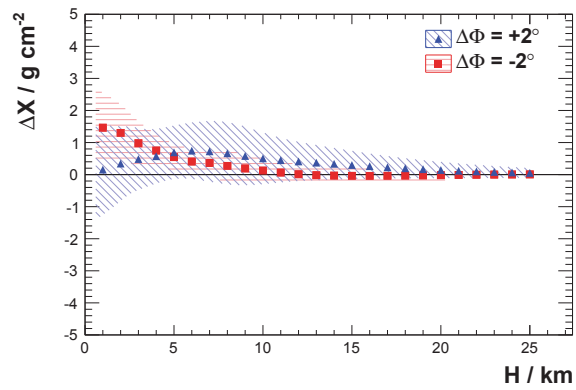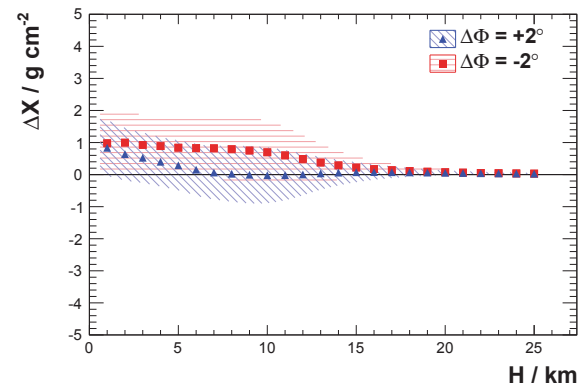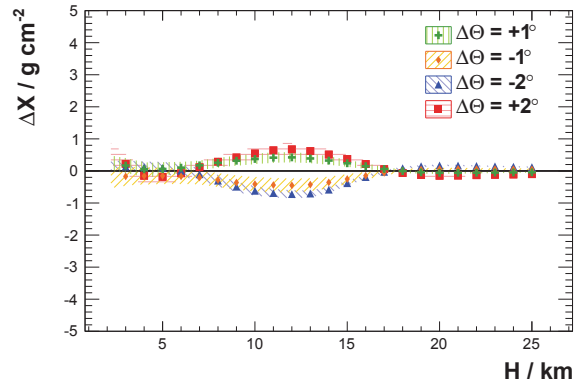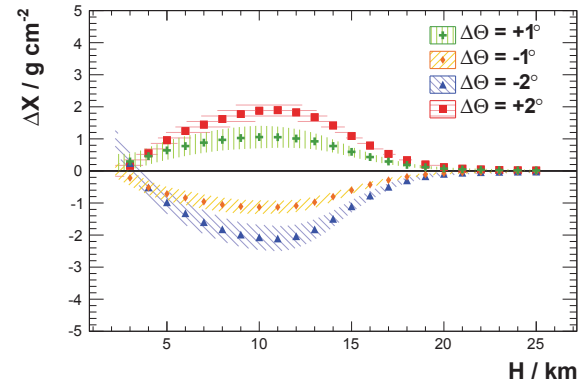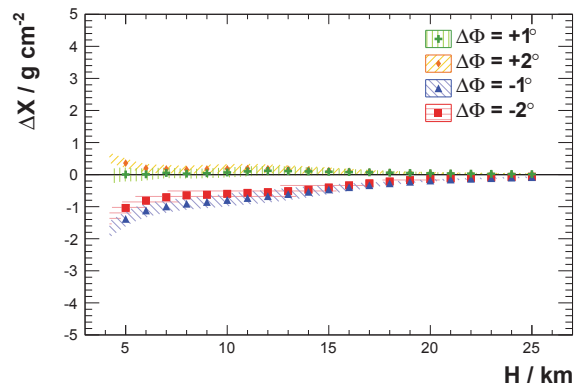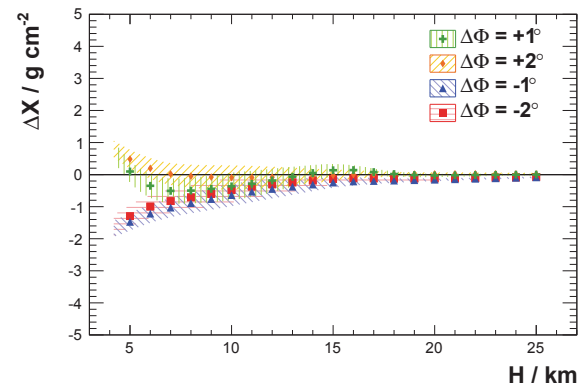
(d) Longitude, July 2009

Figure B.36: Divergence of atmospheric depth profiles at surrounding GDAS grid locations as function of height. Antofagasta (Chile). The colored bands represent the standard deviation on the mean in each bin.

Atmospheric Scenarios

Table C.1: Total amount and components of transmitted light at aperture of JEM-EUSO in different conditions at the Pico (Azores) and Malargüe (Argentina). The statistical uncertainty is about 1%.

Location	total	fluo.	Cher. scat.	Cher. refl.	fluo. refl.
Pico	8518	6329	1404	734	50.4
−2° N	8554	6353	1415	736	50.4
−1° N	8538	6342	1410	735	50.4
+1° N	8502	6321	1397	733	50.4
+2° N	8479	6306	1390	732	50.4
Malargüe	7920	6289	1325	286	19.8
+2° E	7948	6302	1340	286	19.8
+1° E	7938	6294	1338	286	19.8
−1° E	17378	5933	916	9802	727.4
−2° E	8411	6271	1340	748	51.6

Table C.2: Total amount and components of transmitted light at aperture of JEM-EUSO in different locations in summer. The statistical uncertainty is about 1%.

Location	total	fluo.	Cher. scat.	Cher. refl.	fluo. refl.
Aleutian	7895	6272	1317	287	19.9
Andaman	8221	6497	1405	299	20.5
Antofagasta	8308	6538	1452	298	20.3
Azores	8219	6462	1447	290	19.8
Boulder	8132	6478	1334	300	20.7
Hilo	8240	6491	1434	294	20.1
Malargüe	8070	6394	1366	291	20.0
Pago Pago	8285	6531	1433	301	20.5
Timmins	8043	6373	1360	290	20.0

Table C.3: Total amount and components of transmitted light at aperture of JEM-EUSO in different locations in winter. The statistical uncertainty is about 1%.

Location	total	fluo.	Cher. scat.	Cher. refl.	fluo. refl.
Aleutian	7370	5885	1196	269	19.1
Andaman	8241	6512	1410	299	20.5
Antofagasta	8164	6439	1413	292	20.0
Azores	8037	6329	1404	284	19.5
Boulder	7702	6150	1249	283	19.8
Hilo	8192	6458	1421	292	20.1
Malargüe	7811	6195	1317	280	19.4
Pago Pago	8272	6528	1425	299	20.4
Timmins	7481	5967	1221	273	19.3
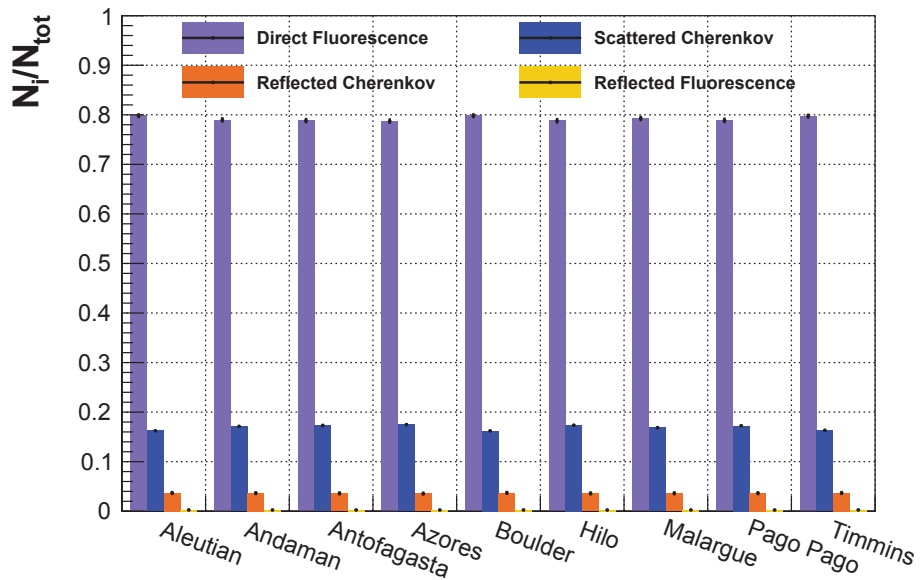
(a) Winter: January (north), July (south)

Figure C.1: The ratio of light at aperture for different atmospheric conditions (global locations). The albedo had been set to Savannah in all cases. Ozone profiles of Hilo, Boulder, and Pago Pago have been used according to month and location.
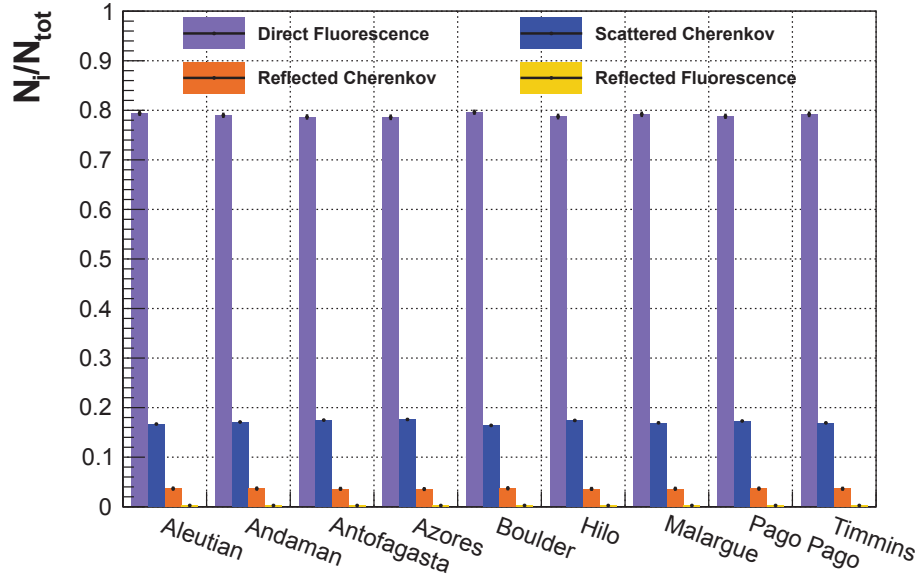
(b) Summer: July (north), January (south)

Figure C.1: The ratio of light at aperture for different atmospheric conditions (global locations). The albedo had been set to Savannah in all cases. Ozone profiles of Hilo, Boulder, and Pago Pago have been used according to month and location.

Table C.4: The amount and components of transmitted light at aperture of JEM-EUSO in different locations and dates.

Location	Date	fluo.	Cher. scat.	Cher. refl.	fluo. refl.
Alëutian	2009 February	5923±476	1189± 83	273± 9	19.3±0.6
	20.02.2011	6137±463	1319± 81	276± 11	19.2±0.5
Andaman	2009 March	6492±497	1399± 89	298± 11	20.5±0.6
	04.03.2010	6507±497	1402± 91	299± 11	20.5±0.6
Antofagasta	2009 July	6439±481	1413± 87	292± 12	20.0±0.5
	08.07.2010	6475±482	1422± 87	295± 12	20.2±0.5
Azores	2009 May	6306±470	1386± 81	282± 12	19.4±0.5
	13.05.2010	6303±465	1392± 82	281± 12	19.3±0.5

Bibliography

[1] ABRAHAM, J., ET AL. Measurement of the Depth of Maximum of Extensive Air Showers above 10^{18} eV. *Phys. Rev. Lett. 104* (2010).

[2] ABREU, P., ET AL. Description of Atmospheric Conditions at the Pierre Auger Observatory using the Global Data Assimilation System (GDAS). *Astropart. Phys. 35* (2012), 591–607.

[3] ADAMS, J., ET AL. An evaluation of the exposure in nadir observation of the JEM-EUSO mission. *Astropart. Phys. 44* (2013), 76–90.

[4] AHN, E. J., ET AL. Measurement of the Depth of Shower Maximum of Cosmic Rays above 1 EeV, 2009. gap-2009-078.

[5] ALLEN, J., ET AL. The Pierre Auger Observatory offline software. *J. Phys. Conf. Ser. 119* (2008).

[6] AMBIWEB GMBH. climate-data.org. online, February 2014.

[7] APEL, W. D., ET AL. Kneelike structure in the spectrum of the heavy component of cosmic rays observed with KASCADE-Grande. *Phys. Rev. Lett. 107* (2011), 171104.

[8] APEL, W. D., ET AL. KASCADE-Grande measurements of energy spectra for elemental groups of cosmic rays. *Astropart. Phys. 47* (2013), 54–66.

[9] ARCIPRETE, F., ET AL. AIRFLY: Measurement of the fluorescence yield in atmospheric gases. *Czech. J. Phys. 56, 0* (2006), 361–367.

[10] ARGIRO, S., BARROSO, S., GONZALEZ, J., NELLEN, L., PAUL, T. C., ET AL. The Offline Software Framework of the Pierre Auger Observatory. *Nucl. Instrum. Meth. A580* (2007), 1485–1496.

[11] AVE, M., ET AL. Precise measurement of the absolute fluorescence yield of the 337 nm band in atmospheric gases. *Astropart. Phys. 42* (2013), 90–102.

[12] BARCIKOWSKI, E., ET AL. Mass Composition Working Group Report at UHECR-2012. *EPJ Web Conf. 53* (2013), 01006.

[13] BASS, A. M., AND PAUR, R. J. The Ultraviolet Cross-Sections Of Ozone: I. The Measurements. *Ozone Symposium - Greece* (1984).

[14] BENSON, R., AND LINSLEY, J. Satellite observation of cosmic ray air showers. *Proc. of 17th Int. Cosmic Ray Conf., Paris (France)* (1981), 145–148.

[15] BenZvi, S.Y. and Connolly, B.M. and Matthews, J.A.J. and Prouza, M. and Visbal, E.F. and others. Measurement of the Aerosol Phase Function at the Pierre Auger Observatory. *Astropart. Phys. 28* (2007), 312–320.

[16] Berat, C., Bottai, S., De Marco, D., Moreggia, S., Naumov, D., et al. ESAF: Full Simulation of Space-Based Extensive Air Showers Detectors. *Astropart. Phys. 33* (2010), 221–247.

[17] Berezinsky, V. Transition from galactic to extragalactic cosmic rays. *Invited talk at 30th Int. Cosmic Ray Conf., Merida (Mexico)* (2007). arxiv:0710.2750v2 [astro-ph].

[18] Blaicher, M. End-to-end simulation of the Extreme Universe Space Observatory (EUSO), 2012. Bachelor thesis, Karlsruher Institut für Technologie (KIT).

[19] Blümer, J., Engel, R., and Hörandel, J. Cosmic rays from the knee to the highest energies. *Prog. Part. Nucl. Phys. 63*, 2 (2009), 293–338.

[20] Bogumil, K., Orphal, J., and Burrows, J. P. Temperature Dependent Absorption Cross Sections Of O_3 , NO_2 , And Other Atmospheric Trace Gases Measured With The Sciamachy Spectrometer. In *Proceedings of the ERS - Envisat Symposium Goteborg Sweden. ERS* (2000).

[21] Bucholtz, A. Rayleigh-scattering calculations for the terrestrial atmosphere. *Appl. Opt. 34*, 15 (1995), 2765–2773.

[22] Bunner, A. N. *Cosmic Ray Detection by Atmospheric Fluorescence*. PhD thesis, Cornell University, Ithaca, NY, USA, 1967.

[23] Casolino, M., et al. Calibration and testing of a prototype of the JEM-EUSO telescope on Telescope Array site. *EPJ Web Conf. 53* (2013), 09005.

[24] Chadyšiene, R., and Girgždys, A. Ultraviolet radiation albedo of natural surfaces. *J. Environ. Eng. Landsc. 16*, 2 (2008), 83–88.

[25] Chapman, S. *A Theory of Upper-atmospheric Ozone*. Memoirs of the Royal Meteorological Society. Edward Stanford, 1930.

[26] Dagoret, S. and Mot, B. EUSO-BALLOON Assembly, Integration and Tests Document. Tech. rep., Laboratoire de l'Accélérateur Linéaire (LAL), 2014.

[27] Eck, T. F., Bhartia, P. K., Hwang, P. H., and Stowe, L. L. Reflectivity of Earth's surface and clouds in ultraviolet from satellite observations. *J. Geophys. Res. 92* (1987), 4287–4296.

[28] Encyclopaedia Britannica Online. declination, 2014. online, http://www.britannica.com/EBchecked/topic/155216/declination.

[29] Engel, R., Heck, D., and Pierog, T. Extensive air showers and hadronic interactions at high energy. *Ann. Rev. Nucl. Part. Sci. 61* (2011), 467–489.

[30] Falcke, H., et al. Detection and imaging of atmospheric radio flashes from cosmic ray air showers. *Nature 435* (2005), 313–316.

[31] Fenu, F. *A Simulation Study of the JEM-EUSO Mission for the Detection of Ultra-High Energy Cosmic Rays*. PhD thesis, Eberhard Karls Universität Tübingen, 2013.

[32] Fick, B., et al. The Central laser facility at the Pierre Auger Observatory. *JINST 1* (2006), P11003.

[33] Forkel, M. Infoblatt Klimadiagramm, April 2012. Klett - Geographie Infothek.

[34] Frank, I., and Tamm, I. Coherent visible radiation of fast electrons passing through matter. *C.R. Acad. Sci. URSS 14* (1937), 109–114.

[35] Gaisser, T. K. *Cosmic Rays and Particle Physics*. Cambridge University Press, 1990.

[36] Global Ozone Research and Monitoring Project. Twenty Questions and Answers About the Ozone Layer, 2002. Scientific Assessment of Ozone Depletion: 2002.

[37] Gockel, A. Luftelektrische Beobachtungen bei einer Ballonfahrt. *Phys. Zeits.* (1910), 280.

[38] Gonzalez, J. G. The Offline Software of the Pierre Auger Observatory: Lessons Learned. *ArXiv e-prints* (2012). arXiv:1208.2154 [astro-ph].

[39] Gorodetzky, P. EUSO in September 2004. *Nucl. Phys. Proc. Suppl. 151* (2006), 401–406.

[40] Greisen, K. End to the cosmic-ray spectrum? *Phys. Rev. Lett. 16*, 17 (1966), 748–750.

[41] Harari, D., Mollerach, S., and Roulet, E. On the ultra-high energy cosmic ray horizon. *JCAP 0611* (2006), 012.

[42] Haungs, A., Rebel, H., and Roth, M. Energy spectrum and mass composition of high-energy cosmic rays. *Rept. Prog. Phys. 66* (2003), 1145–1206.

[43] Heck, D., Knapp, J., Capdevielle, J. N., Schatz, G., and Thouw, T. CORSIKA: A Monte Carlo Code to Simulate Extensive Air Showers. *Wissenschaftl. Berichte Forschungszentrum Karlsruhe, Technik und Umwelt FZKA-6019* (1998).

[44] Heitler, W. *Quantum Theory of Radiation*. Oxford University Press, Oxford, 1944.

[45] Henyey, L. G., and Greenstein, J. L. Diffuse radiation in the Galaxy. *Astro. Phys. 93* (1941), 70–83.

[46] Hess, V., and Kolhörster, W. Über Beobachtungen der durchdringenden Strahlung bei sieben Freiballonfahrten. *Phys. Zeits. 13* (1912), 1084–1091.

[47] Hillas, A. The sensitivity of Cerenkov radiation pulses to the longitudinal development of Cosmic-ray showers. *J. Phys. G8* (1982), 1475–1492.

[48] HILLAS, A. M. The Origin of Ultrahigh-Energy Cosmic Rays. *Ann. Rev. Astron. Astrophys. 22* (1984), 425–444.

[49] KARNEY, C. Algorithms for geodesics. *J. Geodesy 87*, 1 (2013), 43–55.

[50] KEILHAUER, B. Investigation of Atmospheric Effects on the Development of Extensive Air Showers and their Detection with the Pierre Auger Observatory. *Wissenschaftl. Berichte Forschungszentrum Karlsruhe, Technik und Umwelt FZKA-6958* (2004).

[51] KEILHAUER, B., BOHACOVA, M., FRAGA, M., MATTHEWS, J., SAKAKI, N., ET AL. Nitrogen fluorescence in air for observing extensive air showers. *EPJ Web Conf. 53* (2013), 01010.

[52] KOTERA, K., AND OLINTO, A. V. The Astrophysics of Ultrahigh Energy Cosmic Rays. *Ann. Rev. Astron. Astrophys. 49* (2011), 119–153.

[53] KRZYŚCIN, J. W., AND BORKOWSKI, J. L. Variability of the total ozone trend over europe for the period 1950-2004 derived from reconstructed data. *Atmos. Chem. Phys. Discuss. 8* (2008), 47–69.

[54] KULKARNI, P., Ed. *Aerosol measurement : principles, techniques, and applications*, 3rd ed. Wiley, Hoboken, N.J, 2011.

[55] MALICET, J., DAUMONT, D., CHARBONNIER, J., PARISSE, C., CHAKIR, A., AND BRION, J. Ozone UV Spectroscopy. II. Absorption Cross-Sections and Temperature Dependence. *J. Atmos. Chem.* (1995).

[56] MATTHEWS, J. A Heitler model of extensive air showers. *Astropart. Phys. 22* (2005), 387–397.

[57] MCPETERS, R. D., LABOW, G. J., AND JOHNSON, B. J. A satellite-derived ozone climatology for balloonsonde estimation of total column ozone. *J. Geophys. Res. 102* (1997), 8875–8885.

[58] MIE, G. Beiträge zur Optik trüber Medien, speziell kolloidaler Metallösungen. *Ann. Phys. 25*, 4 (1908), 377–445.

[59] MOGG, P. Untersuchung der Auswirkung extremer atmosphärischer Bedingungen auf die Messung von ausgedehnten Luftschauern mit Fluoreszenzteleskopen, 2012. Bachelor thesis, Karlsruher Institut für Technologie (KIT).

[60] MOLINA, L. T., AND MOLINA, M. J. Absolute absorption Cross Sections of Ozone in the 185- to 350-nm Wavelength Range. *J. Geophys. Res.* (1986).

[61] NAGANO, M., KOBAYAKAWA, K., SAKAKI, N., AND ANDO, K. New measurement on photon yields from air and the application to the energy estimation of primary cosmic rays. *Astropart. Phys. 22* (2004), 235–248.

[62] NATIONAL AERONAUTICS AND SPACE ADMINISTRATION. U.S. Standard Atmosphere 1976. Tech. Rep. NASA-TM-X74335, (NASA), 1976.

[63] NATIONAL IMAGERY AND MAPPING AGENCY. World geodetic system 1984. Tech. Rep. Third Edition, Amendment 1, Department of Defense, 2000.

[64] National Oceanic and Atmospheric Administration (NOAA). Summit, Greenland Balloon-Borne Ozonesonde Profile Measurement Program. online report, http://www.esrl.noaa.gov/gmd/dv/ozwv/sum/sum.html.

[65] National Oceanic and Atmospheric Administration (NOAA). Global Data Assimilation System (GDAS1) Archive Information. Tech. rep., Air Ressources Laboratory (ARL), http://ready.arl.noaa.gov/gdas1.php, 2004.

[66] Nauss, T., et al. The intercomparison of selected cloud retrieval algorithms. *Atmos. Res. 78*, 1-2 (2005), 46–78.

[67] Nerling, F. Description of Cherenkov light production in extensive air showers. *Wissenschaftl. Berichte Forschungszentrum Karlsruhe, Technik und Umwelt FZKA-7105* (2005).

[68] Nicodemus, F. E. Directional Reflectance and Emissivity of an Opaque Surface. *Appl. Opt., 4* (1965), 767–775.

[69] Office of the Federal Coordinator for Meteorology, US. *Federal Meteorological Handbook*, 3rd ed., 1997. Appendix D: Computational Formulae and Constants.

[70] Olinto, A. V. Cosmic Rays of Extreme Energies. *Nucl. Phys. Proc. Suppl. 243-244* (2013), 108–115.

[71] Orphal, J. A critical review of the absorption cross-sections of O_3 and NO_2 in the ultraviolet and visible. *J. Photochem. Photobio. A* (2003).

[72] Osteria, G., and Scotti, V. Euso-Balloon: A pathfinder mission for the JEM-EUSO experiment. *Nucl. Instrum. Meth. A732* (2013), 320–324.

[73] Pierog, T., Alekseeva, M., Bergmann, T., Chernatkin, V., Engel, R., et al. First results of fast one-dimensional hybrid simulation of EAS using CONEX. *Nucl. Phys. Proc. Suppl. 151* (2006), 159–162.

[74] Piotrowski, L. W. Status of TA-EUSO. Private conversation, August 2014.

[75] Press, W. H., Teukolsky, S. A., Vetterling, W. T., and Flannery, B. P. *Numerical Recipes in C++: The Art of Scientific Computing*, second ed. Cambridge University Press, 2002. Chapter 5.

[76] Salby, M. L. *Physics of the Atmosphere and Climate*. Cambridge University Press Textbooks, 2012.

[77] Shibata, T., et al. Absolute energy calibration of the Telescope Array fluorescence detector with an electron linear accelerator. *EPJ Web Conf. 53* (2013), 10004.

[78] Smida, R., Baur, S., Bertaina, M., Blümer, J., Chiavassa, A., et al. Observation of microwave emission from extensive air showers with CROME. *EPJ Web Conf. 53* (2013), 08010.

[79] SpaceX. First Private Spacecraft to the Space Station. online. http://www.spacex.com/dragon.

[80] STECKER, F. W., KRIZMANIC, J., BARBIER, L., LOH, E., MITCHELL, J., ET AL. Observing the ultrahigh-energy universe with OWL eyes. *Nucl. Phys. Proc. Suppl. 136C* (2004), 433–438.

[81] TAKAHASHI, Y., ET AL. Central laser facility analysis at the Telescope Array experiment. *AIP Conf. Proc. 1367* (2011), 157–160.

[82] THE JEM-EUSO COLLABORATION. The JEM-EUSO Mission: Status and Prospects in 2011. *ArXiv e-prints* (2012). arXiv:1204.5065 [astro-ph].

[83] THE JEM-EUSO COLLABORATION. The JEM-EUSO Mission: Contributions to the ICRC 2013. *ArXiv e-prints* (2013). arXiv:1307.7071 [astro-ph].

[84] THEA, A., ET AL. The EUSO Simulation and Analysis Framework. *Proc. 29th Int. Cosmic Ray Conf., Pune (India)* (2005).

[85] TOMASI, C., VITALE, V., PETKOV, B., LUPI, A., AND CACCIARI, A. Improved algorithm for calculations of Rayleigh-scattering optical depth in standard atmospheres. *Appl. Opt. 44*, 16 (2005), 3320–3341.

[86] UNGER, M. Composition Studies with the Pierre Auger Observatory. *Nucl. Phys. Proc. Suppl. 190* (2009), 240–246.

[87] UPPALA, S. M., ET AL. The ERA-40 re-analysis. *Quart. J. Roy. Meteor. Soc. 131*, 612 (2005), 2961–3012.

[88] VERZI, V., ET AL. The fluorescence detector of the Pierre Auger Observatory. *Nucl. Phys. Proc. Suppl. 165* (2007), 37–44.

[89] WULF, T. Über die in der Atmosphäre vorhandene Strahlung von hoher Durchdringungsfähigkeit auf dem Eiffelturm. *Phys. Zeits. 11* (1910), 811–813.

[90] ZATSEPIN, G., AND KUZMIN, V. Upper limit of the spectrum of cosmic rays. *JETP Lett. 4* (1966), 78–80.

Acknowledgment

I would like to thank Prof. Johannes Blümer for the opportunity to write my thesis and Prof. Ulrich Husemann for diligently acting as co-referee.

My sincere thanks go to everybody that made this work possible over the course of the past 3 1/2 years. I also thank my advisors Bianca Keilhauer and Andreas "Andy" Haungs.

Since I will almost certainly forget some people, I will not emphasize *any* by name. You all know, I have appreciated your help and advice.

Thank you all.